MODELING AND INVERSION IN NEAR-FIELD MICROWAVE MICROSCOPY AND ELECTRICAL IMPEDANCE TOMOGRAPHY

WEI ZHUN
B. Sc., University of Electronic Science and Technology of China, China

A THESIS SUBMITTED

FOR THE DEGREE OF DOCTOR OF PHILOSOPHY OF ENGINEERING

DEPARTMENT OF ELECTRICAL AND COMPUTER ENGINEERING

NATIONAL UNIVERSITY OF SINGAPORE

2016

DECLARATION

I hereby declare that the thesis is my original work
and it has been written by me in its entirety.
I have duly acknowledged all the sources of
information which have been used in the thesis.

This thesis has also not been submitted for any
degree in any university previously.

Wei Zhun

Wei Zhun

22 July 2016

Acknowledgements

First and foremost, I would like to express my deepest gratitude to my supervisor, Prof. Xudong Chen. As a supervisor and mentor, he has given many instructive suggestions on my research and taught me how to be a good researcher. As a brother, he has encouraged me in my hard time and shared his life experience with me. I sincerely feel that I owe to Prof. Chen a huge debt, and it is a great treasure for me to spend these four years with him.

Secondly, I would like to thank all the staffs in Microwave and RF research group in National University of Singapore, for providing a pleasant lab for the research, instructing me on class and offering kind assistance during my doctoral study.

I would also like to thank my seniors, Krishna Agarwal and Chen Rui, for their professional guidance, very helpful discussions, and friendship. It is also my pleasure to express my appreciation to Ye Xiuzhu, Chen Wen, Zhong Yu, Pan li, Hoang Thanh Xuan, Kuiwen Xu, and Song Rencheng for sharing their research experience and life happiness with me. I greatly cherish the time spent with all of them.

I would specially like to thank Prof. Zhi-Xun Shen at Stanford University and his microwave impedance microscopy team

members, such as Yong-Tao Cui and Eric Yue Ma, for providing experimental data, very helpful discussions and suggestions.

Last but not least, I am deeply grateful to my dear parents, who give me the most endless love. Also, I would like to thank my girlfriend, Jin Lei, for her selfless support and endless love.

Table of Contents

Declaration **i**

Acknowledgements **iii**

Table of Contents **v**

Summary **ix**

List of Tables **xi**

List of Figures **xiii**

List of Symbols **xviii**

List of Publications **xx**

1 Introduction **1**

1.1 Inverse problem 1

1.2 Near-field microwave microscopy 3

1.2.1 Why near-field microwave microscopy? 3

1.2.2 State of the art in NFMM 6

1.2.3 Challenges in NFMM 9

1.3 Electrical impedance tomography problem 10

1.4 Overview of the thesis 12

2 Tip-Sample Interaction in NFMM 15

2.1 Introduction 15

2.2 Microwave impedance microscopy 16

2.2.1 Lumped element modeling 20

2.2.2 MIM-R and MIM-I channels 21

2.3 Equivalent-sphere model in NFMM 22

2.3.1 Bispherical coordinate system 22

2.3.2 Green's function due to a charge 24

2.3.3 Tip charge variation due to a dipole 26

2.3.4 Numerical validation and conclusions 27

2.4 Quantitative analysis of effective height of probes in NFMM . 30

2.4.1 Experimental details and analysis approach 32

2.4.2 Results and discussions 35

2.4.2.1 Cumulative contribution of $C'(h)$, $C'(h)$, and $C''(h)$ 35

2.4.2.2 Effective height of $C'(h)$ and $C''(h)$ 38

2.4.3 Experiment validation 40

2.5 Summary 43

3 A Novel Forward Solver in NFMM 45

3.1 Introduction 45

3.2 Theory and principle of forward solver 48

3.2.1 Model description 48

3.2.2 Calculation of potential 49

3.2.3 Calculation of contrast capacitance 51

3.3 Numerical validation 53

3.3.1 Contrast capacitance at one scanning point 53

3.3.2 Effective interaction area 56

3.3.3 Contrast capacitance at different scanning points . . . 58

3.4 Experimental validation 60

3.5 Summary 64

4 Nonlinear Image Reconstruction with Total Variation in NFMM 66

4.1 Introduction 66

4.2 Inverse formulation 67

4.3 Implementation procedures 69

4.4 Numerical validation 71

4.5 Summary 75

5 Two FFT Subspace-Based Optimization Methods for Electrical Impedance Tomography 76

5.1 Introduction 76

5.2 Forward model 80

5.2.1 Model description 80

5.2.2 Theoretical principle 81

5.2.3 Discretization method 83

5.2.4 Singularities in Green's function 85

5.3 Inverse algorithm 86

5.3.1 Subspace-based optimization method (SOM) 86

5.3.2 New fast Fourier transform subspace-based optimization method (NFFT-SOM) 87

5.3.3 Low frequency subspace optimization method (LF-SOM) 88

5.3.4 Implementation procedures 89

5.4 Numerical simulation and discussions 91

5.5 Summary 97

6 Conclusions and Future Work **99**

6.1 Conclusions 99

6.2 Future work 102

Bibliography **104**

Appendix A: Derivation of Coefficients in Dirichlet Green's Function for Equivalent-Sphere Model **129**

Summary

This thesis addresses the modeling and inversion in near-field microwave microscopy (NFMM) and electrical impedance tomography (EIT) problems. Both the modeling and inversion are conducted in the framework of Laplace's equation since the computational domain is much smaller than the wavelength in the NFMM and the problem is purely static in the EIT. The original contributions of this thesis are: Firstly, the thesis presents a complete analysis of tip-sample interaction in NFMM, which includes proposing both lumped element model method and impedance variation method to analyze the experimental system, deriving the Green's function for calculating charges on tip in equivalent-sphere model, and introducing the concept of effective height to analyze the contribution of tips in NFMM. Secondly, based on the analysis of tip-sample interaction, the thesis proposes a novel forward solver for NFMM which can be applied to arbitrary tip shapes, thick and thin films, and complex inhomogeneous perturbation. It is shown that this method can accurately calculate capacitance variation due to inhomogeneous perturbation in insulating or conductive samples, as verified by both results of commercial software and experimental data from microwave impedance microscopy (MIM). Thirdly, a nonlinear image reconstruction method with total variation constraint in NFMM is presented based on the forward solver proposed.

Numerical results show that the proposed method can accurately reconstruct the permittivity distribution in three dimensional samples for NFMM. Most importantly, it is found from the results that the resolution has been significantly improved in the reconstructed image. Finally, inversion method is also applied to solve the electric impedance tomography (EIT) problem in a domain with arbitrary boundary shape, and two new inversion methods are presented. The first is the new fast Fourier transform subspace-based optimization method (NFFT-SOM), and the second is the low frequency subspace optimization method (LF-SOM). The thesis gives a detailed analysis of strengths and weaknesses of NFFT-SOM and LF-SOM. It is found that compared with the traditional subspace optimization method (SOM), both of the proposed methods are faster and can get a smaller exact error in solving EIT problem.

List of Tables

2.1 Effective height h_e of $C''(h)$ for typical tips and samples in NFMM (Units: μm). 40

List of Figures

1.1 Field regions for antennas equal to, or shorter than, one-half wavelength of the radiation they emit. According to the definition in "Electromagnetic Radiation: Field Memo" by OSHA cincinnati laboratory, the 2 wavelengths definition for far field is approximate "rules of thumb". More precise far field boundary is normally defined based primarily on antenna type and antenna size as $2D^2/\lambda$. (From Wikipedia) 3

1.2 Modeling of a cross section of a human thorax showing current stream lines and equi-potentials from drive electrodes [1]. . . . 10

1.3 A brief schematic of forward and inverse models in electrical impedance tomography problems. 12

2.1 Block diagram of MIM electronics in the reflection mode. [2, 3] 16

2.2 Measurement environment for microwave impedance microscopy with setup and devices [2–4]. 17

2.3 (a) A lumped element model between Z-match network and ground. (b) Magnitude of S_{11} for experiment and simulation. (c) Phase of S_{11} for experiment and simulation. 19

2.4 Bispherical coordinate system [5]. 23

2.5 Dipole geometry. 26

2.6 Typical potential distribution of tip-ground system for equivalent-sphere model. 28

2.7 Surface charge density on the tip of $\phi = 0$ surface induced by a unit dipole placed along the η direction, where horizontal coordinate represents the X coordinate of the tip surface. . . . 29

2.8 Surface charge density on the tip of $\phi = 0$ surface induced by a unit dipole placed along the ϕ direction, where horizontal coordinate represents the X coordinate of the tip surface. . . . 29

2.9 (a) A simple schematic of microwave impedance microscopy with cone-sphere tip. Unless stated otherwise, $H = 15\ \mu m$, $r = 50\ nm$, $\theta = 20°$, $h_s = 200\ nm$, $l = 20\ nm$, and $\varepsilon_r = 3.9$ are used for numerical analysis (Not to scale). (b) Discretization of the tip. 33

2.10 (a) SEM image of the pyramid tip [6] in MIM measurement. (b) SEM image of the Pt tip [7] in MIM measurement. 34

2.11 Cumulative contribution of $C(h)$, $C'(h)$, and $C''(h)$ for the typical model illustrated in Fig. 2.9(a) for (a) dielectric material and (b) metal. 36

2.12 Effective height for C' as a function of relative permittivity (ε_r) for (a) three different sample heights $h_s = 20\ nm$, $h_s = 200\ nm$, $h_s = 500\ nm$, (b) three different apex radii $r = 50\ nm$, $r = 150\ nm$, and $r = 500\ nm$, (c) three different tip half-cone angles: $\theta = 6°$, $\theta = 20°$, and $\theta = 35°$, and (d) three different reference distances $l = 5\ nm$, $l = 12\ nm$, and $l = 20\ nm$. Unless stated otherwise in each case, all the other parameters are the same as that in Fig. 2.9(a). 37

2.13 C' as a function of tip-sample spacing l with Pt tip measuring (a) bulk SiO_2 and (b) Al dot sample for both simulation and experiment results. (c) C' as a function of tip-sample spacing l with pyramid tip measuring Al dot sample for both simulation and experiment results. (Blue square denotes the simulation results from the truncated tip with effective height; Black line denotes the experimental results; Red star denotes the simulation results from equivalent-sphere tip of which the radius is equal to apex radius of practical tip.) 41

3.1 A typical near-field microwave microscopy scheme including geometry and parameters used in the calculation of this chapter: $H = 5\ \mu m$, $h = 0.485\ \mu m$, $\theta = 30°$, $W_p = 1.2\ \mu m$, $W_s = 6\ \mu m$, $h_p = 0.4\ \mu m$, tip sample distance $l = 20\ nm$, and $h_s = 0.6\ \mu m$ (Not to scale). 48

3.2 Contrast capacitance due to the perturbation of domain I which is filled with homogeneous oxide with relative permittivity ε_x for both FE-BI method and COMSOL values. 53

3.3 (a) The side view of a sample with four layers of perturbation filled in domain I. Each layer has a width of W_p and height of h_n and these four layers are filled with alumina, some certain oxide, glass and silicon, respectively. (b) Capacitance variation due to the four layers of perturbation sample depicted in Fig. 3.3(a) for both FE-BI method and COMSOL when changing ε_y from 6 to 40 and (c) changing the conductivity of the second layer from 0.02 S/m to 7.82 S/m. 55

3.4 Contrast capacitance normalized to $W_p = 5\ \mu m$ as a function of W_p for three different half cone angles of tip. 56

3.5 Contrast capacitance normalized to $W_p = 5\ \mu m$ as a function of W_p for three different substrate heights h_s. 57

3.6 Cone-sphere tip scans over a three dimensional sample with an "H" shape perturbation presented ($W_p = 100\ nm$ and $L_s = 400\ nm$). 58

3.7 Contrast Contrast capacitance image when tip scans over "H" shape perturbation (simulation results from COMSOL). 59

3.8 Contrast Contrast capacitance image when tip scans over "H" shape perturbation (results from FE-BI method). 59

3.9 Side view of a buried sample structure, and SiO_2 is buried in Al_2O_3 layer with a specific pattern. 60

3.10 Capacitance varying with tip-sample distance (l) for both EFM and MIM (scaled). The horizontal axis denotes the tip-sample distance. 61

3.11 (a) Capacitance difference between tip-sample distance of 0 nm and 200 nm measured by MIM (dash-line rectangular represents the specific calculation area in FE-BI method). (b) Capacitance difference between tip-sample distance of 0 nm and 200 nm computed by FE-BI method in this chapter. Each pixel has an area of $0.25 \times 0.25\ um^2$. 63

4.1 (a) A three-dimensional sample with an "H" shape perturbation presented with $W_s = 6\ \mu m$, $h_s = 1\ \mu m$, $h_p = 0.4\ \mu m$, $W_h = 100\ nm$, $L_s = 400\ nm$, $\varepsilon_b = 3.9$ and $\varepsilon_1 = 16$; (b) Top view of exact distribution of relative permittivity in (a); (c) The simulated received capacitance signal; (d) Reconstruction of relative permittivity from the signal in (c). 70

4.2 (a) A three-dimensional sample with an "51" shape perturbation presented with $W_s = 6\ \mu m$, $h_s = 1\ \mu m$, $h_p = 0.4\ \mu m$, $W_{s1} = 100\ nm$, $W_{s2} = 250\ nm$, $L_{s1} = 600\ nm$, $L_{s2} = 150\ nm$, $\varepsilon_b = 3.9$, and $\varepsilon_1 = 16$; (b) Top view of exact distribution of relative permittivity in (a); (c) The simulated received capacitance derivative signal; (d) Reconstruction of relative permittivity from the signal in (c). 72

4.3 Top view of exact distribution of (a) relative permittivity and (b) conductivity for a conductive sample with an "51" shape perturbation presented; The simulated received (c) capacitance derivative and (d) conductance derivative signals; Reconstructed (e) relative permittivity and (f) conductivity from the received signals. 73

4.4 (a) The simulated received capacitance derivative signal, where 5% Gaussian noise is added; (b) Reconstruction of relative permittivity from the signal in (a). 74

5.1 A typical schematic of EIT problem with a two dimensional domain consisting of a square with width W_1 and four half circles with a radius of $W_1/2$, in which $W_1 = 1$, and $\sigma_0 = 1$. Voltages are measured at a number of N_r nodes on the boundary ∂I which are labeled as dots. 80

5.2 Schematic of Green's function integral on a small cell with singularities. 85

5.3 (a)The exact profile of two half circles: radii of both half circles are 0.3, and centers are located at (-0.35, -0.2) and (0.35, 0.1), respectively. (b) The singular values of the operator $\overline{\overline{G}}_\partial$, where the base 10 logarithm of the singular value is plotted. 90

5.4 Reconstructed conductivity profiles at the 60th iterations with $L = 4$ for (a) traditional SOM (b) NFFT-SOM and (c) LF-SOM, where 20% Gaussian noise is added. (d) Comparison of exact error f in the first 300 iterations for the three inversion methods with $L = 4$, where the base 10 logarithm of the exact error value is plotted. 91

5.5 Reconstructed conductivity profiles at the 60th iterations with $L = 12$ for (a) traditional SOM (b) NFFT-SOM and (c) LF-SOM, where 20% Gaussian noise is added. (d) Comparison of exact error f in the first 300 iterations for the three inversion methods with $L = 12$, where the base 10 logarithm of the exact error value is plotted. 93

5.6 Comparison of exact error f in the first 300 iterations for (a) traditional SOM (b) NFFT-SOM and (c) LF-SOM with 20% Gaussian noise, where the base 10 logarithm of the exact error value is plotted. 94

5.7 Reconstructed conductivity profiles at the 60th iterations with $L = 12$ for (a) traditional SOM (b) NFFT-SOM and (c) LF-SOM, where 1% Gaussian noise is added. 95

5.8 Comparison of exact error f in the first 300 iterations for (a) traditional SOM (b) NFFT-SOM and (c) LF-SOM with 1% Gaussian noise, where the base 10 logarithm of the exact error value is plotted. 96

List of Symbols

Greek Symbols

ω	Angular frequency
σ	Electrical conductivity
θ	Half cone angle of tip
S_R	MIM-Re signal
S_I	MIM-Im signal
Y	Tip-sample admittance

Acronyms

2D	Two-dimensional
3D	Three-dimensional
ADS	Advanced Design System
AFM	Atomic-force microscopy
AWGN	Additive white Gaussian noise
BEM	Boundary element method
CG	Conjugate gradient
CSI	Contrast source inversion
CT	Computerized tomography
EFM	Electrostatic force microscopy
EIT	Electrical impedance tomography
EMP	Evanescent microwave probe
FEM	Finite element method
FFT	Fast Fourier transform
f-MRI	Functional magnetic resonance imaging
GICM	Generalized image charge method

ITO	Indium-tin-oxide
LF-SOM	Low frequency subspace optimization method
MEMS	Microelectromechanical systems
MIM	Microwave impedance microscopy
MMIC	Monolithic microwave integrated circuit
MOM	Method of moment
NA	Numerical aperture
NFFT-SOM	New fast Fourier transform subspace-based optimization method
NFMM	Near-field microwave microscopy
PRP	Polak-Ribière-Polyak
STED	Stimulated emission depletion
STM	Scanning tunneling microscope
SVD	Singular value decomposition
SOM	Subspace-based optimization method
TSOM	Twofold subspace-based optimization method
UV	Ultraviolet
VNA	Vector network analyzer

List of Publications

[1] **Z. Wei**, Y. T. Cui, E. Y. Ma, S. Johnston, Y. Yang, R. Chen, M. Kelly, Z. X. Shen, X. Chen, "Quantitative Theory for Probe-Sample Interaction With Inhomogeneous Perturbation in Near-Field Scanning Microwave Microscopy," IEEE Transactions on Microwave Theory and Techniques, 64, 1402-1408 (2016).

[2] **Z. Wei**, E. Y. Ma, Y. T. Cui, S. Johnston, Y. Yang, K. Agarwal, M. Kelly, Z. X. Shen, X. Chen, "Quantitative analysis of effective height of probes in near-field microwave microscopy," Review of Scientific Instruments, 87, 094701 (2016).

[3] **Z. Wei**, R. Chen, H. Zhao, and X. Chen, "Two FFT subspace-based optimization methods for electrical impedance tomography," Progress In Electromagnetics Research, Accepted (2016).

[4] R. Chen, M., Wu, J., Ling, **Z. Wei**, Z. Chen, M. Hong, and X. Chen, "Superresolution microscopy imaging using full wave modelling and inverse reconstruction," Optica, 3, 1339-1347 (2016).

[5] **Z. Wei**, Y. T. Cui, E. Y. Ma, S. Johnston, Y. Yang, R. Chen, M. Kelly, Z. X. Shen, X. Chen, "Super-resolution Imaging in near-field microwave microscopy by Inversion," in preparation (2016).

[6] **Z. Wei** and X. Chen, "Numerical study of resolution in near field microscopy for dielectric samples," IEEE International Symposium on Antennas and Propagation (AP-SURSI), (Vancouver, British Columbia, Canada, 910-911, Jul., 2015).

[7] R. Chen, **Z. Wei**, and X. Chen, "Three dimensional through-wall imaging: Inverse scattering problems with an inhomogeneous background medium," Antennas and Propagation (APCAP), 2015 IEEE 4th Asia-Pacific Conference on, (Bali, Indonesia, 505-506, Jun., 2015).

[8] **Z. Wei**, K. Agarwal, R. Chen, and X. Chen, "Analysis of tip-sample interaction in microwave impedance microscopy by lumped element model," Antennas and Propagation (APCAP), 2015 IEEE 4th Asia-Pacific Conference on, (Bali, Indonesia, 67-68, Jun., 2015).

[9] **Z. Wei**, K. Agarwal, and X. Chen, "Analytical Green's function for tip-sample interaction in microwave impedance microscopy," Advanced Materials and Processes for RF and THz Applications (IMWS-AMP), 2015 IEEE MTT-S International Microwave Workshop Series on, (Suzhou, China, 1-3, Jul., 2015).

[10] R. Chen, **Z. Wei**, and X. Chen, "Three Dimensional Inverse Scattering Problems with an Inhomogeneous Background Medium," PIERS 2016, (Shanghai, China, Aug., 2016).

[11] **Z. Wei**, R. Chen, and X. Chen, "Super-resolution Imaging in Near-field Scanning Microwave Impedance Microscopy by Inversion," PIERS 2016, (Shanghai, China, Aug., 2016).

Chapter 1

Introduction

This thesis addresses modeling and inversion in near-field microwave microscopy (NFMM) and electrical impedance tomography (EIT) problems. Both the modeling and inversion are conducted in the framework of Laplace's equation since the computational domain is much smaller than the wavelength in the NFMM and the problem is purely static in the EIT. In the NFMM, the thesis mainly studies tip-sample interaction problem, effective forward solver and the corresponding inversion method. In the EIT, the studies are focused on the new inversion methods which are fast and robust to noise in reconstructing electrical properties. This introductory chapter provides a general description of the inverse problem, near-field microwave microscopy and electrical impedance tomography problems.

1.1 Inverse problem

An inverse problem is the process of solving for the properties of an object (or parameters of a system) from the observation of the response of this object (or system) to a probing signal [8]. It is called inverse problem because it

starts with the response and then reconstructs the properties of the object which cause the response. On contrary, a forward problem starts with the known model and then calculate the response to a probing signal. For example, if an obstacle with specific permittivity distribution is illuminated by electromagnetic waves, the calculation of the scattered fields is the forward problem; if one observes scattered field far away from the the obstacle, the inverse problem, which is referred to as the inverse scattering problem, is to reconstruct the position, shape and permittivity distribution of the obstacle from the observed scattered field.

The inverse scattering technique is one of the most important approaches in quantitatively determining either physical or geometrical properties in various fields [9]. In remote sensing, inversion method is used to estimate physical parameters from the observations of external or internal radiant energy [10]. Inverse technique also acts as a powerful tool to analyze human organs and biological systems in biomedical imaging and diagnosis [11]. In quantum physics, an important application of inversion method is to find the potential from the impedance function [12]. One of the most important advantages of inversion method is that it avoids expensive and destructive evaluation. In order to detect the inhomogeneities in a medium, one only needs to collect the scattered field outside the medium instead of drilling a hole in it. Thus, inverse scattering techniques are also widely used in non-destructive detection [13]. In this thesis, studies are focused on the application of inversion method on characterization of electrical properties in near-field microwave microscopy and electrical impedance tomography problems.

1.2 Near-field microwave microscopy

Near-field microwave microscopy (NFMM) is concerned with measuring the microwave electrodynamic response of materials which have length scales far shorter than the free-space wavelength of the radiation [4, 14–18]. It is an emerging technique used to image semiconductor devices [19], nanoparticles [20], dielectric samples [21], two-dimensional electron gas [22] and other materials with interesting properties [23–26]. In this section, some basic concepts, state of the art, and challenges in NFMM techniques are introduced.

1.2.1 Why near-field microwave microscopy?

Compared with microscopy which relies on the far field interaction, NFMM utilizes the near field interaction between tip and sample. It is well known that, in far field, the spatial resolution is limited by the wavelength known as Abbe diffraction limit found by Ernst Abbe in 1873. It states that spatial

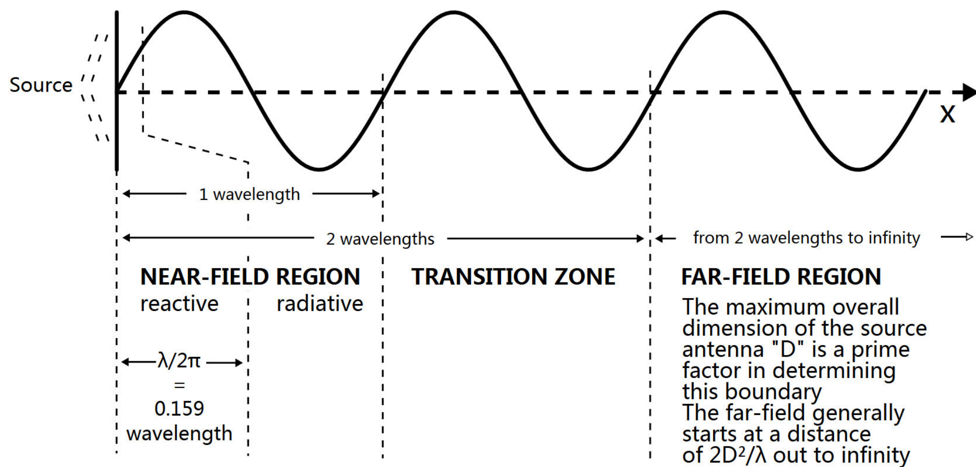

Fig. 1.1 Field regions for antennas equal to, or shorter than, one-half wavelength of the radiation they emit. According to the definition in "Electromagnetic Radiation: Field Memo" by OSHA cincinnati laboratory, the 2 wavelengths definition for far field is approximate "rules of thumb". More precise far field boundary is normally defined based primarily on antenna type and antenna size as $2D^2/\lambda$. (From Wikipedia)

resolution Δr is limited by the equation [27]:

$$\Delta r = \frac{\lambda}{2n \sin\theta} \tag{1.1}$$

in which the denominator $n \sin\theta$ is known as numerical aperture (NA) and can reach about $1.4 - 1.6$ in modern optics. Techniques exploiting shorter wavelengths such as Ultraviolet (UV) [28–32] and X-ray microscopes [33, 34] are often used to increase the resolution, but they are often expensive and some of them may cause damage to samples under test.

To obtain higher resolution, near-field techniques are widely used. In NFMM, the tips used are often in micrometer order, whereas the operating frequency is with a few GHz. Thus, the tips are shorter than half of the wavelength of the radiation they emit, and can be treated as electromagnetically short antennas. Figure 1.1 presents field regions for antennas equal to, or shorter than, one-half wavelength of the radiation they emit, and it suggests that NFMM should work at the near field region since the distance between tip and sample is normally tens of nanometers. In near field region, the diffraction limit is not valid, and the spatial resolution is decided by the size of the source or detector [14]. The reason is that it is the evanescent field that interacts with sample under test in near field region rather than propagating electromagnetic wave. Mathematically, evanescent waves can be characterized by a wave vector where one or more of the vector's components has an imaginary value [35]. Suppose that the wave vector of evanescent wave have the form:

$$\mathbf{k} = k_r\hat{r} + k_z\hat{z} = \beta\hat{r} + j\alpha\hat{z} \tag{1.2}$$

in which $\hat{r}$ and $\hat{z}$ are unit direction in cylindrical coordinate and j is the imaginary unit. The magnitude of wave vector k is calculated as $k = \sqrt{k_r^2 + k_z^2}$. If $\Delta r = \frac{2\pi}{k_r}$ is defined as the spatial resolution in r direction

[2], in propagating electromagnetic wave, it is easy to find $k > k_r$ and $\Delta r > \lambda$, which means the spatial resolution is limited by wavelength. For evanescent wave, since one or more of the wave vector's components has an imaginary value, it is possible that $k < k_r$ and $\Delta r < \lambda$. Therefore, exploiting the near field interaction is able to extend the diffraction limit and obtain higher resolution in NFMM. Additionally, it is noted that this consideration is an alternative explanation of extending diffraction limit in near field region, and, as included in [36], another explanation is concerned with Heisenberg uncertainty principle [37].

Compared with optical microscopy and other microscopy operating at high frequency range, one of the most important advantages of microwave microscopy is the relative simplicity of the detected signal interpretation and experimental instrument implementation [14]. In microwave frequency, the electromagnetic wave interacts with sample in a very straightforward way and the principle can be described by classical electromagnetic theory. On contrary, in optical microscopy, the optical radiation interacts with materials through quantum interactions, plasmon excitation, lattice dynamics, etc., and these interactions are much more complicated [14].

Moreover, compared with atomic-force microscopy (AFM) that mainly measures the topography information of nanostructures [38–42], NFMM has a high resolution image on physical properties including permittivity, conductivity and permeability of sample under investigation [4, 15–18]. In comparison with scanning tunneling microscope (STM), which is an instrument for imaging surfaces at the atomic level [43–48], microwave microscopy measures properties of materials at sub-micron scale, and many emerging phenomena such as phase-separation during metal-insulator transition and quantum spin hall edge states are observed at this length scale [2, 22].

1.2.2 State of the art in NFMM

NFMM technique has been studied extensively in the last two decades, and substantial progress has been made in the aspects of theory, instrumentation, imaging resolution, and data interpretation. This section summarizes state of the art in NFMM including evolution of probes, circuit design, spatial resolution, and applications.

NFMM in S. M. Anlage's group starts from the probe constructed from an open-ended resonant coaxial line which is excited by an applied microwave voltage in the frequency range of $7.5-12.4$ GHz [49], and this simple near-field scanning microwave microscope has a spatial resolution of about 100 μm. In last two decades, probes in his group develop from blunt probe to scanning tunneling microscope (STM) resonant probe [49–56], and the reported spatial resolution is improved from 100 μm to about 100 nm [49, 55–59]. The main applications of NFMM in his group include imaging microwave electric fields from superconducting and normal-metal microstrip resonators [60], measuring local magnetic properties of metallic samples [61], imaging topography of $La_{0.67}Ca_{0.33}MnO_3$ thin film on $LaAlO_3$ substrate [54], and quantitatively measuring dielectric permittivity and nonlinearity in ferroelectric crystals [62].

Probes in M. Tabib-Azar's group mainly include evanescent microwave probe (EMP) with microstripline resonator [63–71] and AFM compatible probe [72]. One advantage of EMP is that, by changing its geometry and frequency of operation, one can easily alter its characteristics for a specific sensing application [69]. It also proves that EMP is able to nondestructively monitor excess carrier generation and recombination process in a semiconductor [71]. The AFM compatible probe consists of a coaxially shielded heavily doped silicon tip and an aluminum (Al) coplanar waveguide,

which can be applied to image embedded nanostructures [72]. Most of the working frequencies in his group are below 4 GHz and the reported spatial resolution is about 50 nm under contact mode and 0.1 μm under non-contact mode. Applications of NFMM in his group are mainly concerned with imaging materials with high conductivity [66, 67], quantifying stress and resistivity change with hydrogen concentration variation [73], mapping temperature distributions [70], detecting depletion regions in solar cell p-n junctions in real time [68], and studying surface electron spin resonance [74].

Golosovsky's group mainly applies resonant-slit probe in near-field millimeter wave resistivity microscope [75–80]. The spatial resolution is better than 100 μm under contactless model [78–80], and 1 μm in slit direction under contact mode [76, 77]. The NFMM technique in his group can be used to test semiconducting wafers, conducting polymers, oxide superconductors, and printed circuits [78], measure ordinary and extraordinary Hall effect [76], and locate heating of biological media [81]. Similarly, in Nozokido's group, slit-type probes are also used to observe the electrical anisotropy in the viewed object [82] and transition phenomena of photoexcited free carriers [83]. Besides slit probes based NFMM, scanning nonlinear dielectric microscope is also used in his group to examine ultrahigh-density storage devices and image the state of spontaneous polarization of a ferroelectric material [84–87].

In Kim and Lee's group [88–91], NFMM begins with a near-field scanning millimeter-wave microscope based on a resonant standard waveguide probe [88]. The waveguide based NFMM has a spatial resolution of about 2 μm, and images thin films by measuring the variation of resonant frequency and quality factor. Then, near-field scanning microwave microscope with a tunable dielectric resonator is developed, which improves the spatial resolution to better than 1 μm [89–91]. The NFMM in their group is mainly applied to

image DNA film in buffer solution [92], investigate space charge properties at the interface of pentacene thin films [93], characterize the sheet resistance of indium-tin-oxide (ITO) thin films [94], and image $YBa_2Cu_3O_y$ thin film on MgO substrate [95].

Scanning tunneling microscope (STM) probe is also used as a point-like evanescent field emitter in Xiang's group [96, 97]. His group achieves a 5 μm spatial resolution [96], and improves it to 100 nm by using phase-sensitive detection and adjusting shifter for 90° out-of-phase between signal and reference [98]. A conducting sphere is used in the same potential to represent the whole tip, and quantitatively measure the dielectric properties [99–101]. Nevertheless, the validity of this analysis requires complete shielding of parasitic near-field components, and the exact tip shape near the apex is also crucial. His group mainly applies NFMM to image dielectric constant profiles [97, 99–101], investigate ferroelectric domains [97, 102–104] and measure low-k dielectric films with varying film thicknesses [105].

Besides NFMM in the above groups, ultratall coaxial tip based on microelectromechanical systems (MEMS) technology is used in Daniel W. van der Weide's group [106]. Z. Popović's group also propose a near-field microwave measurement system which is able to achieve large scan areas (1 mm^2) with micrometer spatial resolution, long-term measurement stability and good signal-to-noise [107], and his group has applied NFMM to investigate monolithic microwave integrated circuit (MMIC). Moreover, Vladimir V. Talanov's group has applied NFMM to measure the lumped-element impedance of a test vehicle [108] for the first time.

Recently, microwave impedance microscopy (MIM), one of the most advanced NFMM, is constructed in Shen's team [2, 3, 6, 7, 15, 19, 22, 109, 110], which is able to make nano-scale images of conductivity and permittivity

of a sample with a spatial resolution better than 100 *nm*. It has wide applications and can be applied to image semiconductor devices, investigate phase separated materials, measure buried structures and image biological specimens. In this thesis, the experimental part is conducted with MIM, and it is particularly introduced in Chapter 2. In addition to the above mentioned groups, Gramse's and Sacha's teams focus on the tip-sample interaction study [21, 111–119], and the comparisons between the work in this thesis and their methods are addressed in Chapter 2 and Chapter 3.

1.2.3 Challenges in NFMM

Although substantial progress has been made in NFMM in last two decades, it remains an area of active research and continues to pose a variety of challenging questions. Among them, solving tip-sample interaction problems, quantitatively extracting properties of materials from measured signals and improving imaging spatial resolution are three urgent issues.

It is difficult to solve tip-sample interaction problem in NFMM due to the complexity of tip geometry and circuits, large computational area for three dimensional samples, and contribution of cantilevers. In this thesis, based on a complete analysis of tip-sample interaction in NFMM, a novel forward solver is developed. As is verified both numerically and experimentally, this solver is general and efficient and at the same time is able to deal with arbitrary tip in three-dimensional setup.

Moreover, although NFMM can receive signals that is related to physical properties of objects under test, most of the studies are limited to qualitative detection. Quantitatively extracting physical information from received signals is still a very challenging task, especially for three dimensional inhomogeneous samples. Till now, quantitative studies have been focusing on

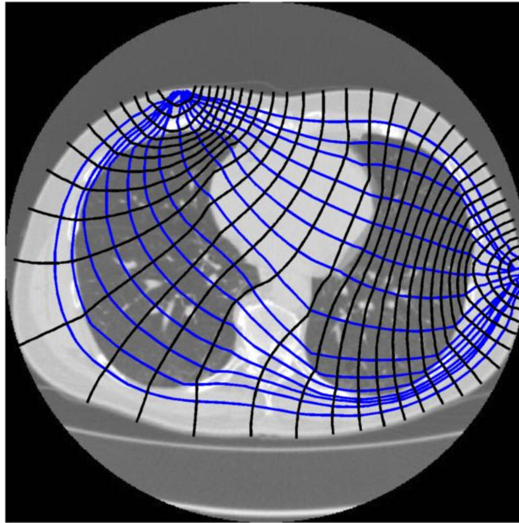

Fig. 1.2 Modeling of a cross section of a human thorax showing current stream lines and equi-potentials from drive electrodes [1].

extracting parameters from a homogeneous media with a constant permittivity or conductivity [113–115], and in comparison, sample information is hardly obtained from inhomogeneous materials. This thesis proposes a nonlinear image reconstruction method based on the above mentioned forward solver to retrieve both permittivity and conductivity information of inhomogeneous samples from measured signals. It is also verified by numerical examples that this method is able to improve imaging resolution as well.

1.3 Electrical impedance tomography problem

Electrical impedance tomography (EIT) is a non-invasive imaging technique in which an image of the internal impedance of the body or subject is reconstructed from the external surface electrode measurements. Since Barber and Brown developed the first EIT device in the early 1980s, electrical impedance tomography has attracted intense interests recently in

geophysics, environmental sciences, medicine, and non-destructive evaluation fields since it is cheap, fast, portable and sensitive to physiological changes [120–123]. Compared with other imaging techniques, such as computerized tomography (CT) scanners, functional magnetic resonance imaging (f-MRI) methods, and ultrasound scanning, EIT is able to provide new and different information such as electrical tissue properties and act as a continuous monitoring technique. Most importantly, only small devices are needed in EIT measurement and no ionising radiation is imposed on users.

Normally, when examining the body part using EIT techniques, people need to attach conducting surface electrodes around the body and apply small alternating current to some of the electrodes. The voltages are recorded from the other electrodes and this process is repeated several times to collect the data for extracting the body information using the reconstruction algorithms. In medicine, EIT is widely used to monitor lung function since the resistivity of lung tissue is much higher than that of other soft tissues within the thorax. Figure 1.2 presents modeling of a cross section of a human thorax showing current stream lines and equi-potentials from drive electrodes [1]. It suggests that equi-potential lines are bent with the variation of conductivity between different organs in the thorax, which means that one can obtain the information of organs by measuring the voltages changes from the electrodes around the body.

Figure 1.3 presents a brief schematic of forward and inverse models in electrical impedance tomography problems. As is depicted in Fig. 1.3, electrical current is injected from the boundary of an object. In EIT forward model, the conductivity distribution is known and the potential distribution needs to be calculated. However, in EIT inverse model, the potential on the boundary is measured and the task is to reconstruct the conductivity

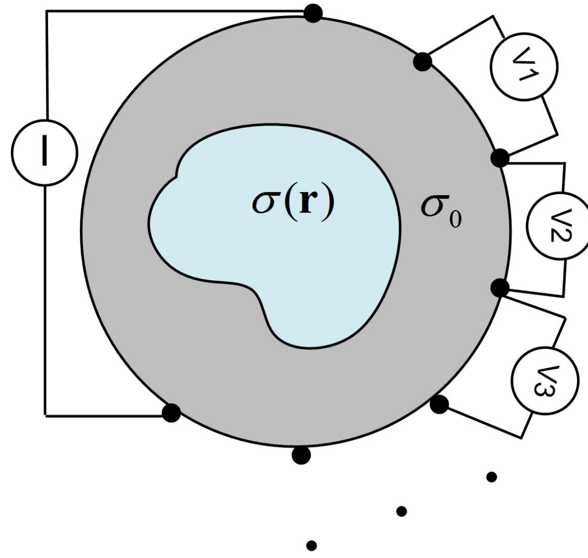

Fig. 1.3 A brief schematic of forward and inverse models in electrical impedance tomography problems.

distribution of the object. Mathematically, EIT inverse problem is a very challenging problem due to its nonlinear and highly ill-posed properties [124, 125]. Till now, many researchers focus on studying the uniqueness of the EIT solution [124, 126–128] and improve the experimental techniques [129, 130]. As a non-invasive medical imaging technique, the algorithm which is fast in reconstructing information of object under test and robust to environmental noise is also crucial [131–135]. In this thesis, studies are focused on the new reconstruction algorithms which are fast and at the same time robust to noise in EIT problem.

1.4 Overview of the thesis

The author's original contribution is presented in the remainder of the thesis, where both of the modeling and inversion are conducted in the framework of Laplace's equation in NFMM and EIT.

In Chapter 2, some challenging problems of tip-sample interaction in

NFMM are discussed. The first part of this chapter presents the electronics of the NFMM used in the experimental part of the study, and both lumped element model method and impedance variation method are used to analyze the experimental system. Then, to deal with tip-sample interaction problems, the Dirichlet Green's function is derived to calculate charges on tips in equivalent-sphere model, and the limitations of equivalent-sphere model have also been discussed. Finally, the concept of effective height is proposed to analyze the contribution of tips in NFMM, which is crucial in numerically solving tip-sample interaction problems for different modes in NFMM.

According to the analysis in Chapter 2, a novel forward solver is proposed for NFMM in Chapter 3, which can be applied to arbitrary tip shapes, thick and thin films, and complex inhomogeneous perturbation. The computational domain for tip-sample interaction problem in the forward solver is reduced to a block perturbation area by applying Green's Theorem, and thus it can save substantial time and memory during calculating either electric field or contrast capacitance for three-dimensional (3D) models of NFMM. It is shown that this method can accurately calculate capacitance variation due to inhomogeneous perturbation in insulating or conductive samples, as verified by both finite element analysis results of commercial software and experimental data from microwave impedance microscopy (MIM). More importantly, this forward solver also provides a rigorous framework to solve the inverse problem which has great potential to improve resolution by deconvolution in NFMM.

Based on the forward solver presented in Chapter 3, a nonlinear image reconstruction method with total variation constraint in NFMM is presented in Chapter 4. The method is fast because it reduces the computational domain for tip-sample interaction problem to a block perturbation area by

applying Green's Theorem in the forward model. Numerical results show that the proposed method can accurately reconstruct the permittivity distribution in three dimensional samples for NFMM. Most importantly, it is found from the results that the resolution has been significantly improved in the retrieved image.

In Chapter 5, two numerical methods are proposed to solve the electric impedance tomography (EIT) problem in a domain with arbitrary boundary shape. The first is the new fast Fourier transform subspace-based optimization method (NFFT-SOM). Instead of implementing optimization within the subspace spanned by smaller singular vectors in subspace-based optimization method (SOM), a space spanned by complete Fourier bases is used in the proposed NFFT-SOM. The thesis studies the advantages and disadvantages of the proposed method through numerical simulations and comparisons with traditional SOM. The second is the low frequency subspace optimization method (LF-SOM), in which the deterministic current subspace and noise subspace in SOM are replaced with low frequency current and the space spanned by discrete Fourier bases, respectively. A detailed analysis of strengths and weaknesses of LF-SOM is also given through comparisons with the above-mentioned SOM and NFFT-SOM in solving EIT problem in a domain with arbitrary boundary shape.

Finally, in Chapter 6, a summary of this thesis is given, as well as suggestions for future work.

Chapter 2

Tip-Sample Interaction in NFMM

2.1 Introduction

In NFMM, as a tip scans over samples, the impedance between tip and ground changes corresponding to the perturbation introduced by the sample under test, and the variation of impedance is detected and recorded in the measured signal. The ultimate goal of quantitative measurement in NFMM is to find the relationship between detected quantities and the sample properties. The processes to achieve this goal can be decomposed into two parts. The first part is to establish the relationship between measured signals and impedance between tip and sample, and the second part is to relate the properties of materials to the impedance between tip and sample, which is also called tip-sample interaction problems in NFMM. This chapter includes solutions for both of the parts, and it is organized as follows.

Section 2.2 introduces basic electronics of the NFMM used in the experimental part of the study, in which both the lumped element model

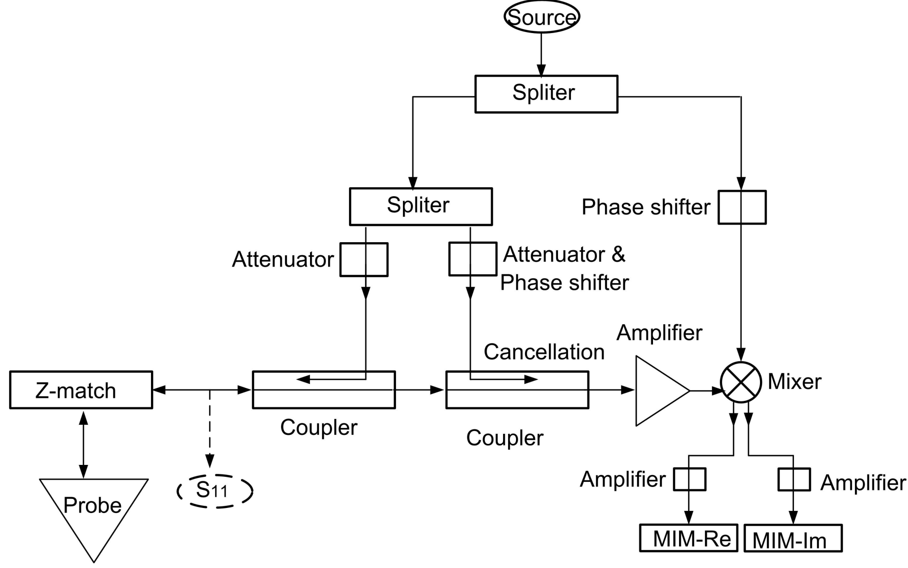

Fig. 2.1 Block diagram of MIM electronics in the reflection mode. [2, 3]

method and the impedance variation method are used to establish the relationship between measured signals and impedance between tip and sample. Then, to deal with tip-sample interaction problems, in section 2.3, Green's function is derived to calculate charge density on tip for equivalent-sphere model, which is the most widely used equivalent model in NFMM. The limitations of equivalent-sphere model have also been discussed in this section. In section 2.4, the concept of effective height is proposed to analyze the contribution of tips in NFMM, and this concept is crucial in numerically solving tip-sample interaction problems for different modes in NFMM.

2.2 Microwave impedance microscopy

In this thesis, the experimental parts are conducted on microwave impedance microscopy (MIM) [2, 3, 6, 7, 15, 19, 22, 109, 110], which is one of the most advanced NFMMs. As is depicted in Fig. 2.1 [2, 3], in MIM, the signal generated from microwave source is divided into two pathes. One path is used as a reference signal for a quadrature mixer, and the other one is further

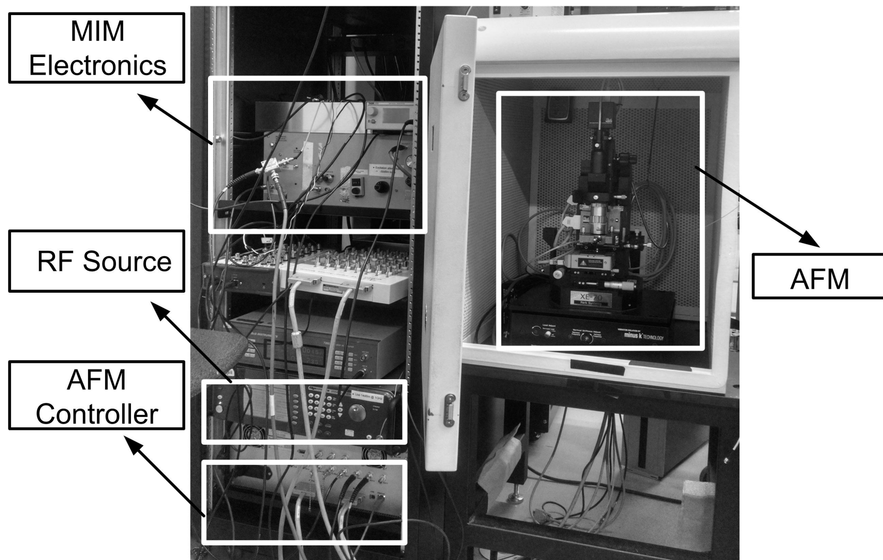

Fig. 2.2 Measurement environment for microwave impedance microscopy with setup and devices [2–4].

divided into two signals. The first one goes to a directional coupler and then to the tip which scans above the sample under test, and there is a z-match circuit between the coupler and tip. The second one is used to cancel common-mode signal [2]. Figure 2.2 shows a photo of experimental setup and devices consisting of AFM, AFM controller, RF Source, and MIM electronics for MIM [4]. In an MIM measurement, GHz voltage modulation is delivered to a metallic tip. When the tip is brought close to and scans across the surface of a sample, variations of tip sample admittance are recorded.

In output part of MIM electronics, a phase shifter is added in the reference signal line to make sure that the output channels, MIM-Re and MIM-Im correspond to the real part ($1/\Delta R$) and imaginary part (ΔC) of the tip-sample admittance variation ($1/\Delta Z$), respectively. The principles that calibration only on the phase is sufficient to guarantee such correspondences are presented as follows. The received reflection coefficient S_{11} at the position between Z-match and coupler in Fig. 2.1 can be expressed as:

$$S_{11} = f(1/R + j\omega C) = f(Y) \tag{2.1}$$

where Y is the tip-sample admittance, then:

$$\frac{dS_{11}}{d(1/R)} = \frac{dS_{11}}{dY}\frac{dY}{d(1/R)} = \frac{dS_{11}}{dY} \tag{2.2}$$

and

$$\frac{dS_{11}}{d(C)} = \frac{dS_{11}}{dY}\frac{dY}{d(C)} = j\omega\frac{dS_{11}}{dY} \tag{2.3}$$

Thus, the differential of S_{11} with respect to differential of $1/R$ and C have a 90° shift, and also a constant ω difference. Considering that the differential of S_{11} is linear with the output of MIM, one only needs to first calibrate some lossless material to get the position of imaginary signal by adjusting the phase in reference signal, which guarantees that imaginary signal corresponds to capacitance variation. Then, the MIM-Re consequently corresponds to real part of the tip-sample admittance variation.

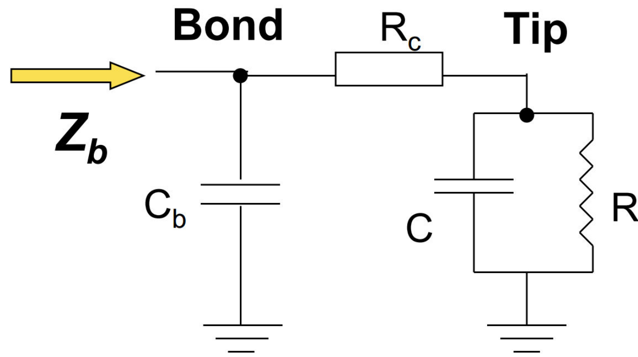

(a)

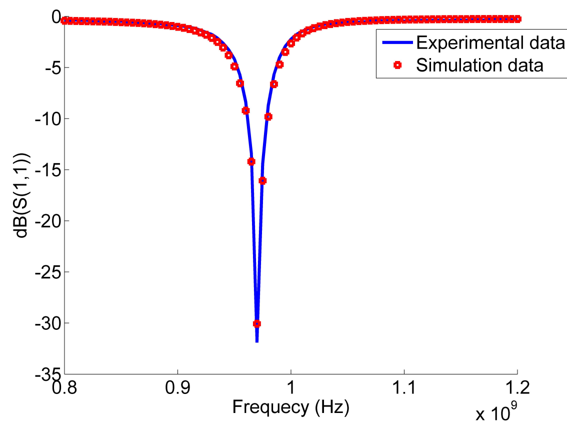

(b)

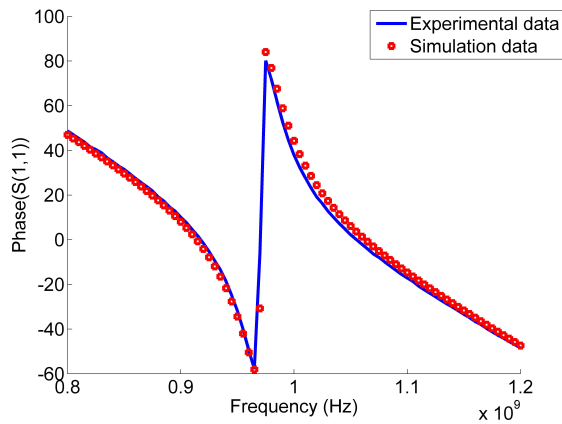

(c)

Fig. 2.3 (a) A lumped element model between Z-match network and ground. (b) Magnitude of S_{11} for experiment and simulation. (c) Phase of S_{11} for experiment and simulation.

2.2.1 Lumped element modeling

Figure 2.3(a) presents a lumped element model for the region between Z-match network and ground. The S_{11} parameter is measured experimentally through vector network analyzer (VNA) at the point between the Z-match circuit and coupler in Fig. 2.1. Then the S11 parameter is loaded into the Advanced Design System (ADS) software as the design goal and the values of capacitance and resistance in Fig. 2.3(a) are optimized such that the calculated S_{11} of the optimized circuit matches the measured S_{11}. Figure 2.3(b) and 2.3(c) present the comparison of magnitude and phase for S_{11} between numerical and experimental results after optimization, respectively, in which $R_c = 5\ \Omega$, $C_b = 1.87\ pF$, $C = 13.5\ fF$, and $R = 2302\ \Omega$ have been obtained through the optimization process.

Although the S_{11} parameter of the established lumped element model matches well with that measured in experiment, the method using lumped element model to analyze tip-sample interaction has its limitations. As is observed in experiment, both the magnitude and phase of S_{11} at the resonant frequency is sensitive to environment effects, which means that a small perturbation may cause dramatic variations in performance of S_{11}. Due to the inevitable experimental error in S_{11}, it is difficult to establish an accurate value for all the components in lumped element model. Thus, lumped element model is only appropriate to qualitatively understand the tip-sample interaction in MIM. To quantitatively evaluate the tip-sample interaction in MIM, a more accurate approach is needed, which will be presented in the next subsection, where the relationship between the impedance variations and MIM signals is studied.

2.2.2 MIM-R and MIM-I channels

In order to quantitatively extract sample information, the relationship between measured signals in MIM and impedance variations between tip and sample is established as follows. For a linear MIM electronic system [2], the relationship between MIM-Re (S_R) and MIM-Im (S_I) signals and the variations of reflection coefficient ΔS_{11} at the position between Z-match and coupler in Fig. 2.1 can be expressed as:

$$\mathrm{S_R} + j\,\mathrm{S_I} \propto \Delta S_{11} \tag{2.4}$$

where ΔS_{11} is the variations due to the perturbation in sample and can be calculated as $S_{11}(Y) - S_{11}(Y_0)$ with Y_0 being the reference impedance, i.e., the impedance between tip and sample without perturbation presented (impedance at the reference point). Take Taylor expansion on $S_{11}(Y)$:

$$S_{11}(Y) = S_{11}(Y_0) + S'_{11}(Y_0)(Y - Y_0) + \dots \tag{2.5}$$

in which the difference between Y and Y_0 is a tiny perturbation compared to the whole impedance between tip and sample. Then, from Eq. (2.5), one can get:

$$\Delta S_{11} \propto \Delta Y \tag{2.6}$$

with $\Delta Y = \Delta 1/R + j\omega\Delta C$. Therefore, the received MIM-Re and MIM-Im have an approximately linear relationship with the variations of impedance between tip and sample:

$$\mathrm{S_R} + j\,\mathrm{S_I} \propto \Delta 1/R + j\omega\Delta C \tag{2.7}$$

Thus, in data interpretation process, one needs to firstly do a calibration to find the linear coefficient between received signals and impedance variations for further sample information analysis. Normally, approach curve method is

used to obtain this coefficient, and details of this method are included in the experimental calibration part of Chapter 3.

2.3 Equivalent-sphere model in NFMM

The previous section has introduced an approach to interpret MIM-Re or MIM-Im signals as impedance variations between tip and sample by exploiting the linear relationship between them. To quantitatively extract sample information, in next step, one needs to solve the tip-sample interaction problem, i.e., to establish the relationship between tip-sample impedance and material properties. As is mentioned previously, this problem is difficult to be numerically solved by traditional method or software due to large computational region for 3D samples. Thus, several equivalent models have been adopted by researchers to model the tip-sample interaction. Among them, the equivalent model which assumes the tip as a small conducting sphere is widely used to solve tip-sample interaction problems especially for thin films [136, 137]. In this section, Green's function is deduced under bispherical coordinate system, in which tip is modeled as a conducting sphere [138].

2.3.1 Bispherical coordinate system

The bispherical coordinate system is defined by [5]:

$$x = \frac{a \sin\eta \cos\phi}{\cosh\mu - \cos\eta} \tag{2.8}$$

$$y = \frac{a \sin\eta \sin\phi}{\cosh\mu - \cos\eta} \tag{2.9}$$

$$z = \frac{a \sinh\mu}{\cosh\mu - \cos\eta} \tag{2.10}$$

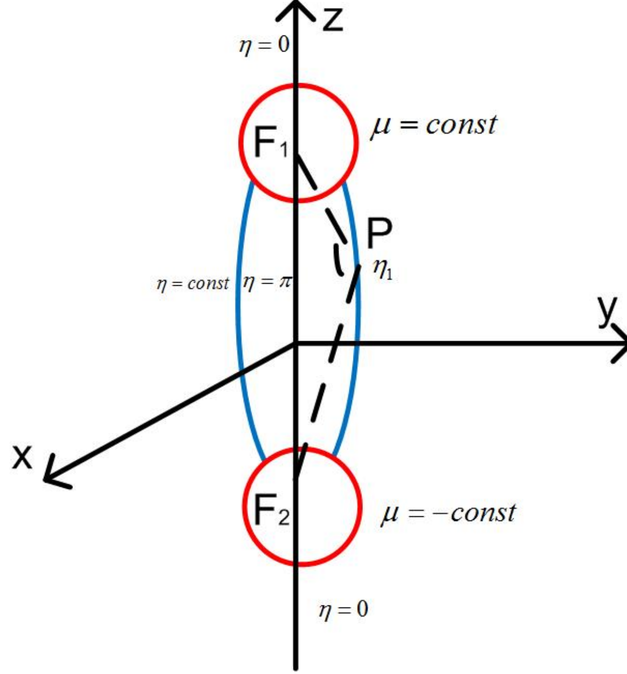

Fig. 2.4 Bispherical coordinate system [5].

$$h_\mu = h_\eta = \frac{a}{\cosh\mu - \cos\eta} \tag{2.11}$$

$$h_\phi = \frac{a\sin\eta}{\cosh\mu - \cos\eta} \tag{2.12}$$

where $0 \le \phi \le 2\pi$, $-\infty < \mu < \infty$, and $0 \le \eta \le \pi$. h_μ, h_η and h_ϕ are the scale factors, and a is the distance between the foci and original point. As is illustrated in Fig. 2.4, those for constant μ_0 represent the spheres surface with center at $z = a\ coth\mu_0$, $x = y = 0$, and radius $R = a|csch\mu_0|$. Those for constant η represent the spindle-shaped surfaces when $\eta > \pi/2$, and apple-shaped surfaces when $\eta < \pi/2$. For any point of P, $\eta = \angle F_1PF_2$ and $\mu = \ln(\frac{|PF_1|}{|PF_{2|}})$.

The transformation relationship of unit vector between bispherical and

Cartesian coordinate can be expressed as:

$$\begin{pmatrix} \hat{\mu} \\ \hat{\eta} \\ \hat{\phi} \end{pmatrix} = \begin{pmatrix} \frac{\frac{\partial x}{\partial \mu}}{h_\mu} & \frac{\frac{\partial y}{\partial \mu}}{h_\mu} & \frac{\frac{\partial z}{\partial \mu}}{h_\mu} \\ \frac{\frac{\partial x}{\partial \eta}}{h_\eta} & \frac{\frac{\partial y}{\partial \eta}}{h_\eta} & \frac{\frac{\partial z}{\partial \eta}}{h_\eta} \\ \frac{\frac{\partial x}{\partial \phi}}{h_\phi} & \frac{\frac{\partial y}{\partial \phi}}{h_\phi} & \frac{\frac{\partial z}{\partial \phi}}{h_\phi} \end{pmatrix} \begin{pmatrix} \hat{x} \\ \hat{y} \\ \hat{z} \end{pmatrix} = M_c \begin{pmatrix} \hat{x} \\ \hat{y} \\ \hat{x} \end{pmatrix} \tag{2.13}$$

where M_c can be calculated as:

$$M_c = \begin{pmatrix} \frac{-2xz}{Q} & \frac{-2yz}{Q} & \frac{-2z^2}{Q} + \frac{R^2+a^2}{Q} \\ -\frac{x\sqrt{4R^2-4z^2}}{Q} + \frac{x}{\sqrt{x^2+y^2}}\frac{R^2-a^2}{Q} & -\frac{y\sqrt{4R^2-4z^2}}{Q} + \frac{y}{\sqrt{x^2+y^2}}\frac{R^2-a^2}{Q} & -\frac{z\sqrt{4R^2-4z^2}}{Q} \\ \frac{-y}{\sqrt{x^2+y^2}} & \frac{x}{\sqrt{x^2+y^2}} & 0 \end{pmatrix} \tag{2.14}$$

with $R = \sqrt{x^2 + y^2 + z^2}$ and $Q = \sqrt{(R^2 + a^2)^2 - (2az)^2}$.

2.3.2 Green's function due to a charge

In NFMM, with the tip-ground voltage applied, the dielectric materials between tip and ground are polarized as dipoles, and these dipoles are secondary sources which further perturb the charge distribution on tip. By measuring the capacitance variation (charge variation) on the tip, one is able to collect the material information under test. Thus, the effect of a dipole on tip charge distribution is critical to solve tip-sample interaction in equivalent-sphere model.

In this part, Green's function in the tip-ground system due to a charge is first derived, in which the potential at the boundary is set to zero for both tip and base, namely the boundary condition in the problem is $\varphi(\mu = 0) = 0$ and $\varphi(\mu = \mu_0) = 0$ where $\mu = 0$ and $\mu = \mu_0$ represent ground plane and boundary of tip, respectively. To obtain the Green's function under this boundary condition, the following Poisson equation needs to be solved:

$$\nabla^2\varphi = -\frac{1}{h_\mu h_\eta h_\phi \varepsilon_0}\delta(\mu - \mu_c)\delta(\eta - \eta_c)\delta(\phi - \phi_c) \tag{2.15}$$

where the subscript c denotes the source point. This is an inhomogeneous partial differential equation, and normally the complete solution of this kind of equation consists of a particular solution of the inhomogeneous equation plus general solution of homogeneous equation. In bispherical coordinates, the Laplacian operator is R-separable, and one can separate the Laplace equation [139] and then get the following particular solution:

$$\varphi_p = \frac{1}{4\pi\varepsilon_0 a}\sqrt{(\cosh\mu - \cos\eta)(\cosh\mu_c - \cos\eta_c)} \cdot F_p \tag{2.16}$$

where

$$F_p = \sum_{n=0}^{\infty}\sum_{m=0}^{n}\varepsilon_m\frac{(n-m)!}{(n+m)!}\cos[m(\phi-\phi_c)]\cdot P_n^m(\cos\eta_c)P_n^m(\cos\eta)\begin{matrix} e^{-(n+0.5)(\mu-\mu_c)}\mu > \mu_c \\ e^{-(n+0.5)(\mu_c-\mu)}\mu < \mu_c \end{matrix} \tag{2.17}$$

in which ε_m is Neumann factor with $\varepsilon_m = 1$ when $m = 0$, and $\varepsilon_m = 2$ when $m > 0$, and $P_n^m(\cos\eta)$ is the associated Legendre function of the first kind. By comparing with this particular solution and considering that φ is finite at surface of $\eta = 0,\ \pi$, the general solution can be expressed as the following form:

$$\varphi_g = \sqrt{(\cosh\mu - \cos\eta)}\cdot\sum_{n=0}^{\infty}\sum_{m=0}^{n}\cos[m(\phi-\phi_c)]\cdot P_n^m(\cos\eta)(Ae^{(n+0.5)\mu}+Be^{-(n+0.5)\mu}) \tag{2.18}$$

where A and B are two coefficients to be determined under the boundary condition.

Taking the boundary condition $\varphi = \varphi_g + \varphi_p = 0|_{\mu=0;\mu=\mu_0}$ into account, the simplified Green's function due to a unit charge under a conducting spherical tip can be expressed as:

$$G_q = \varphi_g + \varphi_p = \sum_{n=0}^{\infty}\sum_{m=0}^{n} -M\sqrt{(\cosh\mu - \cos\eta)}\cdot\cos[m(\phi-\phi_c)]P_n^m(\cos\eta)\cdot F_G \tag{2.19}$$

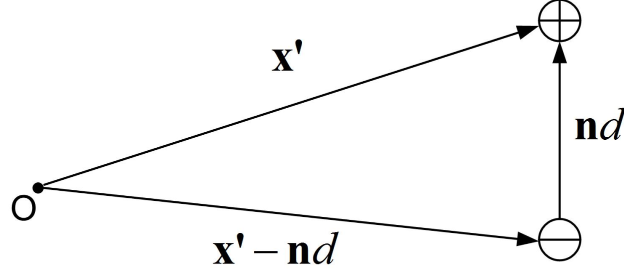

Fig. 2.5 Dipole geometry.

where

$$F_G = \begin{cases} \frac{2\sinh N(\mu_0-\mu)\sinh N\mu_c}{\sinh N\mu_0} & \mu > \mu_c \\ \frac{2\sinh N(\mu_0-\mu_c)\sinh N\mu}{\sinh N\mu_0} & \mu < \mu_c \end{cases} \tag{2.20}$$

and

$$M = -\frac{1}{a}\sqrt{(\cosh\mu_c - \cos\eta_c)} \cdot \varepsilon_m \frac{(n-m)!}{(n+m)!} P_n^m(\cos\eta_c) \cdot \frac{1}{4\pi\varepsilon_0} \tag{2.21}$$

with $N = 0.5 + n$.

2.3.3 Tip charge variation due to a dipole

To calculate the Green's function due to a dipole in equivalent-sphere model, as is illustrated in Fig. 2.5, a dipole consisting of two equal opposite charges with a distance of d is first considered. The potential due to this dipole can be expressed as [140]:

$$\Phi_p(x) = \frac{q}{4\pi\varepsilon_0|\mathbf{x} - \mathbf{x}'|} - \frac{q}{4\pi\varepsilon_0|\mathbf{x} - \mathbf{x}' + \mathbf{n}d|} \tag{2.22}$$

For a small d, one can expand $|\mathbf{x}-\mathbf{x}'+\mathbf{n}d|^{-1}$ using a Taylor series expansion in three dimensions [140]:

$$\frac{1}{|\mathbf{x} + \mathbf{a}|} = \frac{1}{x} + \mathbf{a} \cdot \nabla(\frac{1}{x}) + \cdots \tag{2.23}$$

Thus, as d approaches to zero, the potential becomes:

$$\Phi_p = \frac{1}{4\pi\varepsilon_0}\mathbf{P} \cdot \nabla'(\frac{1}{|\mathbf{x} - \mathbf{x}'|}) = \mathbf{P} \cdot \nabla' G_q \tag{2.24}$$

where $\mathbf{P} = \mathbf{n}qd = \hat{\mu}p_\mu + \hat{\eta}p_\eta + \hat{\varphi}p_\varphi$ is the dipole moment. Thus, in

the bispherical coordinate system, the Green's function due to a dipole is expressed as:

$$G_p = \mathbf{P} \cdot \nabla' G_q = \frac{p_\mu}{h_\mu}\frac{\partial G_q}{\partial \mu} + \frac{p_\eta}{h_\eta}\frac{\partial G_q}{\partial \eta} + \frac{p_\varphi}{h_\varphi}\frac{\partial G_\varphi}{\partial \mu} \tag{2.25}$$

Then, the induced charges on tip due to an arbitrary dipole is calculated as:

$$\rho_s = -\varepsilon\frac{\partial G_p}{\partial n} = \varepsilon(\frac{p_\mu}{h_\mu}\frac{\partial^2 G_q}{\partial \mu^2} + \frac{p_\eta}{h_\eta}\frac{\partial^2 G_q}{\partial \eta \partial \mu} + \frac{p_\varphi}{h_\varphi}\frac{\partial^2 G_\varphi}{\partial \mu \partial \mu}) = \rho_{s\mu} + \rho_{s\eta} + \rho_{s\varphi} \tag{2.26}$$

where $\rho_{s\mu}$, $\rho_{s\eta}$ and $\rho_{s\phi}$ are given as following form:

$$\rho_{s\mu} = \sum_{n=0}^{\infty}\sum_{m=0}^{n} \rho_m(-0.5L_c^{-0.5}\sinh\mu_c \cdot L_0^{0.5} \cdot A_l \cdot N \cdot \sinh N\mu_c + L_c^{0.5} \cdot L_0^{0.5} \cdot A_l \cdot N^2 \cdot \cosh N\mu_c) \tag{2.27}$$

$$\rho_{s\eta} = \sum_{n=0}^{\infty}\sum_{m=0}^{n} \frac{D_e C p_\eta}{h_{\eta_c} h_{\mu_0}} \cos(m(\phi - \phi_c)) P_n^m(\cos\eta) \cdot L_0^{0.5} K_\mu' \tag{2.28}$$

$$\rho_{s\varphi} = \sum_{n=0}^{\infty}\sum_{m=0}^{n} \frac{-M p_\varphi}{h_{\varphi_c} h_{\mu_0}} m \sin(m(\phi - \phi_c)) P_n^m(\cos\eta) \cdot L_0^{0.5} K_\mu' \tag{2.29}$$

with

$$\rho_m = \frac{p_\mu N}{2h_{\mu_c} h_{\mu_0}\pi}\frac{(n+m)!}{(n-m)!} P_n^m(\cos\eta) P_n^m(\cos\eta_c)\epsilon_m \cos(m(\phi - \phi_c)) \tag{2.30}$$

$$K_\mu = \frac{2\sinh N(\mu_0 - \mu)\sinh N\mu_c}{\sinh N\mu_0} \tag{2.31}$$

$$D_e = \frac{1}{2}(\cosh\mu_c - \cos\eta_c)^{-0.5} \cdot \sin\eta_c P_c + (\cosh\mu_c - \cos\eta_c)^{0.5} \cdot P_c{}' \tag{2.32}$$

in which $P_c = P_n^m(\cos\eta_c)$, $C = \epsilon_m(n+m)!/(4a\pi(n-m)!)$, $L_0 = \cosh\mu - \cos\eta$, $L_c = \cosh\mu_c - \cos\eta_c$ and $A_l = 1/Na\sinh(N\mu_0)$. The calculation of h_{μ_c}, h_{μ_0}, h_{η_c}, and h_{φ_c} can be obtained from Eq. (2.11) and Eq. (2.12).

2.3.4 Numerical validation and conclusions

Figure 2.6 presents a typical potential distribution of tip-ground system, in which the 2D axisymmetric electrostatic COMSOL mode analysis is employed to verify the solution in Eq. (2.26) with the consideration that the size of tip

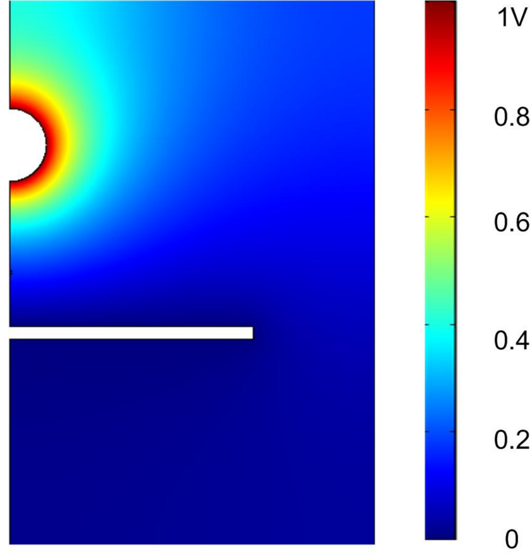

Fig. 2.6 Typical potential distribution of tip-ground system for equivalent-sphere model.

is much larger than the wavelength. Actually, if the operating frequency is 1 GHz, then the wavelength is 0.3 m, which is much larger than a nanometer tip. In simulation, tip is set to be a perfect conducting sphere with radius of $a = 60$ nm having a constant 1 V potential. For convenience, the induced dipole is replaced by a very small dielectric sphere with radius of 3 nm and permittivity of $\varepsilon_r = 10$, where the dipole moment of this sphere can be expressed as [140]:

$$\mathbf{p} = 4\pi\varepsilon_0 a^3 (\frac{\varepsilon_r - 1}{\varepsilon_r + 2})\mathbf{E} \tag{2.33}$$

in which $\mathbf{E}$ is the electric field in absence of dielectric sphere, and has the following relationship with the electrical field inside the sphere ($\mathbf{E}_{in}$).

$$\mathbf{E} = \frac{\varepsilon_r + 2}{3}\mathbf{E}_{in} \tag{2.34}$$

Figure 2.7 shows the surface charge density on the tip of $\phi = 0$ surface induced by a unit dipole placed along the η direction, where position of the dipole is $\mu_c = 2.1$, $\eta_c = \arcsin(\tanh \mu_c)$, and $\phi_c = 0$. The sphere tip is positioned at $\mu = 2.81$. Figure 2.8 shows the surface charge density on the

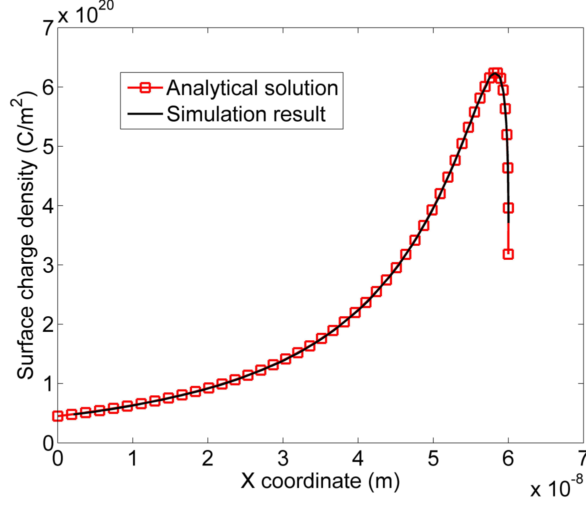

Fig. 2.7 Surface charge density on the tip of $\phi = 0$ surface induced by a unit dipole placed along the η direction, where horizontal coordinate represents the X coordinate of the tip surface.

tip of $\phi = 0$ surface induced by a unit dipole placed along the ϕ direction, where position of the dipole is $\mu_c = 2.1$, $\eta_c = 2\pi/3$, and $\phi_c = 0$. The sphere tip is represented by $\mu = 2.81$. And it is seen that analytical solution matches quite well with simulation results for both cases, which verifies the analytical solution in Eq. (2.26).

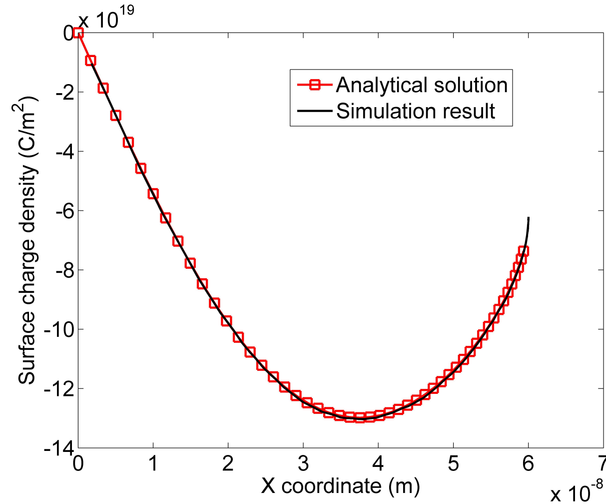

Fig. 2.8 Surface charge density on the tip of $\phi = 0$ surface induced by a unit dipole placed along the ϕ direction, where horizontal coordinate represents the X coordinate of the tip surface.

To sum up, this section has introduced the analytical solution of Green's function which can be used to solve tip-sample interaction problem of equivalent-sphere model in near-field microwave microscopy, and this solution is verified by COMSOL software. However, the equivalent-sphere model has its limitations. As is found by other researchers [112, 114], the accuracy of solving tip-sample interaction problem by replacing a practical tip with a small conducting sphere is questionable when the sample under test is thick. The inaccuracy is due to the important contributions from the upper part of tip. In next section, a concept of effective height is proposed to further study the contributions from the upper part of tip, and the limitations of equivalent-sphere are also verified in experiment by the measurement of microwave impedance microscopy.

To sum up, although approximating a practical tip by a sphere is simple in solving tip-sample interaction problem in NFMM, it has limitations and constraints. A more general and effective approach is needed, and Chapter 3 of the thesis will introduce a novel forward problem solver which is able to effectively solve general tip-sample interaction problem in NFMM.

2.4 Quantitative analysis of effective height of probes in NFMM

As mentioned in last section, equivalent-sphere model has limitations in solving tip-sample interaction problem, and thus many researchers focus on studying numerical methods to solve the problem. Nevertheless, tip-sample interaction problem is difficult to be numerically solved due to the high computational cost involved. This section proposes a concept of effective height which is able to reduce the computational domain of tip-sample

interaction problem.

NFMM typically uses a metallic probe (a tapering tip) to scan across various points ($\vec{r}$) on the surface of a sample while maintaining a tip-sample spacing (l). The sample is typically mounted on an electrical ground surface. The capacitance between the tip and the ground surface $C(\vec{r}, l)$ changes when the tip is near or upon a perturbation in the sample [109, 141, 142], and this is illustrated in Fig. 2.9(a). For convenience, $C(\vec{r}, l)$ is denoted as $C(l)$ unless a mention of scanning point $\vec{r}$ is strictly needed in this study. The capacitance $C(l)$ is a function of the sample properties (permittivity, conductivity and topography), the geometry of the tip, and tip-sample spacing. In general, NFMM measures different quantities under different modes, and the measured parameters are directly related with $C(l)$, $C'(l) = \partial C(l)/\partial l$, and $C''(l) = \partial^2 C(l)/\partial l^2$ under their own mode, respectively.

To accurately model the tip-sample interaction and the measurement quantities is of critical importance to understand the measured signal and isolate or interpret the sample parameters (which are of ultimate importance in microscopy) from the measured quantities. Thus, in general, it is preferred that the measurement quantities are less sensitive to the tip geometry, more sensitive to the perturbations in the sample, and that the tip-sample interaction is easy to model. Several equivalent models have been adopted by researchers for modelling the tip-sample interaction in near-field microwave microscopy. Among them, replacing the tip by a small conducting sphere is widely used to approximate tip-sample interaction [99, 137], but the accuracy of this approximation is questionable, due to the important contribution from the upper part of tip [112, 114] and cantilever [114, 116, 119]. Although the cantilever can be shielded before experiments [7, 110], the computational cost for evaluating tip-sample interaction in numerical model is extremely high due

to the large size of tip cone part.

This section proposes a concept of effective height of tip which is sufficient for modelling the tip-sample accurately for practical purposes. This concept of effective height of tip is very useful in reducing computational area of evaluating tip-sample interaction, determining the sensitivity of the above three capacitance related parameters to the tip height, and explaining the conclusions in previous literatures such as [143, 144]. This approach also exposes the incompleteness of arguments often used in the context of tip-sample interaction for near-field microwave microscopy. Most importantly, the conclusions made in this section are very helpful in improving imaging resolution in NFMM. In experimental part, the validity of the concept of effective height is studied using microwave impedance microscopy [3] that involves pyramid tip with approximately 5.3 μm [6] and circular cone Pt tip with approximately 100 μm [7] measuring thin and thick samples with either dielectric or conducting materials.

2.4.1 Experimental details and analysis approach

Setup: All experiments and numerical results shown here correspond to microwave impedance microscopy [3] setup, a simplified schematic of which is shown in Fig. 2.9(a), where MIM measures a complex valued signal amplified by the microwave circuits.

Tip geometry: An example of tip geometry used in numerical analysis is shown in Fig. 2.9(a), and it can be depicted by tip height H, radius of apex part r, and half cone angle θ. The tip-sample spacing l is the distance between the lowest point of the apex and the upper surface of the sample. As is shown in Fig. 2.10(a) and (b), two probes have been used in experiment, the first probe is a pyramidal probe with the height of approximately $H = 5.3\ \mu m$ and

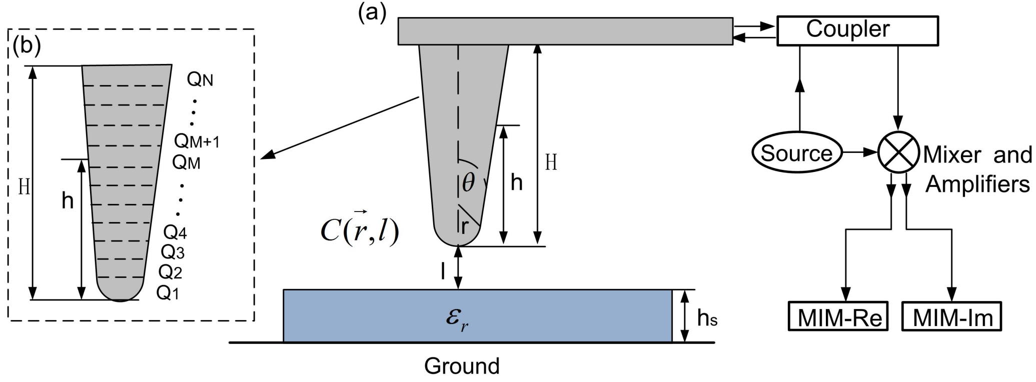

Fig. 2.9 (a) A simple schematic of microwave impedance microscopy with cone-sphere tip. Unless stated otherwise, $H = 15\ \mu m$, $r = 50\ nm$, $\theta = 20°$, $h_s = 200\ nm$, $l = 20\ nm$, and $\varepsilon_r = 3.9$ are used for numerical analysis (Not to scale). (b) Discretization of the tip.

half cone angle $\theta = 35°$ [6]. The second probe is a Pt probe [7] with a height of approximately $H = 100\ \mu m$ and half cone angle $\theta = 6.5°$, where the probe's apex is approximately sphere. The SEM image and detailed information of geometries for both tips have been included in experimental validation part in Fig. 2.10(a) and (b).

Samples: For numerical analysis, any point in the sample is characterized by the relative permittivity ε_r, which may be complex valued if the material at that point is conducting. In general, this section considers the sample as made of silica SiO_2 with relative permittivity $\varepsilon_r = 3.9$ of height 200 nm. If different materials or heights have been used, the details are specified in the relevant results. Samples used in the experiments include bulk homogeneous SiO_2 with the height of 2 μm (thick sample) and aluminum disk with the height of 12 nm on a silicon substrate of thickness 100 nm [110] (thin sample). A thin layer of aluminum dot is assumed to be oxidized and thus composed of aluminum dioxide Al_2O_3.

Analysis approach and implementation details: As discussed before, the analysis approach in this section is based on the effective height which is

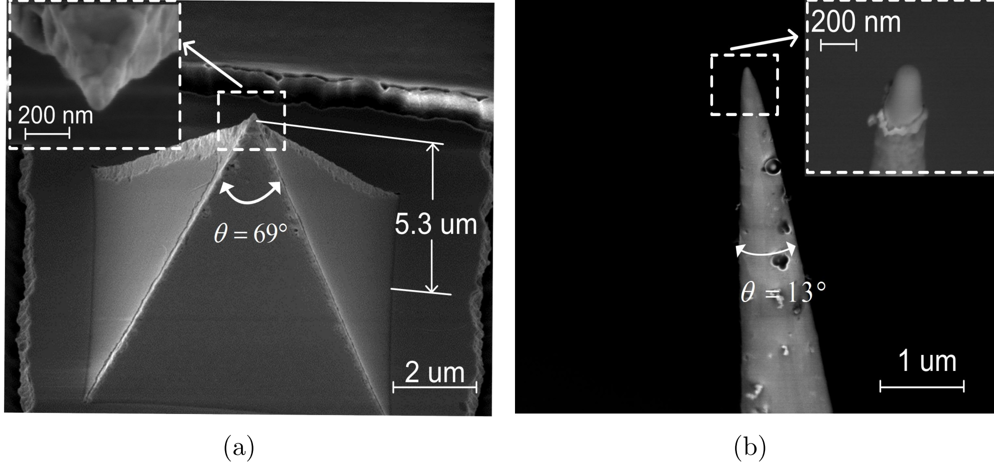

Fig. 2.10 (a) SEM image of the pyramid tip [6] in MIM measurement. (b) SEM image of the Pt tip [7] in MIM measurement.

sufficient for modelling the tip-sample interaction accurately for practical purposes, and the simulation is conducted in COMSOL Multiphysics of concerned parameters under a tip-sample bias of 1 V. To remove large background effects in $C(l)$ and $C'(l)$, whenever $C(l)$ and $C'(l)$ are considered in this section, a reference value $C(l_{ref})$ and $C'(l_{ref})$ at a large tip-sample distance ($l_{ref} = 500\ nm$) have been subtracted from $C(l)$ and $C'(l)$, respectively. For $C''(l)$, the background effects are eliminated by taking the second order derivative of capacitance. In the analysis approach, the cumulative contribution is considered at a variable height h for each parameter. For this purpose, tip is discretized into a total number of N small elements, and, as is depicted in Fig. 2.9(b), the total charges on each element is calculated as Q_1, Q_2, ..., Q_M, Q_{M+1}, ..., Q_N with the Mth element corresponding to a variable height h. Specifically, when the geometry of the whole tip is taken into account, the value of C, C', and C'' at a tip-sample distance l are calculated as $C_H(l)$, $C'_H(l)$, and $C''_H(l)$, respectively. Therefore,

cumulative contribution for C at the height of h can be defined as:

$$C_c(l,h) = \sum_{i=1}^{M} [Q_i(l) - Q_i(l_{ref})]/C_H(l) \times 100\% \tag{2.35}$$

Similarly, C' at the height of h is defined by finite difference as:

$$C'_c(l,h) = \sum_{i=1}^{M} D_i/C'_H(l) \times 100\% \tag{2.36}$$

with

$$D_i = \frac{[(Q_i(l+\Delta l) - Q_i(l-\Delta l)) - (Q_i(l_{ref}+\Delta l) - Q_i(l_{ref}-\Delta l))]}{2\Delta l} \tag{2.37}$$

where Δl is a small perturbation of tip-sample distance, and cumulative contribution for C'' at the height of h is defined as:

$$C''_c(l,h) = \sum_{i=1}^{M} \frac{[Q_i(l+\Delta l) - 2Q_i(l) + Q_i(l-\Delta l)]}{\Delta l^2}/C''_H(l) \times 100\% \tag{2.38}$$

It is evident that $h = 0$, and $h = H$ are the two extremes which correspond to zero contribution and 100% contribution, respectively, to any parameter. The effective height h_e is further defined as the height h at which the cumulative contribution is 98%. Obviously as shown in Fig. 2.9(b), the upper cone part need not to be modelled when the effective height h_e of a practical tip used in experiment is smaller than the tip height H, and thus complexity involved with the large size of the tip can be dispensed away.

2.4.2 Results and discussions

2.4.2.1 Cumulative contribution of $C'(h)$, $C'(h)$, and $C''(h)$

Figure 2.11(a) and 2.11(b) present the cumulative contribution of $C(h)$, $C'(h)$, and $C''(h)$ for the typical model illustrated in Fig. 2.9(a) with tip-sample spacing $l = 20$ nm. It is noted that the results presented in Fig. 2.11 follow the same general trends for other values of tip-sample spacing. The value $l = 20$ nm is used because small tip-sample spacing implies very strong

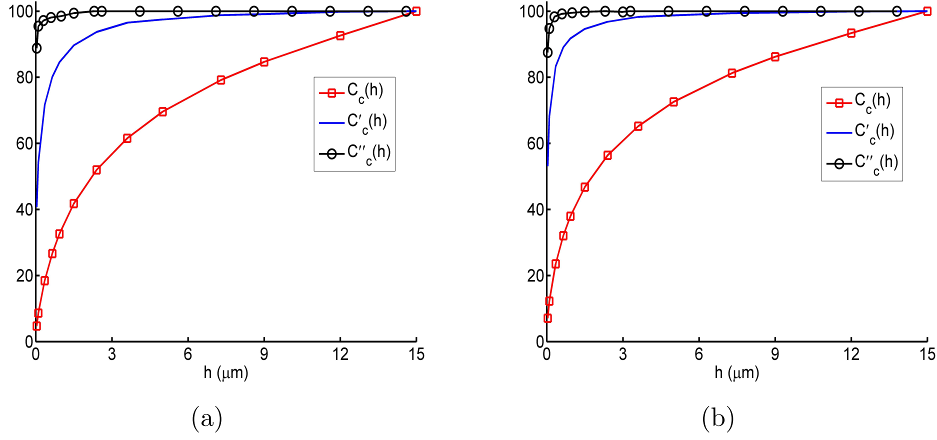

Fig. 2.11 Cumulative contribution of $C(h)$, $C'(h)$, and $C''(h)$ for the typical model illustrated in Fig. 2.9(a) for (a) dielectric material and (b) metal.

coupling between the sample and tip. It is found from Fig. 2.11(a) that the apex part of the tip (which corresponds to the first point with $h = 0.033\ \mu m$) contributes approximately 5.5%, 55% and 89% to the total value for $C''(h)$, $C'(h)$, and $C''(h)$ when dielectric material is considered, respectively.

Another remarkable phenomenon is that the upper cone part contributes barely to the total value of $C'(h)$ and $C''(h)$, whereas it keeps contributing to the value of $C(h)$. The reason is that the upper cone part is far away from the sample and ground, and can be treated as stray capacitance which is approximately linear to tip-sample distance l [114, 118]. Therefore, the capacitance contribution from the upper part can be expressed as $C_{up} = Kl + c$, in which K and c are constant coefficients related with tip geometries and sample properties. For $C'(h)$ and $C''(h)$, the stray capacitance from upper cone part is either subtracted by taking a reference point or eliminated by taking the second order derivative, whereas the upper cone part keeps contributing to C even when it is far away from the sample. Thus, considering the effective height is only meaningful when $C'(h)$ and $C''(h)$ is evaluated. As is shown in Fig. 2.11(a), the effective heights h_e of the dielectric materials

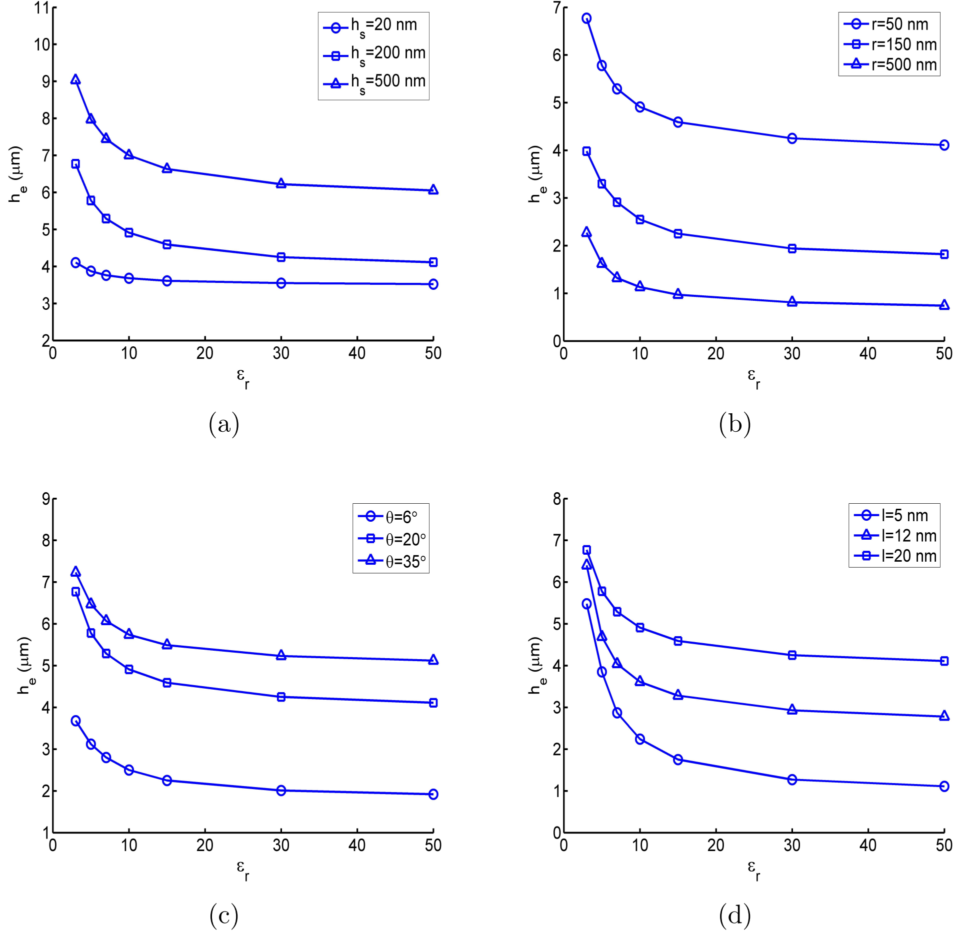

Fig. 2.12 Effective height for C' as a function of relative permittivity (ε_r) for (a) three different sample heights $h_s = 20\ nm$, $h_s = 200\ nm$, $h_s = 500\ nm$, (b) three different apex radii $r = 50\ nm$, $r = 150\ nm$, and $r = 500\ nm$, (c) three different tip half-cone angles: $\theta = 6°$, $\theta = 20°$, and $\theta = 35°$, and (d) three different reference distances $l = 5\ nm$, $l = 12\ nm$, and $l = 20\ nm$. Unless stated otherwise in each case, all the other parameters are the same as that in Fig. 2.9(a).

in Fig. 2.9(a) are 4.7 μm and 0.6 μm for $C'(h)$ and $C''(h)$, respectively. Compared with dielectric materials, it is found from Fig. 2.11(b) that the lower part of the tip contributes more to the total value when metal is considered, which results in a smaller effective height for both $C'(h)$ and $C''(h)$. Specifically, when the dielectric materials are replaced by metal, the effective height for $C'(h)$ and $C''(h)$ are 2.2 μm and 0.3 μm, respectively, and

it is also noted that the most upper part contribution still cannot be neglected for $C(h)$ even when the material under the tip is perfect conductor.

As compared to C', it is concluded that the effective height of C'' is much smaller and it is also found that the C'' has larger contribution from the apex of the tip, with other parameters being the same, thus making it better suited to extract localized sample information below the apex and to provide improved imaging resolution of NFMM. The results in Fig. 2.11(a) and (b) also explain the conclusion in [143, 144] that the force gradient (proportional to C'') has better resolution than that of force (proportional to C') mode in electrostatic force microscopy (EFM). On contrary, compared with C'', one of the advantages of C' is that it is easier to evaluate either in numerical software or experiment since C'' requires a second order derivative with respect to tip-sample distance l.

2.4.2.2 Effective height of $C'(h)$ and $C''(h)$

As is mentioned previously, this section considers the effective height h_e of the tip for different sample properties, tip geometries, and tip-sample distances, and the results have been presented in Fig. 2.12(a)-(d). It is found from Fig. 2.12(a) that, as a general result, h_e is a decreasing function of the relative permittivity ε_r and an increasing function of sample height h_s. It is also noted that h_e increases fast when ε_r is smaller than 5, and becomes almost independent from ε_r when relative permittivity is larger than 30. Figure 2.12(b) and (c) show the effects of tip geometries by considering different apex radii and half cone angles, and it is seen that tips with larger r and smaller θ have smaller effective height. With other parameters unchanged, larger apex radius means larger area of lower part of the tip and thus contribution comes more from that part for such tips. Moreover, the effects of tip-sample

distances on effective height are considered, and the results are shown in Fig. 2.12(d). It suggests that the model with smaller tip-sample distance has smaller effective height for the interaction concentrates more on the apex part.

In table 2.1, the effective height h_e of $C''(h)$ for typical tips and samples is presented, and it is found that the effects of relative permittivity, sample height, apex radius, half cone angle and tip-sample distance have on the effective height for $C''(h)$ are very similar to that for $C'(h)$. Whereas, compared with C', h_e is much smaller when C'' is considered.

Since the effective heights for both $C''(h)$ and C' vary in a small range with the changes of tip geometries and sample properties, it is easy for us to determine approximate values of h_e based on Fig. 2.12(a)-(d) and table 2.1 to model tip-sample interaction problems concerned with different kinds of tips and materials practically. Specifically, to calculate the effective height h_e of a practical setup, one need to first determine an initial value of effective height h_0 according to the half cone angle of the practical tip θ from Fig. 2.12(c) and the first three rows of table 2.1 without consideration of the effects of tip radius and the thickness of sample. The half apex angel θ is in the range of $6^\circ \leq \theta \leq 35^\circ$. Then, an adjustment e_1 is added on h_0, i.e., $h_e = h_0 + e_1$, following the relation $e_1 \approx 7(h_s - 200) - 330(r - 50)^{0.4}$ and $e_1 \approx 1.1(h_s - 200) - 51(r - 50)^{0.4}$ for C' and C'', respectively, in which all the units are nanometers and tip radius and sample thickness are in the range of $50\ nm \leq r \leq 500\ nm$ and $h_s \leq 2\ \mu m$, respectively. In addition, it should be noted that the empirical formulas of effective height are not valid for the "tip" that has a larger bottom part but a smaller upper part.

Table 2.1 Effective height h_e of $C''(h)$ for typical tips and samples in NFMM (Units: μm).

	ε_r	3.5	5	7	10	15	30	50
$h_s = 200\ nm$,	$\theta = 6°$	0.27	0.24	0.22	0.21	0.2	0.2	0.2
$l = 20\ nm$,	$\theta = 20°$	0.67	0.54	0.46	0.41	0.38	0.35	0.34
$r = 50\ nm$	$\theta = 35°$	1.08	0.91	0.79	0.71	0.64	0.58	0.56
$h_s = 200\ nm$,	$r = 20\ nm$	0.93	0.82	0.74	0.69	0.65	0.6	0.59
$l = 20\ nm$, $\theta = 20°$	$r = 100\ nm$	0.35	0.37	0.23	0.21	0.2	0.18	0.18
$h_s = 200\ nm$,	$l = 30\ nm$	0.83	0.72	0.64	0.59	0.55	0.51	0.5
$r = 50\ nm$, $\theta = 20°$	$l = 40\ nm$	0.96	0.84	0.77	0.71	0.67	0.64	0.62
$r = 50\ nm$, $\theta = 20°$	$h_s = 300\ nm$	0.8	0.65	0.57	0.51	0.48	0.45	0.44
$l = 20\ nm$,	$h_s = 20\ nm$	0.41	0.38	0.36	0.35	0.34	0.33	0.32

2.4.3 Experiment validation

In the first example, experiment is conducted using a long Pt tip [7] with the height of approximately 100 μm to measure both bulk SiO_2 and Al dot sample [110] with microwave impedance microscopy (MIM). The detailed information and SEM image of the Pt tip [7] are presented in Fig. 2.10(a). For bulk SiO_2 sample, it is homogeneous and the height of it is about 2 μm, as is presented in Fig. 2.13(a). In simulation, the effective height h_e of C' for SiO_2 is first determined based on the equation $h_e = h_0 + e_1$, in which $h_0 \approx 3.5\ \mu m$ and $e_1 \approx 12.5\ \mu m$ are obtained from Fig. 2.12(c) and the expression for e_1 in previous section, respectively. Then, a truncated tip with $H = 16\ \mu m$ is used to replace the practical Pt tip when C' is evaluated in COMSOL Multiphysics (2D AC/DC electrostatic module). It is found from Fig. 2.13(a) that simulation results agree well with experiment results when using a truncated tip with $H = 16\ \mu m$ to model a practical Pt tip with $H \approx 100\ \mu m$. Figure 2.13(a) also presents the simulation results from a equivalent-sphere tip model of which the radius is equal to the apex radius of Pt tip. It suggests that discrepancies are found between experimental and simulated results from the equivalent-sphere model, which indicates that

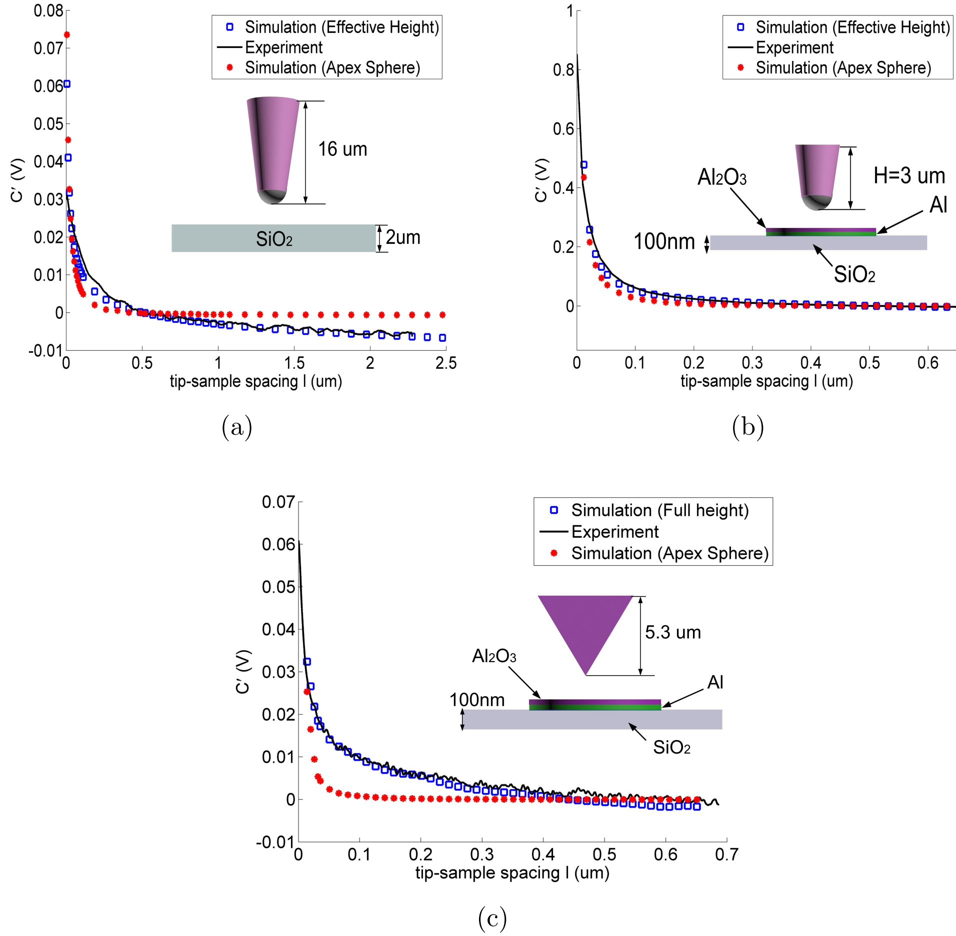

Fig. 2.13 C' as a function of tip-sample spacing l with Pt tip measuring (a) bulk SiO_2 and (b) Al dot sample for both simulation and experiment results. (c) C' as a function of tip-sample spacing l with pyramid tip measuring Al dot sample for both simulation and experiment results. (Blue square denotes the simulation results from the truncated tip with effective height; Black line denotes the experimental results; Red star denotes the simulation results from equivalent-sphere tip of which the radius is equal to apex radius of practical tip.)

replacing the tip by a small conducting sphere is not accurate in modeling the tip-sample interaction.

For Al dot sample, as is shown in Fig. 2.13(b), there is a layer of oxide with height of $2-5$ nanometers formed on Al with the height of $12-15$ nanometers and the substrate layer is SiO_2 with the height of approximately 100 nm. In simulation, the effective height of C' for Al dot sample is first

calculated as 3 μm, and a truncated tip with $H = 3\ \mu m$ is used to replace the practical Pt tip when C' is evaluated in COMSOL Multiphysics for Al dot sample. As is presented in Fig. 2.13(b), it suggests that the simulation results match perfectly with experiment results when C' is evaluated for Al dot sample. Similarly, the results obtained from the equivalent-sphere tip model are also compared with experimental results in Fig. 2.13(b), and it suggests that discrepancies exist between experimental and simulated results obtained by equivalent-sphere model.

Further experiment is conducted using a pyramid tip [6] with the height of 5.3 μm to measure Al dot sample. The detailed information and SEM image of the pyramid tip [6] are depicted in Fig. 2.10(b). Since the geometry of the pyramid tip is not axisymmetric, three dimensional (3D) COMSOL Multiphysic module has to be applied to solve tip-sample interaction in simulation. By calculating the effective height h_e according to the equation $h_e = h_0 + e_1$ in previous section, it is found that the tip height $H = 5.3\ \mu m$ is not large enough to make us use truncated tip in simulation to model the practical tip. Thus, the complete pyramid tip with $H = 5.3\ \mu m$ is used in simulation, and Fig. 2.13(c) presents the performance of both simulation and experiment results as a function of tip-sample spacing l for C'. It is found that the results match well between experiment and simulation, but the performance is not good when replacing the whole tip by a small conducting sphere of which the radius is equal to the apex radius of the pyramid tip. Apparent discrepancies are found between experimental and simulated results obtained by equivalent-sphere model, which further verifies the inaccuracy of using equivalent-sphere model to model the tip-sample interaction in MIM.

2.5 Summary

This chapter mainly studies the approach to quantitatively interpret sample properties from measured quantities in NFMM, which can be decomposed into two issues. The first issue is to determine the relationship between measured quantities and tip-sample impedance, and in this chapter, an impedance variation based method is proposed to solve this problem. The second issue is to establish the relationship between tip-sample impedance and material properties, i.e., to solve the tip-sample interaction problem, which is the most crucial part in quantitatively extracting properties of materials from measured signals.

To deal with tip-sample interaction problem, Green's function is firstly derived to calculate charges on tips in equivalent-sphere model, and the solution is verified by COMSOL software. The analytical solution of Green's function can help us comprehend the principles behind NFMM, such as the effects of each geometry parameter on tip charge variations. Moreover, compared with numerically calculating Green's function, the usage of analytical solution saves a lot of time and computer memory. The limitations of equivalent-sphere model are also discussed in this chapter.

Then, to reduce computational region of evaluating tip-sample interaction in numerical method and to determine the sensitivity of the capacitance related quantities to the tip height, a concept of effective height is proposed to analyze the contribution of tips in NFMM. The original contributions of the "effective height" section are summarized as follows. Firstly, it is found that the effective height for the first and second derivative of capacitance with respect to vertical distance is much smaller than the one for the capacitance, which has the advantage of greatly reducing the computational complexity.

Secondly, the effective height of C' and C'' considering a wide range of tip and sample information is established, which is helpful to quickly and approximately estimate the effective height of other practical tips. Thirdly, this section has discussed the effects of relative permittivity, sample height, apex radius, half cone angle and tip-sample distance have on the effective height, and the concept of effective height provides a unified solution to explain some important conclusions in previous literatures. Fourthly, all the conclusions in this section provide very helpful instructions for improving imaging resolution in NFMM, since a small effective height is in correlation to a small area of sample that contributes to measured signal, i.e., better resolution.

Additionally, although the concept of effective height is able to reduce computational cost to some extent, the full numerical solution of tip-sample interaction problems is challenging because it still involves complex 3D geometries that cover a wide range of sizes, from nanometric contribution of the sample features to micrometric contribution of the tip. The next chapter will introduce a novel method based on finite element-boundary integral to further reduce the computational domain.

Chapter 3

A Novel Forward Solver in NFMM

3.1 Introduction

As introduced in previous chapter, replacing the tip by a small conducting sphere is widely used to approximate tip-sample interaction [99, 137], but the accuracy of this approximation is questionable, due to the important contribution from the upper part of tip [112, 114]. Besides the equivalent-sphere model, approximate analytical solution is also used in solving tip-sample interaction problem [21, 145], but the tip geometry is limited to very few specific types [146–148]. More importantly, fabricated tips can hardly be of a rigorously regular shape in practice, which further makes the approximate analytical solutions inaccurate and inflexible. Also, the above two methods are mainly used to calculate homogeneous samples and can hardly be applied to samples with inhomogeneous perturbation presented.

Another well-known approach is to obtain the capacitance between a metallic tip and an inhomogeneous sample using a boundary integral

method [149], but quantitatively speaking, the results can hardly be accurate especially when the perturbation in sample is inhomogeneous due to approximations made in the theoretical part of the method. Moreover, an algorithm called generalized image charge method (GICM) [150] has also been developed and widely used. It has been applied to evaluate electrostatic interaction between the tip and metallic nanowire over the surface by using the Green's function of segment [151], and to calculate electric field at very small tip-sample distances [152]. Nevertheless, the models used in these papers are 2D symmetric, and when the setup of tip-sample interaction is asymmetric, the approach can hardly be accurate since it is derived under symmetric setup.

Therefore, a fast, accurate and general approach to evaluate the tip-sample interaction with arbitrary tip and inhomogeneous perturbation is yet to be realized, and this chapter proposes an approach based on finite element-boundary integral (FE-BI) methods to fill this gap [4, 153]. Based on the fact that only a limited region beneath the tip contributes to the tip-sample capacitance in NFMM [153], the computational domain of tip-sample interaction problem can be reduced to a block area by applying Green's Theorem in the proposed method, and it is fast when computing a 3D tip-sample interaction problem for both insulating and conductive sample. Contrast capacitance due to various perturbations is calculated using this method and compared with both numerical results obtained by commercial software and experimental images of MIM.

In an MIM measurement, GHz voltage modulation is delivered to a metallic tip, usually of pyramid shape with a base length of about 5 μm and an apex diameter of nearly 50 nm [6]. When the tip is brought close to and scanned across the surface of a sample, variations of tip-sample admittance are recorded, the imaginary and real parts of which are denoted as MIM-Im and

MIM-Re signals, respectively. For samples under test the major contribution of impedance perturbation comes from variations of dielectric constant and conductivity. Semi-quantitative information of local permittivity or electrical conductivity is obtained by comparing MIM data to admittance-permittivity or conductivity curve (response curve) simulated in commercial finite analysis software. Usually a 2D axisymmetric model of a cone-shaped tip on a large homogeneous sample is used to calculate the admittance between the two, whereas a point-by-point full 3D simulation remains impractical due to extremely large computational cost. A fast, general method of calculating admittance between arbitrary tip and inhomogeneous samples is therefore highly desirable for experiments.

This chapter is organized as follows. Section 3.2 describes the theoretical principle of the forward solver, and proposes an approach to implement it. In section 3.3, the results are presented when the perturbation in sample under test is inhomogeneous, and the image of capacitance variation due to an "H" shape perturbation structure is shown. Also, the computation time of applying the proposed method in solving the scanning problems is compared with that of using COMSOL Multiphysics. To further demonstrate the FE-BI based forward solver, the image of a buried sample obtained by MIM in experiment is compared with capacitance variation computed by the proposed method in section 3.4. Finally, original contributions of this chapter are summarized in section 3.5.

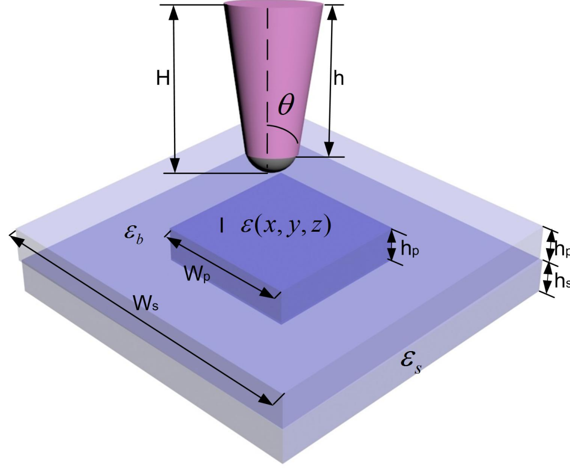

Fig. 3.1 A typical near-field microwave microscopy scheme including geometry and parameters used in the calculation of this chapter: $H = 5\ \mu m$, $h = 0.485\ \mu m$, $\theta = 30°$, $W_p = 1.2\ \mu m$, $W_s = 6\ \mu m$, $h_p = 0.4\ \mu m$, tip sample distance $l = 20\ nm$, and $h_s = 0.6\ \mu m$ (Not to scale).

3.2 Theory and principle of forward solver

3.2.1 Model description

The geometry and parameters used in the calculation are sketched in Fig. 3.1, and this section considers a widely used cone-sphere tip which is depicted by the height of the whole tip H, height of cone h, and half cone angle θ. It is noted that the tip can be of arbitrary geometry and the cone sphere tip is chosen as an example to present the modeling. In this thesis, frequency is set to be 1 GHz unless otherwise stated. A three-dimensional sample with two layers is considered in this chapter. One layer is called feature layer which is a cuboid region with height h_p and width W_s, another one is a bottom surface grounded substrate layer with height h_s and width W_s. All perturbations are located inside a finite region in the feature layer, which is denoted as the domain I.

Here, the domain I is chosen as a cuboid with width W_p and height h_p.

Outside the domain I, other regions of feature layer and substrate layer are filled with known materials and here SiO_2 with relative permittivity of 3.9 is used for both of them as an example in this chapter. In this model, it is assumed that the top surface of the sample is flat and the distance between the bottom of tip and the top surface of sample is l.

3.2.2 Calculation of potential

Under a tip-sample bias of 1 V, the background potential, i.e., with the absence of perturbation, is denoted as $\phi_i(r)$. The task is to calculate the change in capacitance, referred to as contrast capacitance, when perturbation is present. The model in this chapter calculates the potential inside domain I using finite element method (FEM) and deals with the potential outside via the boundary element method (BEM). In domain I, the potential satisfies the following equations:

$$\nabla \cdot (\varepsilon(r)\nabla\phi(r)) = 0 \tag{3.1}$$

For dielectric samples, $\varepsilon(r)$ is a real value representing permittivity of sample, whereas for conductive materials, $\varepsilon(r)$ is replaced by $\varepsilon(r) - j\sigma(r)/\omega$ with $\sigma(r)$ and ω to be electrical conductivity and angular frequency, respectively. Following the finite element method [154], domain I is discretized into rectangular brick elements, and Eq. (3.1) can be discretized as:

$$\overline{\overline{K}} \cdot \overline{\phi} - \overline{\overline{B}} \cdot \overline{q}_b = 0 \tag{3.2}$$

where $\overline{\overline{K}}$ and $\overline{\overline{B}}$ are evaluated as integral over domain I element and its boundary element respectively. $\overline{q}_b$ is corresponding to potential derivative at the boundary with $\overline{q}_b = \frac{\partial\overline{\phi}_b}{\partial n'}$, where $\overline{\phi}_b$ and n' are the potential on the boundary and outer normal direction of the boundary, respectively. According to Green's Theorem, the electrical potential in the exterior region of domain

I satisfies the following equation [140]:

$$\begin{aligned}\phi(r) &= \phi_i(r) + \oint_s [G(r,r')\varepsilon(r')\frac{\partial \phi(r')}{\partial n'} \\ &\quad -\phi(r')\varepsilon(r')\frac{\partial G(r,r')}{\partial n'}]dr' \end{aligned} \tag{3.3}$$

where s and n' are the boundary of domain I and its inward normal direction, respectively. $G(r,r')$ is the potential due to a unit charge (Green's function) in the background medium, i.e., when there is no perturbation presented in the sample. Under most cases, $G(r,r')$ has no analytical solution but it can be evaluated numerically easily using commercial software. In detail, the Green's function $G(r,r')$ is calculated as:

$$\nabla \cdot (\varepsilon(r)\nabla G(r,r')) = -\delta(r-r') \tag{3.4}$$

The physical meaning of $G(r,r')$ is the potential at the position of r due to a unit point charge at the position r'. Thus, for the case when there is no analytical solution, it can be numerically calculated by putting a unit charge at the position of r' and evaluate the potential at r. For calculating $\partial G(r,r')/\partial n'$, one only needs to replace the charge with a dipole [140] due to reciprocity principle.

Following the discretization method in FEM, the potential $\overline{\phi}_b$ on boundary of domain I satisfies the following equation by applying collocation method to Eq. (3.3):

$$\overline{\overline{H}} \cdot \overline{\phi}_b + \overline{\overline{G}} \cdot \overline{q}_b = \overline{b} \tag{3.5}$$

where $\overline{\overline{H}}$ and $\overline{\overline{G}}$ are calculated as integrals of $\partial G(r,r')/\partial n'$ and $G(r,r')$ over boundary element of domain I, respectively, and $\overline{b}$ is corresponding to $\phi_i(r)$ on the boundary of domain I. By combining Eq. (3.2) and Eq. (3.5), the potential on the boundary of domain can be easily solved.

3.2.3 Calculation of contrast capacitance

A homogeneous sample which excludes the perturbation is chosen as a reference model to obtain reference capacitance C_{ref} between tip and ground. Contrast capacitance (denoted as $C_{contrast}$), which is defined as the difference between capacitance in the presence of perturbation and C_{ref}, is evaluated in this chapter. The proposed method to calculate contrast capacitance in this chapter can also be directly applied to calculate capacitance derivative with respect to tip sample distance (dC/dl), which is a parameter widely used in electrostatic force microscopy [111–113, 155, 156]. One only need to calculate capacitance for two different tip-sample distances, and then use finite difference to calculate dC/dl. Other parameters related with capacitance in NFMM, such as d^2C/dl^2 [117, 136, 143], can also be calculated in a similar way.

To calculate contrast capacitance between tip and ground, N is defined as the inward normal direction of tip surface. Taking derivative of both sides in Eq. (3.3) with respect to N, integrating it over the tip, and then multiplying both sides by the permittivity of air, Eq. (3.3) becomes:

$$\Delta_\phi = \oint_{tip}\oint_{s} [\varepsilon_0 \frac{\partial G(r,r')}{\partial N}\varepsilon(r')\frac{\partial \phi(r')}{\partial n'}]\mathrm{d}r dT - \oint_{tip}\oint_{s} [\varepsilon_0 \frac{\partial(\partial G(r,r')/\partial n')}{\partial N}\phi(r')\varepsilon(r')]\mathrm{d}r dT \tag{3.6}$$

in which

$$\Delta_\phi = \oint_{tip} [\varepsilon_0 \frac{\partial \phi(r)}{\partial N} - \varepsilon_0 \frac{\partial \phi_i(r)}{\partial N}]\ dT \tag{3.7}$$

For Δ_ϕ, an integral of $\varepsilon_0 \partial\phi(r)/\partial N$ and $\varepsilon_0\partial\phi_i(r)/\partial N$ over tip surface are total charges on the tip with and without perturbation presented, respectively. Since the voltage on tip is 1 V, the left hand side of Eq. (3.6) is directly equal to the contrast capacitance defined in section previously. On the right hand

side of Eq. (3.6), if one changes the integral order, it is easy to get the contrast capacitance between tip and ground due to the presence of perturbation in sample:

$$\begin{aligned} C_{contrast} &= \oint_{s} [G_c(r,r')\varepsilon(r')\frac{\partial \phi(r')}{\partial n'} \\ &\quad -\phi(r')\varepsilon(r')\frac{\partial G_c(r,r')}{\partial n'}]dr' \end{aligned} \tag{3.8}$$

where $G_c(r,r')$ and $\partial G_c(r,r')/\partial n'$ can be calculated as the total charges on the tip due to a unit charge (Green's function) and dipole in background, respectively. In detail,

$$G_c(r,r') = \oint_{tip} \varepsilon_0 \frac{\partial G(r,r')}{\partial N}\ d\mathrm{T} \tag{3.9}$$

It is obvious from the definition of $G(r,r')$ in Eq. (3.4) that the physical meaning of $G_c(r,r')$ is the total charges on the tip due to a unit charge. Similarly, when there is no analytical solution for $G_c(r,r')$ and $\partial G_c(r,r')/\partial n'$, they can be calculated by evaluating the total charges on the tip when a unit charge and dipole are presented, respectively.

For Eq. (3.8), using the same process in discretizing Eq. (3.3), contrast capacitance on tip can be evaluated as:

$$C_{contrast} = -\overline{L}^T \cdot \overline{\phi}_b - \overline{M}^T \cdot \overline{q}_b \tag{3.10}$$

The matrices $\overline{L}$ and $\overline{M}$ are calculated as integrals of $G_c(r,r')$ and $\partial G_c(r,r')/\partial n'$ over boundary element of domain I, and the superscript T denotes the transpose operator. For the perturbation with conductive materials presented, capacitance variation will be frequency dependent. The relationship between charges on the tip and capacitance is:

$$Q(\omega) = \frac{I(\omega)}{j\omega} = V(\omega)(-j\frac{G_{ts}(\omega)}{\omega} + C(\omega)) \tag{3.11}$$

where G_{ts} is the conductance between tip and sample. Under a tip-sample

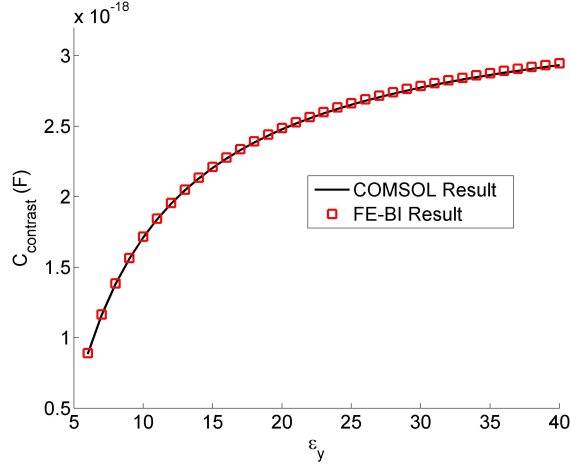

Fig. 3.2 Contrast capacitance due to the perturbation of domain I which is filled with homogeneous oxide with relative permittivity ε_x for both FE-BI method and COMSOL values.

bias of 1 V, capacitance is equal to the real part of $Q(\omega)$, and combined with Eq. (3.10), one can get:

$$C_{contrast}(\omega) = Re(-\overline{L}^T \cdot \overline{\phi}_b - \overline{M}^T \cdot \overline{q}_b) \tag{3.12}$$

where Re denotes taking the real part of a complex value. Similarly, considering the relationship between $Q(\omega)$ and G_{ts}, contrast conductance is obtained from Eq. (3.10):

$$\Delta G_{ts}(\omega) = Im[(\overline{L}^T \cdot \overline{\phi}_b + \overline{M}^T \cdot \overline{q}_b)\omega] \tag{3.13}$$

with Im denotes taking the imaginary part of a complex value.

3.3 Numerical validation

3.3.1 Contrast capacitance at one scanning point

Contrast capacitance is evaluated using the FE-BI approach (denoted as C_{fe}) in this chapter and compared with simulation result of COMSOL software (denoted as C_{com}). The first example is concerned with contrast capacitance

due to the perturbation of domain I which is filled with homogeneous oxide with relative permittivity ε_x for both FE-BI and COMSOL values, and, as is illustrated in Fig. 3.2, it shows a good agreement between them when ε_x varying from 6 to 40. Relative error, which is defined as $|C_{fe} - C_{com}|/|C_{com}|$, is below 0.4% in Fig. 3.2.

In the second example, domain I is filled with four layers of perturbation as shown in Fig. 3.3(a), and each layer has a height of $h_n = 100\ nm$. The materials filled in each layer are alumina, an unknown oxide, glass and silicon with relative permittivity set to be 9.3, ε_y, 6 and 11.7, respectively. Contrast capacitance due to this four layers perturbation from both FE-BI and COMSOL results, with ε_y varying from 6 to 40, is presented in Fig. 3.3(b). In Fig. 3.3(c), certain oxide is replaced by conductive materials with relative permittivity of 16 and conductivity of σ varying from 0.02 S/m to 7.82 S/m. It is found that contrast capacitance calculated by FE-BI approach agrees excellently with that by finite element software for both insulating and conductive perturbation with relative error smaller than 0.6%.

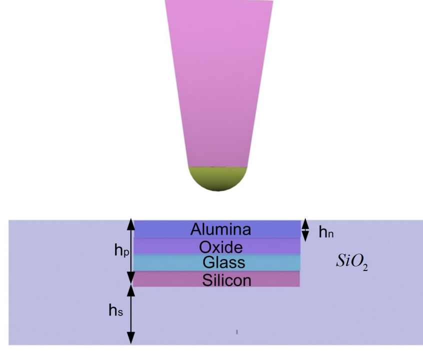

(a)

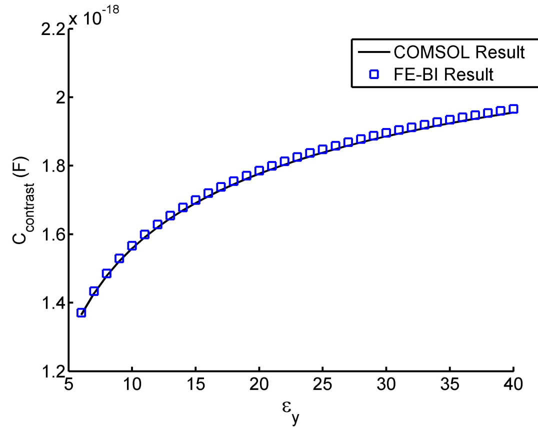

(b)

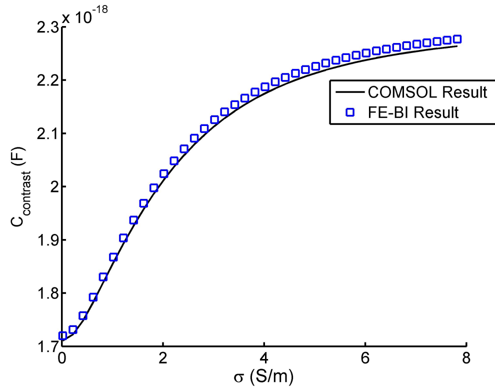

(c)

Fig. 3.3 (a) The side view of a sample with four layers of perturbation filled in domain I. Each layer has a width of W_p and height of h_n and these four layers are filled with alumina, some certain oxide, glass and silicon, respectively. (b) Capacitance variation due to the four layers of perturbation sample depicted in Fig. 3.3(a) for both FE-BI method and COMSOL when changing ε_y from 6 to 40 and (c) changing the conductivity of the second layer from 0.02 S/m to 7.82 S/m.

3.3.2 Effective interaction area

In order to show that the contribution of contrast capacitance in tip-sample interaction comes primarily from the perturbation of a limited window (effective interaction area) beneath the tip [153], silicon with permittivity of 12 is filled in domain I. The width W_p of perturbation domain I is gradually increased from a small value to 5 μm while other parameters are kept unchanged. Again, C_{ref} is calculated as the capacitance when there is no perturbation presented ($W_p = 0\ \mu m$).

Figure 3.4 shows the contrast capacitance normalized to $W_p = 5\ \mu m$ as a function of W_p for three different half cone angles of tip, and Fig. 3.5 shows the normalized contrast for three different substrate heights h_s. Conclusions can be drawn that the contrast capacitance increases when the size of perturbation domain I is enlarged, but it saturates when W_p reaches some certain value. The conclusions suggest that only a limited region (effective interaction area) beneath the tip contributes to the contrast capacitance. Besides, from Fig. 3.4, it is found that with a sharp tip the contrast capacitance increases faster to saturation than that with a blunt tip, which means that the response on a

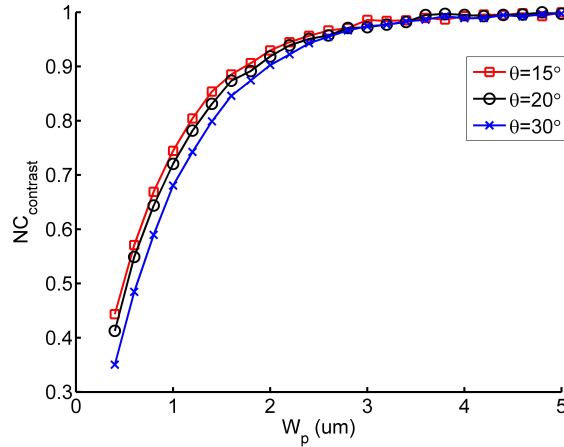

Fig. 3.4 Contrast capacitance normalized to $W_p = 5\ \mu m$ as a function of W_p for three different half cone angles of tip.

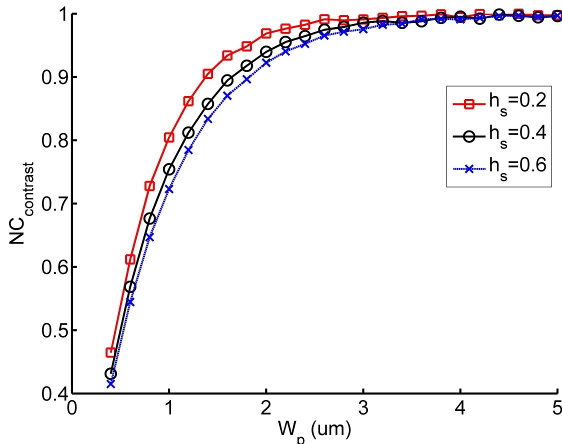

Fig. 3.5 Contrast capacitance normalized to $W_p = 5\ \mu m$ as a function of W_p for three different substrate heights h_s.

blunt tip comes from a larger region beneath the tip. This conclusion suggests that under the same condition, high resolution will be achieved for a sharper tip. From Fig. 3.5, it is seen that, comparing with a thick sample, a thin film is easier to achieve higher resolution with other parameters being the same. This conclusion suggests that if it is possible, one should reduce the thickness of sample under test to achieve better resolution in experiment. One physical reason behind these conclusions is that the electric field concentrates more between the tip and ground for a sharper tip or thinner sample.

Another point to be addressed is that in Fig. 3.4 and 3.5, the perturbation domain I is full of perturbation materials, but in practice perturbation normally comes from only a fraction of the domain I, for example, perturbations are often particles or stripes. Further simulation results also show that, in the latter case, it is much easier for contrast capacitance to reach saturation point comparing with the former case. This is due to the fact that for such small perturbation particles or stripes, the perturbation contribution decreases faster when it is farther away from the tip.

To summarize, for situations where perturbation materials occupy only a fraction of the domain I, the computational window beneath the tip can be chosen to be a smaller domain. Further simulation also suggests that for most of the sample in experiment, W_p corresponding to $NC_{contrast} = 80\%$ is good enough for computing contrast capacitance.

3.3.3 Contrast capacitance at different scanning points

In this example, a three dimensional sample with an "H" shape perturbation is considered, and a cone-sphere tip is applied to scan over this three dimensional structure with a certain tip-sample distance l. The substrate area is filled with SiO_2 while perturbation region is filled with certain oxide with relative permittivity of 16. The calculation is done with a finite-element package COMSOL 4.3 3D solver and the result is used as a benchmark to compare with the FE-BI results obtained by the method in this chapter. In the calculation of contrast capacitance using FE-BI method, at each scanning point, a window with width of 1.2 μm beneath the tip is considered as the perturbation region

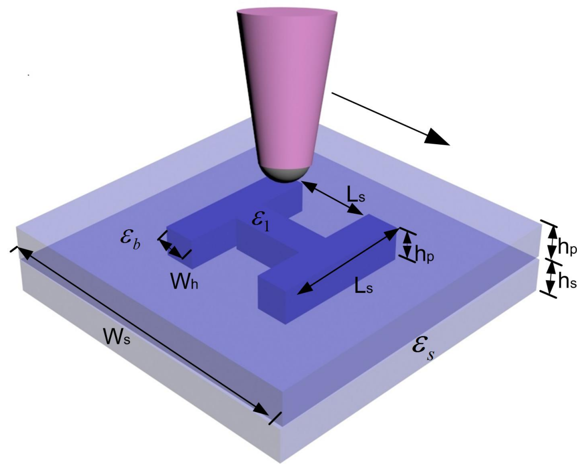

Fig. 3.6 Cone-sphere tip scans over a three dimensional sample with an "H" shape perturbation presented ($W_p = 100\ nm$ and $L_s = 400\ nm$).

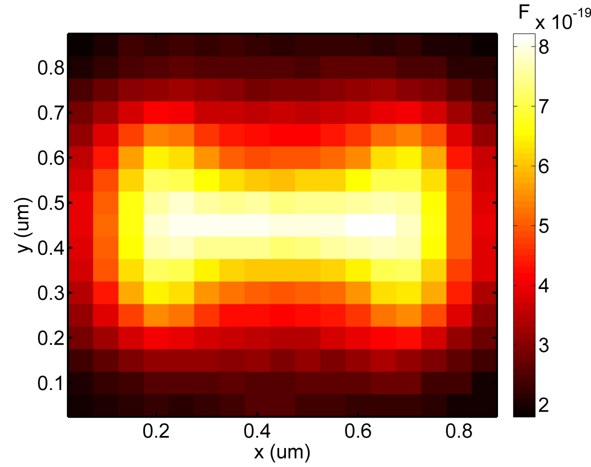

Fig. 3.7 Contrast Contrast capacitance image when tip scans over "H" shape perturbation (simulation results from COMSOL).

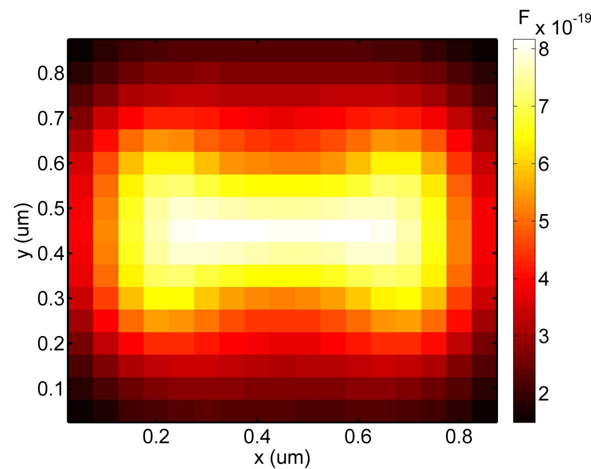

Fig. 3.8 Contrast Contrast capacitance image when tip scans over "H" shape perturbation (results from FE-BI method).

which contributes to the contrast capacitance.

Figure 3.7 presents the contrast capacitance image when the tip scans over the sample shown in Fig. 3.6 in COMSOL, and Fig. 3.8 shows the counterpart obtained by the proposed FE-BI method, where it is seen that both results agree with each other perfectly. If same computers and discretizations on domain I are used, for such a pattern, it takes about 130 minutes and more than 30 GB RAM to finish the simulation in COMSOL whereas it takes only about 18 minutes and 1 GB RAM using the stored Green's function

to compute the contrast capacitance applying the method introduced in this chapter. It suggests that the proposed method has great advantage in the scanning of 3D structure over commercial software.

Moreover, even if the structures (here, the “H” pattern) fabricated in the same substrate have been changed, one can directly compute the perturbation on the tip without re-storing the Green’s function. Another important advantage of the method in this chapter is that it can be directly applied to inverse problem, and the properties of unknown materials can be reconstructed by solving the inverse problem. By comparing with the exact pattern shown in Fig. 3.6, it is seen from Fig. 3.7 and 3.8 that the perturbation response on a tip is actually a convolution from a region beneath the tip rather than just from a single pixel beneath the tip. If one can reconstruct the materials properties by deconvolution, the resolution can be noticeably improved.

3.4 Experimental validation

Figure 3.9 presents a two layer standard sample for measuring the dielectric response of microwave impedance microscopy. In the measurement, a pyramid tip with the height of 5.3 μm , angle of 69° and apex diameter approximately

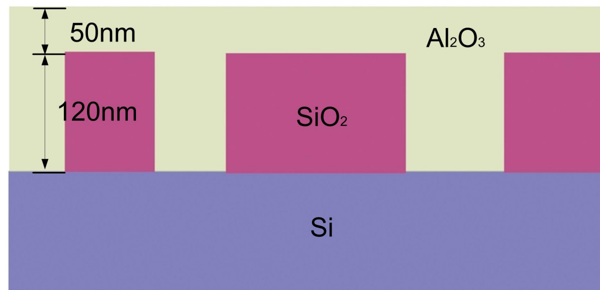

Fig. 3.9 Side view of a buried sample structure, and SiO_2 is buried in Al_2O_3 layer with a specific pattern.

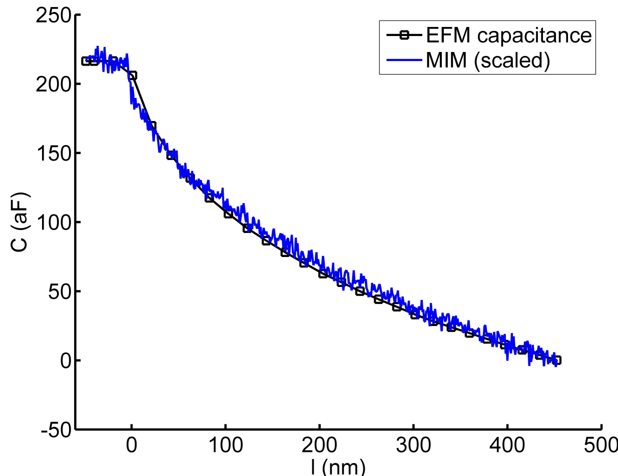

Fig. 3.10 Capacitance varying with tip-sample distance (l) for both EFM and MIM (scaled). The horizontal axis denotes the tip-sample distance.

of 50 nm is used and the schematic of the pyramid tip is depicted in Fig. 2.10(a) [6]. The sample under test consists of a doped Si layer and Al_2O_3 layer with permittivity of 9, and SiO_2 with permittivity of 3.9, buried in Al_2O_3 layer with a specific pattern.

In experiment, electrostatic force microscopy (EFM) is used to calibrate the signal of MIM [118, 157]. In one mode of MIM, measured signal is directly proportional to capacitance between tip and ground. Thus, as is presented in Fig. 3.10, if taking tip-sample approach curves at the same scanning point by both EFM and MIM, the approach curves can be matched between them by a scaling factor (620 aF/V) on MIM. Thus, one is able to directly convert measured signal into capacitance images when tip scans across the sample in Fig. 3.9 using the scaling factor.

Since there is always an arbitrary offset in the experiment, one needs to take capacitance difference between two different tip-sample distances to eliminate it. Figure 3.11(a) presents the capacitance difference image between tip-sample distance of 0 nm and 200 nm measured by microwave impedance microscopy. Although there are some small discontinuities due to drifts in

experiment, it is found that the buried structure pattern is clearly resolved. In FE-BI part, contrast capacitance at a tip-sample distance of 0 nm and 200 nm is calculated. Fig. 3.11(b) shows capacitance difference between tip-sample distance of 0 nm and 200 nm obtained by the FE-BI method in this chapter. Except for some small discrepancies due to stains in sample and drifts in experiment, it is found that capacitance difference measured by experiment matches well with results calculated by FE-BI method. The data (denoted as A) in the scanning area of Fig. 3.11(a) is also extracted, and compared with the value of capacitance difference (denoted as B) at the same positon in Fig. 3.11(b). It is found that the relative error, which is calculated as $|A - B|/|B|$, is as small as 3.05%.

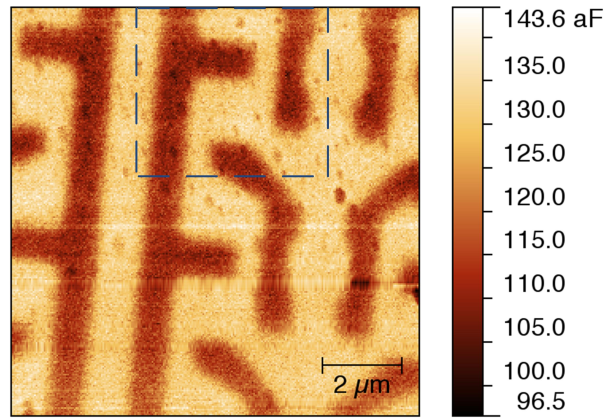

(a)

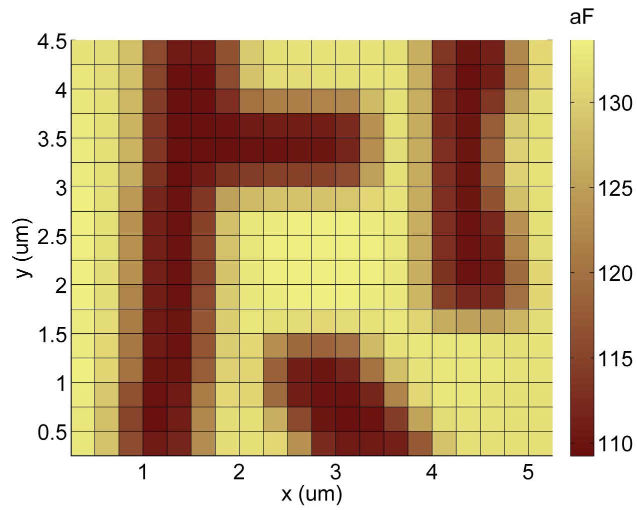

(b)

Fig. 3.11 (a) Capacitance difference between tip-sample distance of 0 nm and 200 nm measured by MIM (dash-line rectangular represents the specific calculation area in FE-BI method). (b) Capacitance difference between tip-sample distance of 0 nm and 200 nm computed by FE-BI method in this chapter. Each pixel has an area of $0.25 \times 0.25\ um^2$.

3.5 Summary

In this chapter, a hybrid numerical method combing boundary element and finite element methods is used to reduce the computational domain of tip-sample interaction in NFMM into a box (the domain I). The associated computational costs are largely reduced in tip-sample interaction problem. The principles behind the approach are firstly derived in this chapter, and then the proposed approach is verified by both numerical and experimental methods in this chapter. The original contributions of the method proposed are summarized as follows.

The first advantage of this approach is that it can be directly applied to scanning microscopy and saves considerable time and memory. For different scanning points, the region that perturbs the tip-ground capacitance is limited to a box (the domain I) beneath the tip and consequently for the materials outside this region one can treat them as known homogeneous material due to their negligible contribution to contrast capacitance. Thus, Green's function is not changed for different scanning points, and one only needs to change the value of $\overline{\overline{K}}$ matrix that depends on the properties of perturbation materials during the scanning process. To conclude, the proposed method reduces the three-dimensional computational domain to the computational box (i.e., the aforementioned effective region) beneath the tip, which avoids using FEM to compute the whole computational domain (whatever between the tip and the ground) during the scanning process. To simulate three-dimensional tip-sample interaction for scanning points, the proposed method is much faster than brute force all-domain methods.

The second advantage of this approach is that the framework is applicable to various models regardless of the tip shape, sample type and perturbation

material, and the results are very accurate. For different setting of tips and samples, one only needs to calculate the corresponding Green's function on the boundary of effective region. When analytical Green's function is not available, one can numerically calculate it and then save it in the library. Note that the numerical evaluation of Green's function is needed only once for a given experimental setup, and will not change during the scanning process.

The third and most important advantage is that this rigorous approach can be directly applied to inverse problem in next chapter, where one is able to reconstruct the materials properties from received signal of NFMM by deconvolution and noticeably improve resolution.

Chapter 4

Nonlinear Image Reconstruction with Total Variation in NFMM

4.1 Introduction

As is stated previously, most of the studies in NFMM are limited to qualitative detecting, and it is still a very challenging task to quantitatively extract physical properties such as permittivity and conductivity of materials from received signals, especially for three dimensional inhomogeneous samples [113–115, 158]. In this chapter, based on the above mentioned forward problem solver, a fast nonlinear image reconstruction method using conjugate gradient (CG) algorithm with total variation constraints [158] is presented to quantitatively restore both permittivity and conductivity information of inhomogeneous samples from capacitance variation signals. Numerical results show that the proposed method can accurately reconstruct the permittivity distribution in three dimensional samples under test. More importantly, it

is also found that, by reconstructing the permittivity and conductivity of samples from the received capacitance signals, the imaging resolution can be highly improved in NFMM.

This chapter is organized as follows. Section 4.2 describes the theoretical principle of the reconstruction method, and introduces an efficient CG based approach with total variation constraints. In section 4.3, the numerical results for various samples under test are presented, and it is shown that the proposed method is able to restore permittivity and conductivity from capacitance variation and improve resolution in NFMM. Finally, the main original contributions and future work are included in section 4.4.

4.2 Inverse formulation

In the inverse problem, the contrast capacitance between tip and sample is measured at every scanning point, whereas the permittivity or conductivity distribution of the sample is unknown and has to be determined.

Defining the matrix $\overline{\overline{P}}$, which picks up the boundary nodes out of all nodes, the potential at the boundary $\overline{\phi}_b$ is obtained by combining Eq. (3.2) and Eq. (3.5):

$$\overline{\phi}_b = \overline{\overline{P}} \cdot \overline{\phi} = \overline{\overline{P}} \cdot \overline{\overline{K}}_\varepsilon \cdot \overline{\overline{B}} \cdot \overline{\overline{G}}^{-1} \cdot \overline{b} \tag{4.1}$$

with

$$\overline{\overline{K}}_\varepsilon = (\overline{\overline{K}} + \overline{\overline{B}} \cdot \overline{\overline{G}}^{-1} \cdot \overline{\overline{H}} \cdot \overline{\overline{P}})^{-1} \tag{4.2}$$

Therefore, the contrast capacitance ΔC_i at the ith scanning point is obtained by

$$\Delta C_i = -\overline{L}^T \overline{\phi}_b - \overline{M}^T \overline{q}_b = (\overline{M}_1 + \overline{M}_3) \cdot \overline{\overline{K}}_\varepsilon^i \cdot \overline{M}_2 + M_4 \tag{4.3}$$

where $\overline{M}_1 = -\overline{L}^T \cdot \overline{\overline{P}}$, $\overline{M}_2 = \overline{\overline{B}} \cdot \overline{\overline{G}}^{-1} \cdot \overline{b}$, $\overline{M}_3 = \overline{M}^T \cdot \overline{\overline{G}}^{-1} \cdot \overline{\overline{H}} \cdot \overline{\overline{P}}$, and

$M_4 = -\overline{M}^T \cdot \overline{\overline{G}}^{-1} \cdot \bar{b}$. $\overline{\overline{K}}_\varepsilon^i$ is the value of $\overline{\overline{K}}_\varepsilon$ at the ith scanning point, and it is also the only term which is related with the unknown permittivity ε in Eq. (4.3). Then, a nonlinear least squares cost function corresponding to the residue between measured contrast capacitance and the predicted one is defined:

$$f_c = \sum_{i=1}^{S} (\Delta C_i - \Delta C_i^m)^2 \tag{4.4}$$

where ΔC_i^m is the measured contrast capacitance at the ith scanning point, and S represents the total number of scanning points. Since the sample considered is piecewise constant, the total variation regularization is defined [158]:

$$T(\varepsilon) = \int_I \sqrt{|\nabla \varepsilon|^2 + \alpha^2} dI \tag{4.5}$$

where ε is the predicted permittivity, and α is a small positive constant to keep $T(\varepsilon)$ differentiable at $\varepsilon = 0$. Specifically, the total variation T of a discrete imaging with a $M \times M$ sampling grid is expressed as [159, 160]:

$$\begin{aligned} T(\varepsilon) \quad = \quad & \sum_{i,j=0}^{M-2} \sqrt{|\varepsilon_{i+1,j} - \varepsilon_{i,j}|^2 + |\varepsilon_{i,j+1} - \varepsilon_{i,j}|^2 + \alpha^2} \\ & + \sum_{i=0}^{M-2} \sqrt{|\varepsilon_{i+1,M-1} - \varepsilon_{i,M-1}|^2 + \alpha^2} \\ & + \sum_{j=0}^{M-2} \sqrt{|\varepsilon_{M-1,j+1} - \varepsilon_{M-1,j}|^2 + \alpha^2} \end{aligned} \tag{4.6}$$

Therefore, one is able to define the objective function with a total variation regularization term as:

$$f(\varepsilon) = \sum_{i=1}^{S} (\Delta C_i - \Delta C_i^m)^2 + \beta T(\varepsilon) \tag{4.7}$$

where β is a regularization parameter to be adjusted in optimization process [161–163]. The unknown permittivity in sample under test is reconstructed by minimizing the objective function in Eq. (4.7).

4.3 Implementation procedures

In the inverse procedures, conjugate gradient (CG) method is used to minimize the objective function in Eq. (4.7), and the implementation procedures of this nonlinear inverse problem are detailed as follows.

- Step 1) Calculate $\overline{M}_1$, $\overline{M}_2$, $\overline{M}_3$, and $\overline{M}_4$ in Eq. (4.3).
- Step 2) Initial step, $n = 1$; Give an initial guess of $\overline{\varepsilon}_0 = \overline{\varepsilon}_b$, and $\overline{\varepsilon}_b$ is the background permittivity.
- Step 3) Determine the search direction: Calculate the matrix term $\overline{\overline{K}}^i_\varepsilon$, objective function $f(\overline{\varepsilon}_n)$, and gradient of objective function $\overline{g}(\overline{\varepsilon}_n) = \partial f(\overline{\varepsilon}_n)/\partial \overline{\varepsilon}_n$. Then determine the Polak-Ribière-Polyak (PRP) directions [164]: If n=1, the search direction $\overline{\rho}_1$ is $\overline{\rho}_1 = -\overline{g}_1$. Otherwise, $\overline{\rho}_n = -\overline{g}_n + (\mathrm{Re}[(\overline{g}_n - \overline{g}_{n-1})^* \cdot \overline{g}_n]/||\overline{g}_{n-1}||^2)\overline{\rho}_{n-1}$, where the superscript "*" denotes the transpose conjugate operator.
- Step 4) Determine the search length l_n according to Wolfe conditions [164] (Initialize m=0):
  - Step 4.1) Calculate $f(\overline{\varepsilon} + \gamma^m \overline{\rho}_n)$ and $g(\overline{\varepsilon} + \gamma^m \overline{\rho}_n)$.
  - Step 4.2) If $|g(\overline{\varepsilon} + \gamma^m \overline{\rho}_n)^T| \leq -\sigma \overline{g}_n^T \overline{\rho}_n$ and $f(\overline{\varepsilon}) - f(\overline{\varepsilon} + \gamma^m \overline{\rho}_n) \geq -\delta \gamma^m \overline{g}_n^T \overline{\rho}_n$, where σ and δ are two parameters adjusted in optimization and $0 < \delta < \sigma < 1$, let $l_n = \gamma^m$ and move to Step 5). Otherwise, let $l_n = \gamma^m$, $m = m + 1$, and go to Step 4.1).
- Step 5) Update $\overline{\varepsilon}_{n+1}$: $\overline{\varepsilon}_{n+1} = \overline{\varepsilon}_n + l_n \overline{\rho}_n$.
- Step 6) If termination condition is satisfied, stop iteration. Otherwise, let $n = n + 1$, and go to step 3).

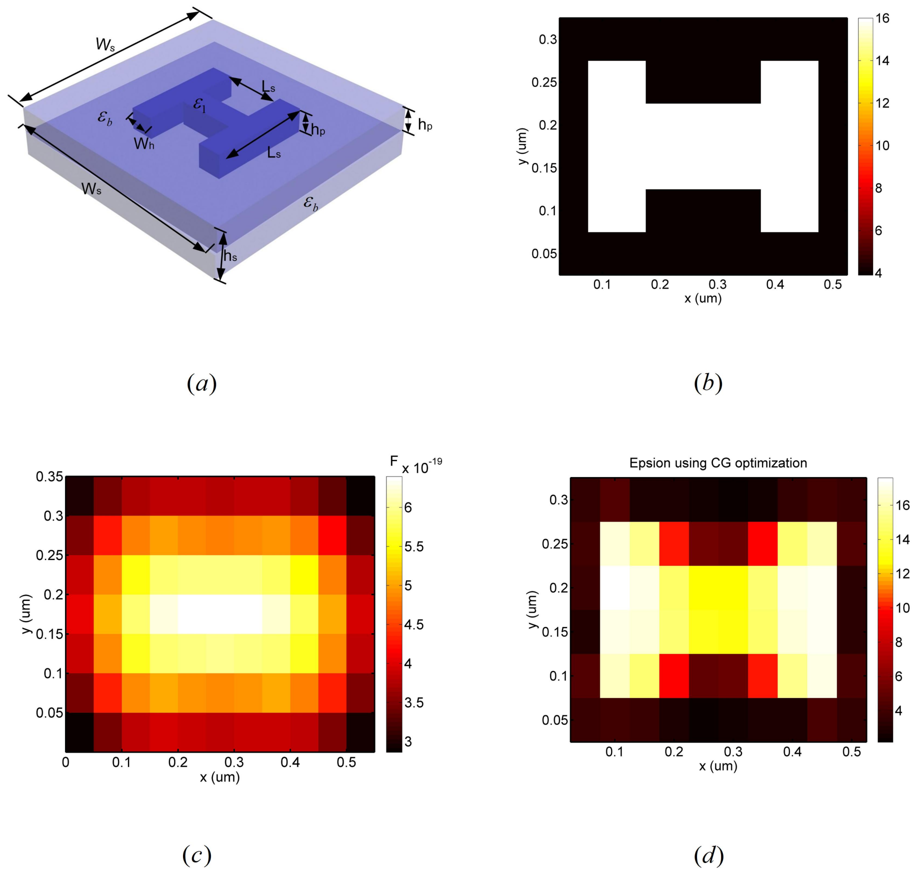

(*a*) (*b*)

(*c*) (*d*)

Fig. 4.1 (a) A three-dimensional sample with an "H" shape perturbation presented with $W_s = 6\ \mu m$, $h_s = 1\ \mu m$, $h_p = 0.4\ \mu m$, $W_h = 100\ nm$, $L_s = 400\ nm$, $\varepsilon_b = 3.9$ and $\varepsilon_1 = 16$; (b) Top view of exact distribution of relative permittivity in (a); (c) The simulated received capacitance signal; (d) Reconstruction of relative permittivity from the signal in (c).

4.4 Numerical validation

This section presents some numerical results to evaluate the performance of the proposed nonlinear reconstruction method in this chapter. In all the numerical results, as is illustrated in Fig. 3.1, a cone-sphere tip with $H = 0.5\ \mu m$, $h = 0.485\ \mu m$, and $\theta = 30°$ is used. The measured signals are computed by commercial software COMSOL, which include capacitance and capacitance derivative signals. Capacitance signal is same as the contrast capacitance in the forward model, and capacitance derivative signal is computed as the derivative of capacitance signal with respect to tip-sample distance. Both of them are widely used measured signals in NFMM measurements.

Figure 4.1(a) presents a three dimensional "H" shape perturbation presented sample. The total sample size is $W_s \times W_s \times h_s$ with $W_s = 6\ \mu m$ and $h_s = 1\ \mu m$. The "H" shape perturbation is distributed in a top layer layer of the sample with the thickness $h_p = 0.4\ \mu m$, width $W_h = 100\ nm$, and length $L_s = 400\ nm$. As illustrated in Fig. 4.1(a), except the "H" perturbation shape, all the other regions of the sample have a relative permittivity of $\varepsilon_b = 3.9$. The top view of exact distribution of permittivity is depicted in Fig. 4.1(b). Contrast capacitance computed by COMSOL software is shown in Fig. 4.1(c), where the "H" feature is hardly recognized although the position and size of the "H" shape are roughly displayed. As is mentioned above, the measured capacitance signal is not the exact sample properties beneath the tip, but an accumulative response over a spread region centered at the tip. Thus, by restoring the permittivity of the sample from the measured capacitance, imaging resolution can be improved. Figure 4.1(d) presents the reconstructed relative permittivity from the received capacitance signal in

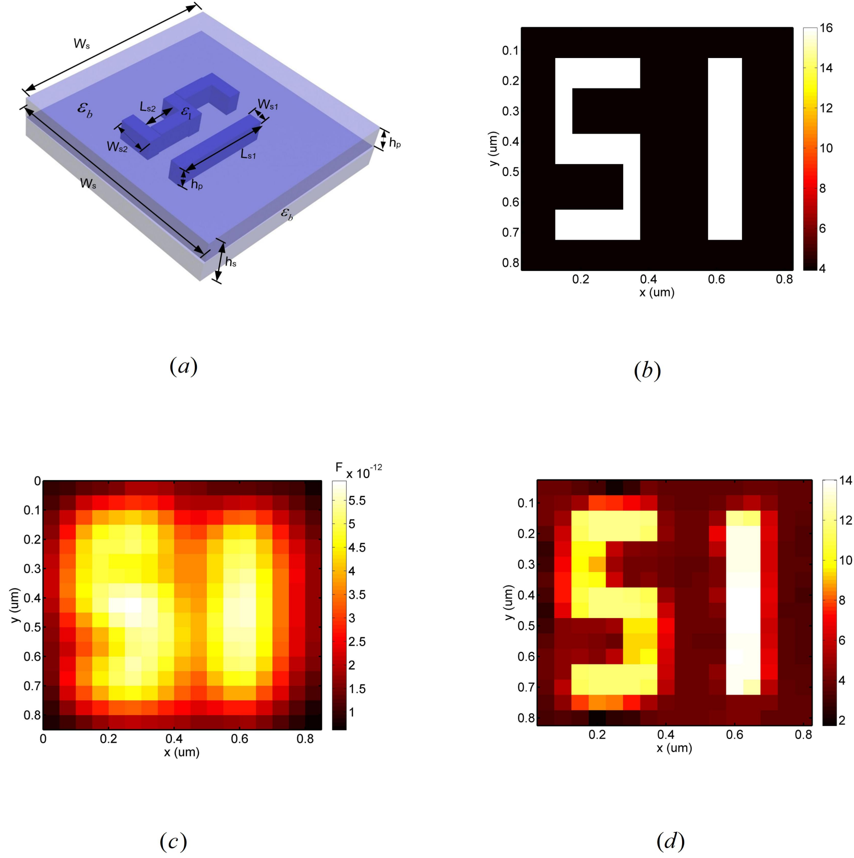

Fig. 4.2 (a) A three-dimensional sample with an "51" shape perturbation presented with $W_s = 6\ \mu m$, $h_s = 1\ \mu m$, $h_p = 0.4\ \mu m$, $W_{s1} = 100\ nm$, $W_{s2} = 250\ nm$, $L_{s1} = 600\ nm$, $L_{s2} = 150\ nm$, $\varepsilon_b = 3.9$, and $\varepsilon_1 = 16$; (b) Top view of exact distribution of relative permittivity in (a); (c) The simulated received capacitance derivative signal; (d) Reconstruction of relative permittivity from the signal in (c).

Fig. 4.1(c). It suggests that, by reconstructing the relative permittivity for all pixels, the "H" pattern is retrieved in Fig. 4.1(d), and imaging resolution is highly improved.

In the second example, a more challenging three dimensional sample is considered. The total size of the sample is the same as that of the first example, whereas the shape of perturbation is more complex. As illustrated in Fig. 4.2(a), a "51" shape perturbation is distributed in a top layer layer of the sample with the thickness $h_p = 0.4\ \mu m$, width $W_{s1} = 100\ nm$, $W_{s2} = 250\ nm$, and length $L_{s1} = 600\ nm$, $L_{s2} = 150\ nm$. Figure 4.2(b)

presents the top view of exact distribution of relative permittivity for "51" shape perturbation sample. The simulated received capacitance derivative signal is shown in Fig. 4.2(c), and it is found that the perturbation feature can hardly be identified from the received capacitance derivative signal. As presented in Fig. 4.2(d), the relative permittivity distribution is reconstructed from the received capacitance derivative signal. It suggests that the proposed nonlinear reconstruction method is able to reconstruct the sample properties from received signal and improve imaging resolution at the same time.

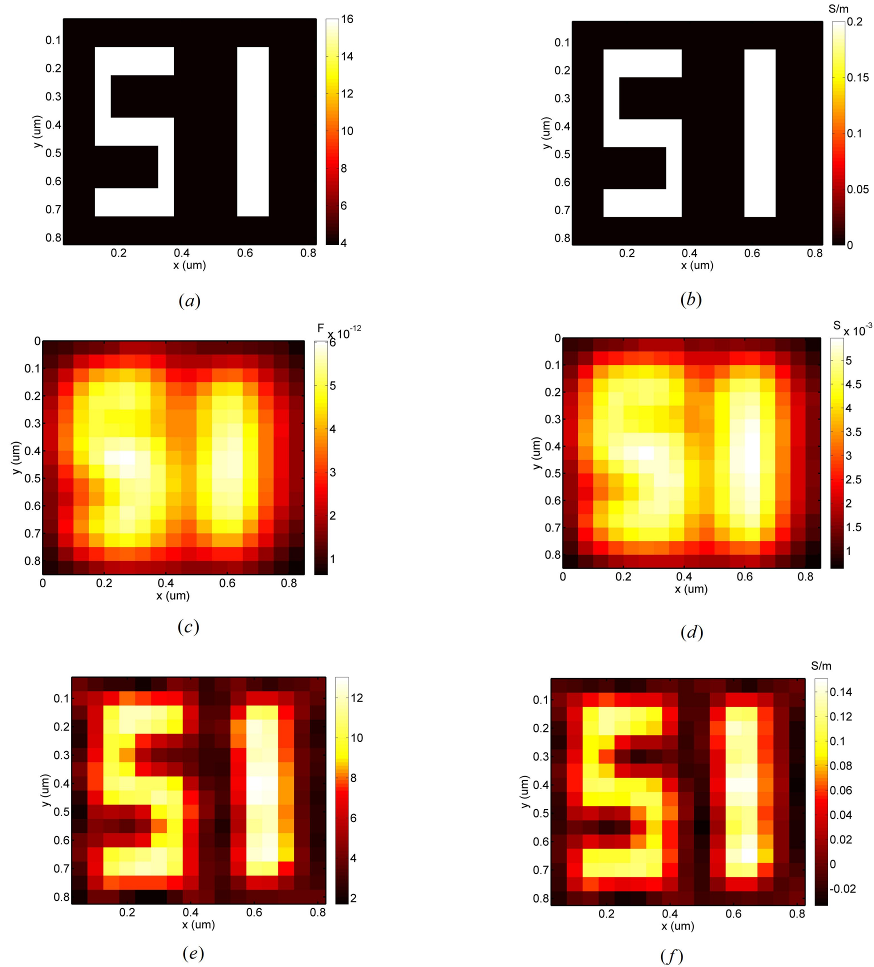

Fig. 4.3 Top view of exact distribution of (a) relative permittivity and (b) conductivity for a conductive sample with an "51" shape perturbation presented; The simulated received (c) capacitance derivative and (d) conductance derivative signals; Reconstructed (e) relative permittivity and (f) conductivity from the received signals.

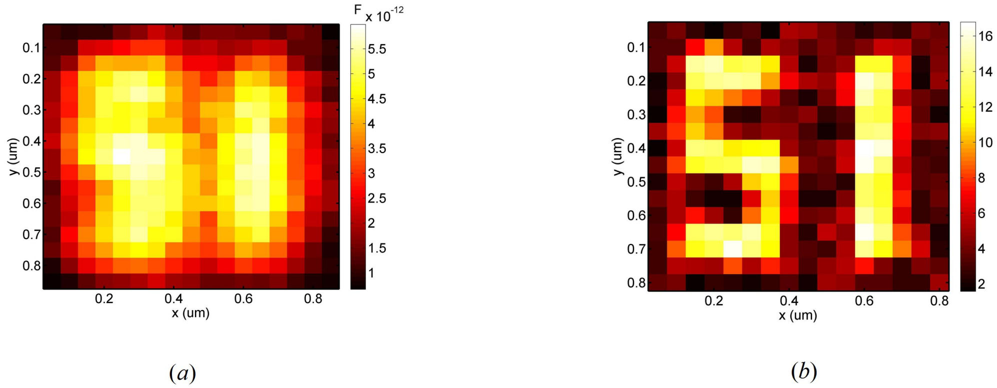

Fig. 4.4 (a) The simulated received capacitance derivative signal, where 5% Gaussian noise is added; (b) Reconstruction of relative permittivity from the signal in (a).

In the third example, a three dimensional sample with conductive perturbation presented is considered. The geometry size and position of the sample are the same as that of the second sample in Fig. 4.2(a), whereas the perturbation of "51" shape is replaced by conductive material with relative permittivity $\varepsilon_r = 16$ and conductivity $\sigma = 0.2\ S/m$. The top view of exact distribution of relative permittivity and conductivity for the sample are depicted in Fig. 4.3(a) and (b), respectively. The capacitance and conductance derivative signals are recorded by COMSOL software, and depicted in Fig. 4.3(c) and (d), respectively. Similarly, it is found that the perturbation feature can hardly be distinguished from the received capacitance and conductance derivative signals. In the inverse problem, both of relative permittivity and conductivity are reconstructed from the received signals. As shown in Fig. 4.3(e) and (f), the imaging resolution is highly improved and sample properties are restored.

The fourth example considers a noisy case, where the received signal in the second example is recorded as a matrix $\overline{\overline{R}}$. Additive white Gaussian noise (AWGN) is added to the received signal, and is quantified by $(||\overline{\overline{r}}||/||\overline{\overline{R}}||) \times 100\%$, where $||\cdot||$ denotes Frobenius norm. Figure 4.4(a) presents the received

capacitance signal with 5% Gaussian noise. The reconstructed permittivity profile from the received noisy signal is shown in Fig. 4.4(b), and it suggests that, with the presence of white Gaussian noise, the proposed method is able to reconstruct the properties of materials and improve the imaging resolution at the same time.

4.5 Summary

This chapter presents a nonlinear image reconstruction method with total variation constraint in near-field microwave microscopy (NFMM). The method is fast because it reduces the computational domain for tip-sample interaction problem to a block perturbation region by applying Green's Theorem in the forward model. In the inverse procedures, conjugate gradient (CG) method is used to minimize the objective function.

Numerical examples show that the proposed method can not only quantitatively reconstruct the permittivity distribution in three dimensional samples for NFMM, but also improve the imaging resolution. Most importantly, the methods proposed can be accomplished in a post-processing sense without requiring expensive and complex instruments in experiment or destructing the samples under test, and it can also be easily applied to other scanning imaging systems with very few changes.

In the next step, the experimental part of the inversion method will be focused to verify that the proposed method is able to improve resolution in experiment. It mainly includes the compensation of drift errors and noise, the calibration of various samples and the design of samples which can be hardly distinguished in experiment.

Chapter 5

Two FFT Subspace-Based Optimization Methods for Electrical Impedance Tomography

5.1 Introduction

In previous chapters, the modeling and inversion of NFMM have been discussed, which are in the framework of Laplace's equation that is described by Eq. (3.1). In this chapter, modeling and inversion of electrical impedance tomography (EIT), which are also in the framework of Laplace's equation, are studied. As mentioned in the first Chapter, electrical impedance tomography has attracted intense interests recently in both mathematical and engineering communities [120–122]. It is well-known that EIT is a very challenging problem due to its nonlinear and highly ill-posed properties [124, 125]. Various methods have been proposed to solve EIT problems

such as factorization method [131, 132], unconstrained least squares methods [133], variationally constrained numerical method [134], and subspace-based optimization method (SOM) [135].

The factorization method is able to locate the boundaries of inclusions fast, but it cannot be applied to some challenging inclusions, such as an annulus or two inclusions with one more conductive and the other one less conductive than the background [165–167]. In addition, the factorization method is not robust in presence of noise [168–170]. Traditionally, the unconstrained least squares approach has been the method of choice [133], due to its simplicity and relatively low computational cost. However, the unconstrained least squares approach does not make the best use of the measured data, and the image resolution is very limited [134]. Later, variational constraints method is proposed to achieve a better image resolution by efficiently using the data fit [134]. However, neither unconstrained least squares approach nor variational constraints method is robust to noise and reconstructed results are not satisfying when 3% noise is added in [134].

Recently, subspace-based optimization method (SOM) is proposed to solve electrical impedance tomography (EIT) problems [135]. In SOM, through a full singular value decomposition (SVD) of matrix mapping from induced current to voltage on the boundary, the induced current is decomposed into deterministic part and ambiguous part. The deterministic part can be computed from SVD, whereas the ambiguous part is obtained by optimizing the subspace spanned by singular vectors corresponding to small singular values. Compared with the contrast source inversion (CSI) method [171–173], SOM has the properties of faster convergence rate and good robustness against noise. However, a drawback of SOM is the overhead computation associated with the full SVD of matrix mapping from induced current to

voltage on the boundary [174]. In order to reduce the computational cost, an improved method is proposed in [175] to avoid the full SVD in SOM by using a thin SVD method. In addition, the computational speed is further increased with FFT applied in twofold subspace-based optimization method (TSOM) [176].

This chapter proposes two FFT subspace-based optimization methods for electrical impedance tomography in a domain with arbitrary boundary shape [123]. The first one is a new fast Fourier transform subspace-based optimization method (NFFT-SOM). Compared with the original SOM method in [135], the original contributions and advantages of NFFT-SOM are as follows:

(1) Instead of solving problems with circular boundary, where analytical Green's function is available, the proposed method extends to be applicable to a domain with an arbitrary boundary shape.

(2) Instead of using a noise subspace corresponding to smaller singular values in SOM, complete Fourier bases are used in NFFT-SOM. It is found that, compared with SOM, NFFT-SOM can obtain better reconstructed results in dealing with high noise EIT problem. Also, the computational complexity of the proposed method is greatly reduced compared with [135] for two reasons. Firstly, it avoids the full singular-value decomposition of the matrix mapping from the induced current to received voltage. Secondly, FFT can be directly used in algorithm to accelerate the computational speed.

(3) It is also found that NFFT-SOM is robust to the change of number of significant singular values (the integer L) for both high and low noise cases, which is an important and encouraging conclusion.

(4) Instead of using coupled dipole method to solve the EIT problem, a more general method, i.e., method of moment (MOM) is adopted in NFFT-SOM.

Additionally, compared with the thin SVD method in [175], where the computational costs is reduced in [175] by constructing the ambiguous current subspace from identity matrix and deterministic current subspace, the NFFT-SOM constructs the ambiguous current subspace that is directly spanned by complete Fourier bases instead of singular value vectors.

Compared with the twofold subspace-based optimization method in [176], where 2D Fourier bases are used to construct the current subspace for two dimensional TM cases, 1D Fourier bases are used in NFFT-SOM for EIT problems in proposed method. Since the subspace spanned by low frequency Fourier bases roughly corresponds to the subspace spanned by singular vectors with large singular values [176, 177], 1D Fourier bases adopted in this chapter directly exhibit such a correspondence, whereas the 2D Fourier bases adopted in [176] have to be sorted in order to exhibit such a correspondence. In addition, when the domain of interest is not a rectangle, the application of 2D Fourier bases requires an extra work of extending the domain of interest to a rectangle that is able to fully cover it. For NFFT-SOM, there is no need to extend the domain of interest to a rectangle one. These are two advantages of the proposed method over [176] as far as implementing the SOM is concerned.

As mentioned above, it is well known that the behavior of Fourier functions is similar to that of singular function in singular value decomposition (SVD) in the sense that low-frequency Fourier functions correspond to those singular functions with large singular values [176, 177]. Thus, it is very natural to think that we can replace the deterministic current and noise subspace in SOM with low frequency current and space spanned by

discrete Fourier bases, respectively. For convenience, we denote this method as low frequency subspace optimized method (LF-SOM). In this chapter, the performance of LF-SOM has been discussed through various numerical simulations and comparisons with traditional SOM and NFFT-SOM in EIT problems. Additionally, it is noted that though we test our proposed methods in two-dimensional examples in this chapter, both of the proposed methods are applicable to three-dimensional cases.

5.2 Forward model

5.2.1 Model description

In this chapter, a two-dimensional domain I consisting of a square and four half circles is considered. As it is depicted in Fig. 5.1, the square has a

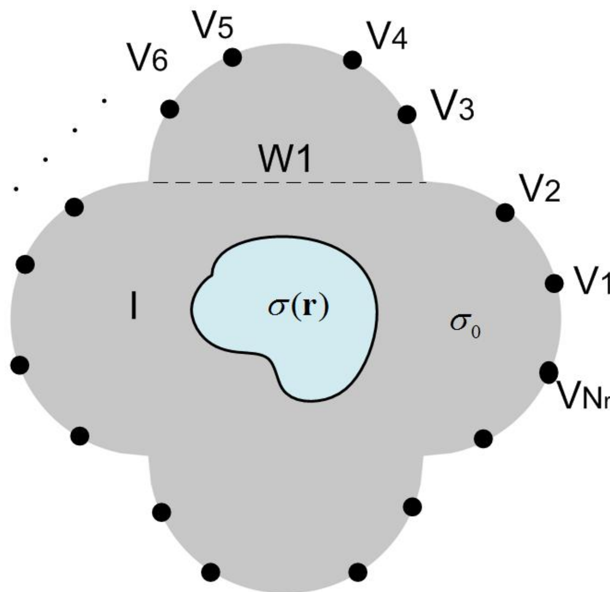

Fig. 5.1 A typical schematic of EIT problem with a two dimensional domain consisting of a square with width W_1 and four half circles with a radius of $W_1/2$, in which $W_1 = 1$, and $\sigma_0 = 1$. Voltages are measured at a number of N_r nodes on the boundary ∂I which are labeled as dots.

width of W_1 which is surrounded by four half circles with a radius of $W_1/2$. Actually, domain I can be of arbitrary shape, and the one in Fig. 5.1 is chosen as an example to present the proposed method. The background is homogenous material with the conductivity of σ_0 and some inclusions with conductivity of $\sigma(\mathbf{r})$ are embedded in a region interior to domain I. Electrical current is injected from the boundary ∂I into domain I, and voltages are measured at a number of N_r nodes on the boundary ∂I which are labeled as dots in Fig. 5.1. There are a total number of N_i excitations of current from boundary, and voltages at all nodes are measured for each excitation. Due to the presence of inclusions, the voltages measured at the boundary differ from those in homogenous case, and the differential voltage between these two cases at each node is recorded as V_p^q, p=1, 2, $\ldots$, N_i, q=1, 2, $\ldots$, N_r.

5.2.2 Theoretical principle

The Neumann boundary value problem in EIT can be described as the partial differential equation $\nabla\cdot(\sigma\nabla\mu) = 0$ in I, with $\sigma\frac{\partial\mu}{\partial\nu} = J$ on ∂I given a boundary excitation current $J \in H^{-1/2}(\partial I)$ with $\oint_{\partial I} Jds = 0$, where ν is the outer normal direction on the boundary ∂I. This Neumann boundary value problem has a unique weak solution given that $\mu \in H^1(I)$ with $\oint_{\partial I} \mu ds = 0$. The partial differential equation can further be written as:

$$\nabla\cdot(\sigma_0\nabla\mu) = -\rho_{in} \ in \ I, \qquad \sigma_0\frac{\partial\mu}{\partial\nu} = J \ on \ \partial I \tag{5.1}$$

with the induced source $\rho_{in} = \nabla\cdot[(\sigma-\sigma_0)\nabla\mu]$. Since the inclusions are within a region interior to I, the σ at the boundary ∂I is just the known σ_0. To solve Eq. (5.1) in method of moment [178], the Green's function $G(\mathbf{r},\mathbf{r}')$ in homogeneous background medium is defined and it satisfies the following

differential equation with the normalization $\oint_{\partial I} G(\mathbf{r},\mathbf{r}')ds = 0$,

$$\nabla \cdot (\sigma_0 \nabla G(\mathbf{r},\mathbf{r}')) = -\delta(\mathbf{r}-\mathbf{r}') \qquad \textit{with } \sigma_0 \frac{\partial G}{\partial \nu} = -\frac{1}{|\partial I|} \textit{ on } \partial I \tag{5.2}$$

where $\delta(\mathbf{r}-\mathbf{r}')$ is the Dirac delta function, and $\mathbf{r}$ and $\mathbf{r}'$ are the field point and source point in domain I, respectively.

The solution of every linear differential equation like Eq. (5.1) consists of two part: the particular solution μ^s that depends on the induced source ρ_{in} together with the boundary condition $\sigma_0 \frac{\partial \mu^s}{\partial \nu'} = 0$ on ∂I, and the general solution that depends on the exciting current J on the boundary that is injected into a homogeneous medium in absence of induced source ρ_{in}. The superscript s in μ^s means "scattered" since the physical meaning of μ^s is actually scattered potential by the induced source.

For the particular solution, it can be solved according to Green's theorem [140] as:

$$\mu^s = \int_I G(\mathbf{r},\mathbf{r}')\rho_{in}(\mathbf{r}')d\mathbf{r}' + I_{\partial I} \tag{5.3}$$

with

$$I_{\partial I} = \oint_{\partial I} [G(\mathbf{r},\mathbf{r}')\sigma_0 \frac{\partial \mu^s}{\partial \nu'} + \mu^s \sigma_0 \frac{G(\mathbf{r},\mathbf{r}')}{\partial \nu'}]ds' \tag{5.4}$$

On boundary ∂I, according to $\sigma_0 \frac{\partial \mu^s}{\partial \nu'} = 0$ and the predefined normalization $\oint_{\partial I} \mu^s ds = 0$, it is easy to get $I_{\partial I} = 0$. Therefore, $\mu^s = \int_I G(\mathbf{r},\mathbf{r}')\rho_{in}(\mathbf{r}')d\mathbf{r}'$ is the particular solution for differential equation in Eq. (5.1).

For the general solution, it satisfies that $\nabla \cdot (\sigma_0 \nabla \mu^0) = 0$ with $\sigma_0 \frac{\partial \mu^0}{\partial \nu'} = J \textit{ on } \partial I$. Thus, the compete solution for Eq. (5.1) is

$$\mu = \mu^0 + \mu^s = \mu^0 + \int_I G(\mathbf{r},\mathbf{r}')\nabla' \cdot [(\sigma(\mathbf{r}') - \sigma_0)\nabla' \mu(\mathbf{r}')]d\mathbf{r}' \tag{5.5}$$

Utilizing the identity $\nabla' \cdot (G(\mathbf{r},\mathbf{r}')\mathbf{A}) = \mathbf{A} \cdot \nabla' G(\mathbf{r},\mathbf{r}') + G(\mathbf{r},\mathbf{r}')\nabla' \cdot \mathbf{A}$ with $\mathbf{A} = (\sigma(\mathbf{r}') - \sigma_0)\nabla' \mu(\mathbf{r}')$ and considering that $\int_I \nabla' \cdot (G(\mathbf{r},\mathbf{r}')\mathbf{A})d\mathbf{r}' = 0$ due

to divergence theorem, Eq. (5.5) becomes

$$\mu = \mu^0 + \int_I -\nabla' G(\mathbf{r}, \mathbf{r}') \cdot (\sigma(\mathbf{r}') - \sigma_0) \nabla' \mu(\mathbf{r}') d\mathbf{r}' \tag{5.6}$$

Taking gradient on both side of Eq. (5.6), the following self-consistent equation can be obtained.

$$\mathbf{E}^t = \mathbf{E}^0 + \int_I -\nabla[\nabla' G(\mathbf{r}, \mathbf{r}') \cdot (\sigma(\mathbf{r}') - \sigma_0) \mathbf{E}^t(\mathbf{r}')] d\mathbf{r}' \tag{5.7}$$

for electric field $\mathbf{E}^t = -\nabla\mu$ and $\mathbf{E}^0 = -\nabla\mu^0$.

5.2.3 Discretization method

In method of moment (MOM) [178], domain I is discretized into a total number of M small squares that are centered at $\overline{r}_1, \overline{r}_1, \ldots, \overline{r}_M$, and the mth subunit has an effective radius of a_m. Pulse basis function and delta test function are used in MOM and the total electric field exerting on subunits $\overline{E}_p^t(\overline{r}_m)$ can be expressed as,

$$\overline{E}_p^t(\overline{r}_m) = \overline{E}_p^0(\overline{r}_m) + \sum_{n=1}^{M} \overline{\overline{G}}_D(\overline{r}_m, \overline{r}_n) \cdot \overline{\overline{\xi}}_n \cdot \overline{E}_p^t(\overline{r}_n) \tag{5.8}$$

where p represents the pth injection of current, and $\overline{E}_p^0(\overline{r}_m)$ is the electric field in homogeneous background. $\overline{\overline{\xi}}_n$ relates the current induced in the nth subunit $\overline{J}(\overline{r}_n)$ to the total electric field $\overline{E}_p^t(\overline{r}_n)$, i.e., $\overline{J}(\overline{r}_n) = \overline{\overline{\xi}}_n \cdot \overline{E}_p^t(\overline{r}_n)$. According to Eq. (5.6), $\overline{\overline{\xi}}_n$ can be calculated as $\overline{\overline{\xi}}_n = \pi a_m^2(\sigma(\overline{r}_n) - \sigma_0)\overline{\overline{I}}_2$, and $\overline{\overline{I}}_2$ is a two-dimensional identity matrix. The Green's function $\overline{\overline{G}}_D(\overline{r}_m, \overline{r}_n)$ is characterized as $\overline{\overline{G}}_D(\mathbf{r}, \mathbf{r}') \cdot \mathbf{d} = -\nabla[\nabla' G(\mathbf{r}, \mathbf{r}') \cdot \mathbf{d}]$ for a arbitrary dipole $\mathbf{d}$.

Since the boundary of domain I is irregular, $G(\mathbf{r}, \mathbf{r}')$ in Eq. (5.7) has no analytical solution. Instead, it can be computed using numerical software as potential at $\mathbf{r}$ due to a unit dipole placed at $\mathbf{r}'$. In order to deal with singularities in the integral, $G(\mathbf{r}, \mathbf{r}')$ is decomposed into two parts: unbounded-domain Green's function $G_0(\mathbf{r}, \mathbf{r}')$ that contains singularity, and

the general Green's function $G_I(\mathbf{r},\mathbf{r}')$ that contains no singularity and is directly calculated as $G(\mathbf{r},\mathbf{r}')-G_0(\mathbf{r},\mathbf{r}')$. Then, in Eq. (5.7), the singularities in the integral can be easily calculated with the analytical solution, and the other part of integral is calculated by Gaussian quadrature method [179]. The details to deal with singularities are included in next section.

The relationship between $\overline{J}(\overline{r}_n)$ and $\overline{E}^t_p(\overline{r}_n)$, together with Eq. (5.8) leads to

$$\overline{J}_p = \overline{\overline{\xi}} \cdot (\overline{E}^0_p + \overline{\overline{G}}_D \cdot \overline{J}_p) \tag{5.9}$$

where $\overline{J}_p$ is a $2M$-dimensional vector with

$$\overline{J}_p = [J^x_p(\overline{r}_1), J^x_p(\overline{r}_2), ..., J^x_p(\overline{r}_M), J^y_p(\overline{r}_1), J^y_p(\overline{r}_2), ..., J^y_p(\overline{r}_M)]^T \tag{5.10}$$

in which $J^x_p(\overline{r}_M)$ and $J^y_p(\overline{r}_M)$ are x and y component of induced current at $\overline{r}_M$ for the pth injection of current on boundary ∂I, respectively. The superscript T denotes the transpose operator of a matrix. $\overline{\overline{G}}_D$ is a $2M \times 2M$ matrix with

$$\overline{\overline{G}}_D = [\overline{\overline{G}}_{xx}, \overline{\overline{G}}_{xy}; \overline{\overline{G}}_{yx}, \overline{\overline{G}}_{yy}] \tag{5.11}$$

in which $\overline{\overline{G}}_{xx}$ is a $M \times M$ matrix. $\overline{\overline{G}}_{xx}(m,n)$ and $\overline{\overline{G}}_{xy}(m,n)$ is computed as x component of electric field at $\overline{r}_m$ due to a unit x-oriented and y-oriented dipole placed at $\overline{r}_n$, respectively. $\overline{\overline{G}}_{yx}$ and $\overline{\overline{G}}_{yy}$ can also be evaluated in a similar way. $\overline{\overline{\xi}}$ consists of ξ_m in a diagonal way, and ξ_m can be calculated as $\xi_m = \pi a^2_m(\sigma(\overline{r}_n) - \sigma_0)$. Thus, the induced current $\overline{J}_p$ can be obtained from Eq. (5.9). According to Eq. (5.6), the differential voltage on the boundary $V(\mathbf{r}_{\partial\mathbf{I}})$ can be calculated as:

$$V(\mathbf{r}_{\partial\mathbf{I}}) = \mu - \mu^0 = \int_I -\nabla' G(\mathbf{r}_{\partial\mathbf{I}}, \mathbf{r}') \cdot (\sigma(\mathbf{r}') - \sigma_0)\nabla'\mu(\mathbf{r}')d\mathbf{r}' \tag{5.12}$$

where $\mathbf{r}_{\partial\mathbf{I}}$ is the position at the boundary ∂I. Following the same discretized method in Eq. (5.8), the differential voltage $\overline{V}_p$ at the boundary for pth

injection is then calculated as

$$\overline{V}_p = \overline{\overline{G}}_\partial \cdot \overline{J}_p \tag{5.13}$$

where $\overline{\overline{G}}_\partial(\mathbf{r}_{\partial\mathbf{I}}, \mathbf{r}')$ is characterized as $\overline{\overline{G}}_\partial(\mathbf{r}_{\partial\mathbf{I}}, \mathbf{r}') = \nabla' G(\mathbf{r}_{\partial\mathbf{I}}, \mathbf{r}')$ and $\overline{\overline{G}}_\partial$ is a $N_r \times 2M$ matrix $[\overline{\overline{G}}^x_\partial, \overline{\overline{G}}^y_\partial]$. $\overline{\overline{G}}^x_\partial(q,n)$ and $\overline{\overline{G}}^y_\partial(q,n)$ are calculated as potential on the boundary node $\overline{r}_q$ due to a unit x-oriented and y-oriented dipole at $\overline{r}_n$, respectively. This forward model has been verified by comparing with commercial software (COMSOL), and numerical results calculated by the proposed forward model agree well with the simulation results produced by COMSOL for various examples.

5.2.4 Singularities in Green's function

As is mentioned in previous section, to deal with the singularities in the integral of Eq. (5.7), $G(\mathbf{r}, \mathbf{r}')$ is decomposed into two parts: unbounded-domain Green's function $G_0(\mathbf{r}, \mathbf{r}')$

$$G_0(\mathbf{r}, \mathbf{r}') = \frac{-1}{2\pi\sigma_0} \log(|\mathbf{r} - \mathbf{r}'|) \tag{5.14}$$

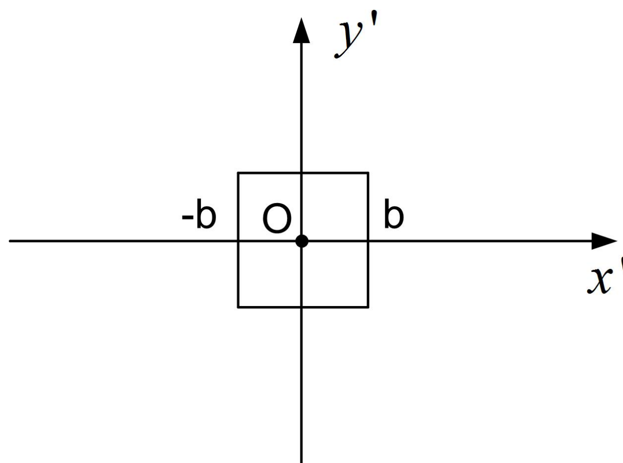

Fig. 5.2 Schematic of Green's function integral on a small cell with singularities.

which contains singularity and the general Green's function $G_I(\mathbf{r}, \mathbf{r}')$ that contains no singularity and is directly calculated as $G(\mathbf{r}, \mathbf{r}') - G_0(\mathbf{r}, \mathbf{r}')$. The second part is directly calculated by Gaussian quadrature method [179], and for the first part, it is calculated as follows. As depicted in Fig. 5.2, for arbitrary small discretization cell D with the size of $2b \times 2b$, one needs to calculate the following integration in Eq. (5.7) (Suppose that the filed point is at the origin):

$$\mathbf{I_1} = \iint_D -\nabla[\nabla' G(\mathbf{r}, \mathbf{r}') \cdot \mathbf{d_0}]\ dx'dy' \tag{5.15}$$

in which $\mathbf{d}_0$ is a unit dipole. I_{xx} and I_{xy} are defined as the x component of $\mathbf{I_1}$ due to a unit x and y oriented dipole, respectively. Similarly, I_{yx} and I_{yy} are defined as y component of $\mathbf{I_1}$ due to a unit x and y oriented dipole, respectively. Thus,

$$I_{xx} = -\int_{-b}^{b} \frac{\partial}{\partial x} \int_{-b}^{b} [\nabla' G(\mathbf{r}, \mathbf{r}') \cdot (\widehat{x})]\ dx'dy' = -1/2 \tag{5.16}$$

I_{yy}, I_{xy} and I_{yx} are calculated as -1/2, 0, 0 in a similar way, respectively.

5.3 Inverse algorithm

5.3.1 Subspace-based optimization method (SOM)

It is well-known that EIT is a highly ill-posed problem, which means that the induced current can't be uniquely determined from Eq. (5.14). In the traditional SOM [174, 180], a full singular value decomposition is firstly conducted on $\overline{\overline{G}}_\partial$, in which $\overline{\overline{G}}_\partial = \sum_m \overline{u}_m \sigma_m \overline{\nu}_m^*$ with $\overline{\overline{G}}_\partial \cdot \overline{\nu}_m = \sigma_m \overline{u}_m$, $\sigma_1 \geq \sigma_2 \ldots \geq \sigma_{2M} > 0$. Alternatively, $\overline{\overline{G}}_\partial = \overline{\overline{U}} \cdot \overline{\overline{\Sigma}} \cdot \overline{\overline{V}}^*$, in which $\overline{\overline{U}}$ is a $N_r \times N_r$ matrix composed of left singular vectors, $\overline{\overline{V}}$ is a $2M \times 2M$ matrix composed of right singular vectors, and $\overline{\overline{\Sigma}}$ is a diagonal matrix composed of

singular values. The superscript $*$ denotes the transpose conjugate operator.

Then, induced current $\overline{J}$ is mathematically classified into deterministic current $\overline{J}^s$ and ambiguous current $\overline{J}^n$, $\overline{J} = \overline{J}^s + \overline{J}^n$, where the former is uniquely determined by the signal subspace $\overline{\overline{V}}^s$ composed of first L singular vectors and the latter is reconstructed in the noise subspace $\overline{\overline{V}}^n$ spanned by the remaining $2M - L$ singular value vectors [174, 180].

5.3.2 New fast Fourier transform subspace-based optimization method (NFFT-SOM)

As mentioned in [175, 176], the drawback of the traditional SOM is its overhead computational cost associated with a full SVD of the matrix mapping from the induced current to received signal, especially when the domain of interest is large. Thus, an alternative method to construct ambiguous part of induced current is proposed to avoid a full SVD of the matrix mapping from induced current to scattered fields [175].

This chapter proposes a new fast Fourier transform subspace-based optimization method (NFFT-SOM) which avoids a full SVD of $\overline{\overline{G}}_\partial$, and in addition, fast Fourier transform can be used to accelerate the computational speed at the same time. In NFFT-SOM, the deterministic current is still computed by the first L singular vectors, whereas the ambiguous current is spanned by a complete Fourier bases $\overline{\overline{F}}$, in which the $2M \times 2M$ dimensional matrix $\overline{\overline{F}}$ consists of units $\overline{\overline{F}}(m, n) = \exp(-j2\pi(m-1)(n-1)/(2M))$. Since only the first L singular vectors is needed, a thin-type SVD of $\overline{\overline{G}}_\partial$ is sufficient to supply these bases, and the complexity of a thin SVD is smaller than that of a full SVD [175, 181]. Thus, the induced current can be written in the

form

$$\overline{J}_p = \overline{J}_p^s + \overline{\overline{F}} \cdot \overline{\alpha}_p^n \tag{5.17}$$

where $\overline{\alpha}_p{}^n$ is a $2M$-dimensional vector to be optimized. $\overline{\overline{F}} \cdot \overline{\alpha}_p{}^n$ is calculated in fast Fourier transform way with the computational complexity of $O(2M\log_2 2M)$, whereas the complexity of direct multiplication in traditional SOM is $O(2M(2M-L))$. Since $2M-L$ is usually much larger than $\log_2 2M$, the computational cost in NFFT-SOM is much smaller. Using Eq. (5.17), the residue of Eq. (5.14) is

$$\Delta_p^f = ||\overline{\overline{G}}_\partial \cdot \overline{J}_p^s + \overline{\overline{G}}_\partial \cdot \overline{\overline{F}} \cdot \overline{\alpha}_p^n - \overline{V}_p||^2 \tag{5.18}$$

and residue of Eq. (5.9) becomes

$$\Delta_p^a = ||\overline{\overline{A}} \cdot \overline{\alpha}_p^n - \overline{B}_p||^2 \tag{5.19}$$

in which $\overline{\overline{A}} = \overline{\overline{F}} - \overline{\overline{\xi}} \cdot (\overline{\overline{G}}_D \cdot \overline{\overline{F}})$, and $\overline{\overline{B}}_p = \overline{\overline{\xi}} \cdot (\overline{E}^0 + \overline{\overline{G}}_D \cdot \overline{J}_p^s) - \overline{J}_p^s$. The objective function is defined as:

$$f(\overline{\alpha}_1^n, \overline{\alpha}_2^n, ..., \overline{\alpha}_{N_i}^n, \overline{\overline{\xi}}) = \sum_{p=1}^{N_i} (\Delta_p^f / |\overline{V}_p|^2 + \Delta_p^s / |\overline{J}_p^s|^2) \tag{5.20}$$

5.3.3 Low frequency subspace optimization method (LF-SOM)

Considering the fact that low-frequency Fourier functions in FFT correspond to those singular functions with large singular values in SVD [176, 177], one can further replace the deterministic current $\overline{J}^s$ in NFFT-SOM with low frequency components of current in this section, and denote the method as low frequency subspace optimization method (LF-SOM). In LF-SOM, the deterministic current $\widetilde{J}_p^L$ is spanned by the first L low frequency Fourier bases, i.e., $\widetilde{J}_p^L = \sum_{i=1}^{L} \alpha_i' F_i = \overline{\overline{F}}_L \alpha_p'^L$, and the coefficient $\alpha_p'^L$ can be calculated in a least

square sense from Eq. (5.14) by

$$\alpha_p'^L = ((\overline{\overline{G}}_\partial \overline{\overline{F}}_L)^* \cdot (\overline{\overline{G}}_\partial \overline{\overline{F}}_L))^{-1} \cdot ((\overline{\overline{G}}_\partial \overline{\overline{F}}_L)^* \cdot \overline{V}_p) \tag{5.21}$$

The computational complexity of Eq. (5.21) is $O(2MN_rL)$, which is smaller than the computational complexity ($O(2MN_r{}^2)$) of thin SVD [175, 181] in NFFT-SOM since L is usually smaller than N_r. Thus, the speed of LF-SOM is faster compared with NFFT-SOM.

Therefore, induced current $\overline{J}_p$ can be spanned by Fourier bases as

$$\overline{J}_p = \sum_{i=1}^{L} \alpha_i' F_i + \sum_{i=1}^{L} (\alpha_i - \alpha_i') F_i + \sum_{i=L+1}^{2M} \alpha_i F_i = \widetilde{J}_p^L + \overline{\overline{F}} \cdot \overline{\beta}_p^n \tag{5.22}$$

Where $\overline{\beta}_p{}^n$ is a $2M$-dimensional vector to be reconstructed. For LF-SOM, the objective function and following steps are the same as that of NFFT-SOM except that induced current is expressed in a different way as it is in Eq. (5.22).

5.3.4 Implementation procedures

The optimization method used in the contrast source inversion method is adopted, i.e., alternatively updating the coefficients $\overline{\alpha}_p{}^n$ and the polarization tensor $\overline{\overline{\xi}}$. The implementation procedures of NFFT-SOM and LF-SOM are as follows [174, 176, 182]:

- Step 1) Calculate $\overline{\overline{G}}_\partial$, $\overline{\overline{G}}_D$. For NFFT-SOM, compute the thin SVD of $\overline{\overline{G}}_\partial$, and obtain $\overline{J}_p^s$ in Eq. (5.17). For LF-SOM, compute $\alpha_p'^L$ in Eq. (5.21), and obtain $\widetilde{J}_p^L$.

- Step 2) Initial step, $n = 0$; Give an initial guess of $\overline{\overline{\xi}}$ according to back propagation [171], and initialize $\overline{\alpha}_{p,0}^n = 0$, $\overline{\rho}_{p,0} = 0$.

- Step 3) n=n+1.

– Step 3.1) Update $\overline{\alpha}^n_{p,n}$: calculate gradient $\overline{g}_{p,n} = \nabla_{\overline{\alpha}^n_p} f$ evaluate at $\overline{\alpha}^n_{p,n-1}$ and $\overline{\overline{\xi}}_{n-1}$. Then determine the Polak-Ribière-Polyak (PRP) directions [164]: $\overline{\rho}_{p,n} = -\overline{g}_{p,n} + (\mathrm{Re}[(\overline{g}_{p,n} - \overline{g}_{p,n-1})^* \cdot \overline{g}_{p,n}]/||\overline{g}_{n-1}||^2)\overline{\rho}_{p,n-1}$. Update $\overline{\alpha}^n_{p,n}$ as: $\overline{\alpha}^n_{p,n} = \overline{\alpha}^n_{p,n-1} + d_{p,n}\overline{\rho}_{p,n}$. $d_{p,n}$ is the search length, and the objective function is quadratic in terms of parameter $d_{p,n}$. $d_{p,n}$ can be easily obtained as done in [171, 182].

– Step 3.2) Update $\overline{\overline{\xi}}_n$: For the mth subunit, $m = 1,\ 2,\ \ldots,\ M$, calculate the induced current $(\overline{J}_{p,n})_m$ and the total electric filed $(\overline{E}^t_{p,n})_m$. Then objective function becomes quadratic in terms of $(\overline{\overline{\xi}}_n)_m$, and the solution is given by [174]:

$$(\overline{\overline{\xi}})_m = [\sum_{p=1}^{N_i} \frac{(\overline{E}^t_{p,n})^*_m}{||\overline{J}^s_p||} \cdot \frac{(\overline{J}_{p,n})_m}{||\overline{J}^s_p||}]/[\sum_{p=1}^{N_i} \frac{(\overline{E}^t_{p,n})^*_m}{||\overline{J}^s_p||} \cdot \frac{(\overline{E}^t_{p,n})_m}{||\overline{J}^s_p||}] \quad (5.23)$$

- Step 4) If the termination condition is satisfied, stop iteration. Otherwise, go to step 3).

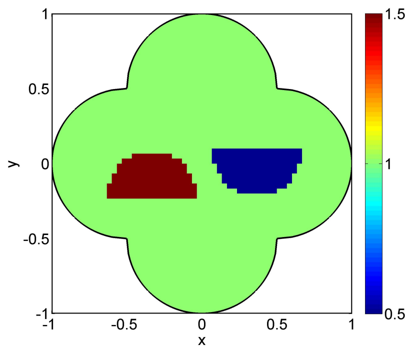

(a)

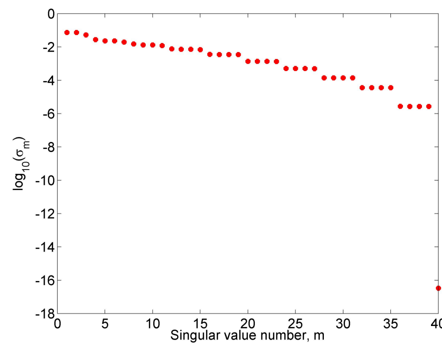

(b)

Fig. 5.3 (a)The exact profile of two half circles: radii of both half circles are 0.3, and centers are located at (-0.35, -0.2) and (0.35, 0.1), respectively. (b) The singular values of the operator $\overline{\overline{G}}_\partial$, where the base 10 logarithm of the singular value is plotted.

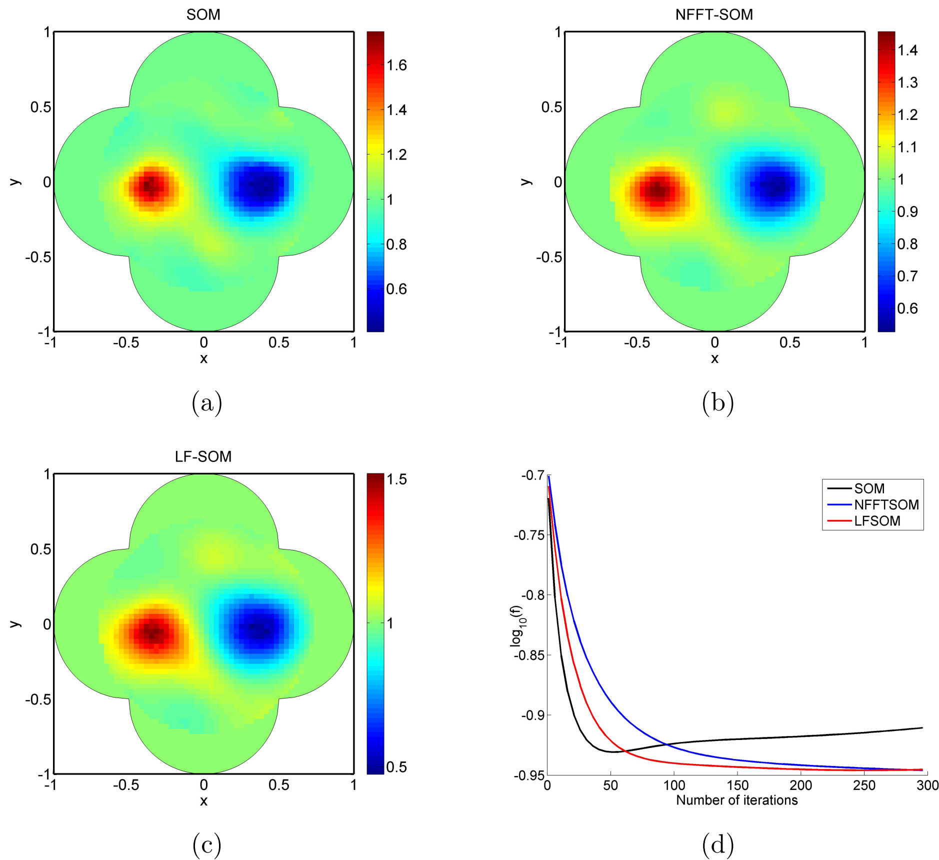

Fig. 5.4 Reconstructed conductivity profiles at the 60th iterations with $L = 4$ for (a) traditional SOM (b) NFFT-SOM and (c) LF-SOM, where 20% Gaussian noise is added. (d) Comparison of exact error f in the first 300 iterations for the three inversion methods with $L = 4$, where the base 10 logarithm of the exact error value is plotted.

5.4 Numerical simulation and discussions

In this section, numerical examples for both high and low noise cases are considered to verify the proposed methods, and compare the performance of tradition SOM, NFFT-SOM and LF-SOM. As shown in Fig. 5.3(a), the "two half circles" profile is considered in numerical simulations. Although all numerical results reported in this section are for the "two half circles" profile, the proposed algorithms have been tested on various other profiles, and all drawn conclusions are the same as the one reported in this section.

In these examples, a total number of $N_i = 10$ current excitations is placed at the boundary ∂I, where $J_{2t-1}(\phi) = \cos(t\phi)$, and $J_{2t}(\phi) = \sin(t\phi)$, t=1, 2, ..., 5, and $0 \leq \phi \leq 2\pi$. A total number of $N_r = 40$ measurements is conducted on the boundary of ∂I. *A priori* information is known that inclusions are within a circle of radius $\sqrt{2}/2W_1$ centered at the origin with $W_1 = 1$, which is referred to as the domain of interest. In discretization, the domain of interest is divided into 1421 subunits with dimensions 0.033×0.033. The measured voltage is computed by commercial software COMSOL to avoid inverse crime, and recorded as a matrix $\overline{\overline{R}}$ with the size of $N_r \cdot N_i$. In this examples, additive white Gaussian noise (AWGN) is added to the measured voltages, and is quantified by $(||\overline{\overline{r}}||/||\overline{\overline{R}}||)\times 100\%$, where $||\cdot||$ denotes Frobenius norm.

The value of L is important in implementing SOM and the proposed algorithms. In previous literatures [174, 176, 180], L is usually determined from singular values of the operator $\overline{\overline{G}}_\partial$, and a good candidate of L takes the value where singular values noticeably change the slope in the spectrum [174]. In EIT, as is depicted in Fig. 5.3(b), it is difficult to find a good candidate of L directly from the spectrum of $\overline{\overline{G}}_\partial$. Thus, it is preferred that there is a consecutive range of integer L, instead of a single value, that can be chosen for various cases.

With the presence of 20% white Gaussian noise, the reconstructed conductivity profiles at 60th iteration for SOM, NFFT-SOM, and LF-SOM are presented in Fig. 5.4(a), 5.4(b), and 5.4(c), respectively. It is found that the reconstruction results are quite satisfying for all the three methods when $L = 4$. If the same computer is used, for 60 iterations, it takes about 63 seconds to finish the optimization for SOM whereas it takes only about 15 and 14 seconds for NFFT-SOM and LFSOM, respectively. It suggests that

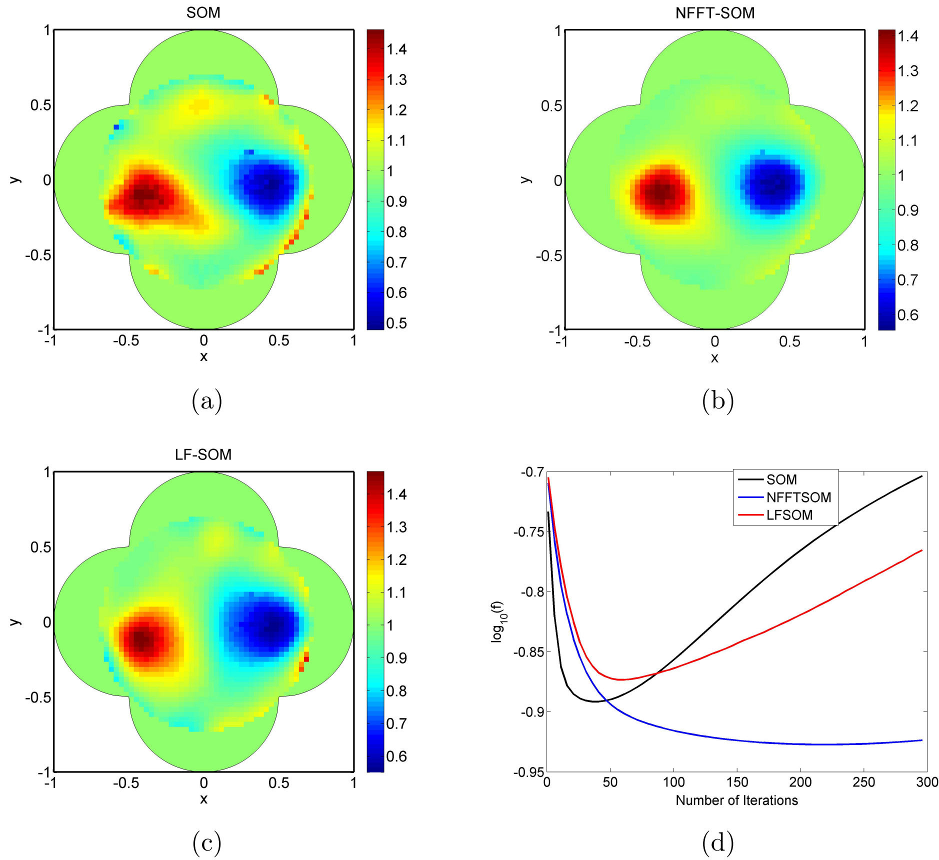

Fig. 5.5 Reconstructed conductivity profiles at the 60th iterations with $L = 12$ for (a) traditional SOM (b) NFFT-SOM and (c) LF-SOM, where 20% Gaussian noise is added. (d) Comparison of exact error f in the first 300 iterations for the three inversion methods with $L = 12$, where the base 10 logarithm of the exact error value is plotted.

compared with traditional SOM, the proposed methods has great advantage in the speed. To further compare the three methods quantitatively, exact error f is defined as $|A_\sigma - B_\sigma|/|B_\sigma|$, where A_σ and B_σ are reconstructed conductivity and exact conductivity of the profile, respectively. Figure 5.4(d) presents the comparison of exact error with the base of 10 logarithm in the first 300 iterations for the three inversion methods. It is found that, compared with SOM, both LF-SOM and NFFT-SOM can get a smaller exact error for high noise cases, but with more iterations.

It is worthwhile to discuss the reasons of the results in Fig. 5.4(d). In

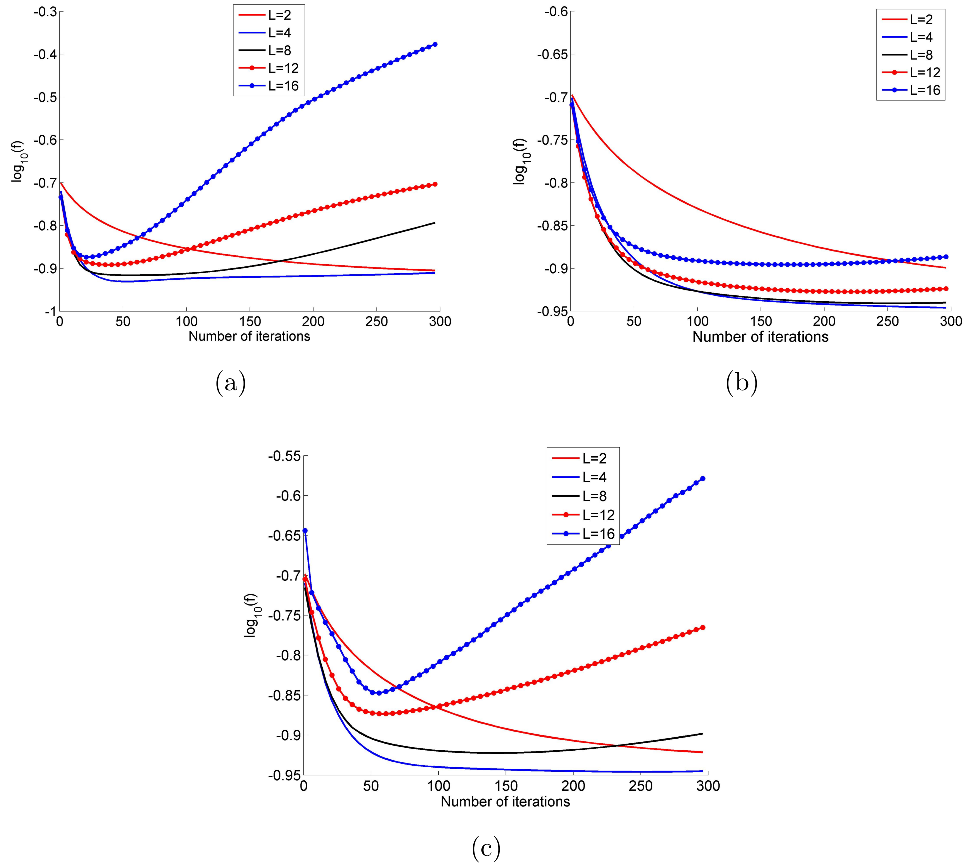

Fig. 5.6 Comparison of exact error f in the first 300 iterations for (a) traditional SOM (b) NFFT-SOM and (c) LF-SOM with 20% Gaussian noise, where the base 10 logarithm of the exact error value is plotted.

SOM, the deterministic current is calculated from the spectrum analysis of (5.14) without using any optimizations, and ambiguous current is determined by optimizing a noise subspace which is perpendicular to the deterministic current space. Since the voltages measured at the boundary $\overline{V}_p$ contain white Gaussian noise, the calculated deterministic current differs from the exact one. When the noise level is high, the deterministic current becomes inaccurate and needs to be optimized as well. In the proposed NFFT-SOM and LF-SOM, the space to be optimized is no longer perpendicular to the deterministic current space, and instead the space spanned by complete Fourier bases is used. In the optimization, the deterministic current of NFFT-SOM and LF-

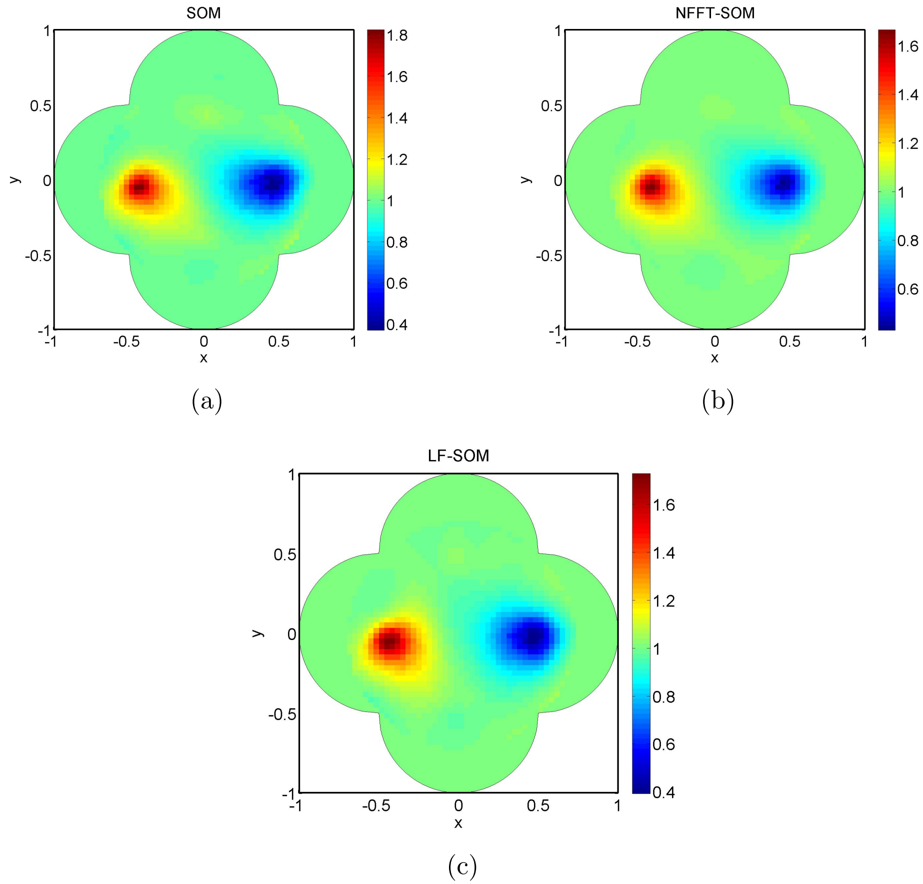

Fig. 5.7 Reconstructed conductivity profiles at the 60th iterations with $L = 12$ for (a) traditional SOM (b) NFFT-SOM and (c) LF-SOM, where 1% Gaussian noise is added.

SOM is further optimized based on an initial value calculated from Eq. (5.14). Therefore, compared with SOM, both LF-SOM and NFFT-SOM can get a smaller exact error for high noise cases, but with more iterations.

To study the effects of L on the three inversion methods, with $L = 12$, the reconstructed conductivity profiles at 60th iteration for SOM, NFFT-SOM, and LF-SOM are presented in Fig. 5.5(a), 5.5(b), and 5.5(c), respectively. It is noted that the reconstructed profile for NFFT-SOM outperforms those for the traditional SOM and LF-SOM. Figure 5.5(d) shows the exact error with the base of 10 logarithm for the three inversion methods, and it suggests that SOM and LF-SOM can hardly converges to a satisfying exact error with

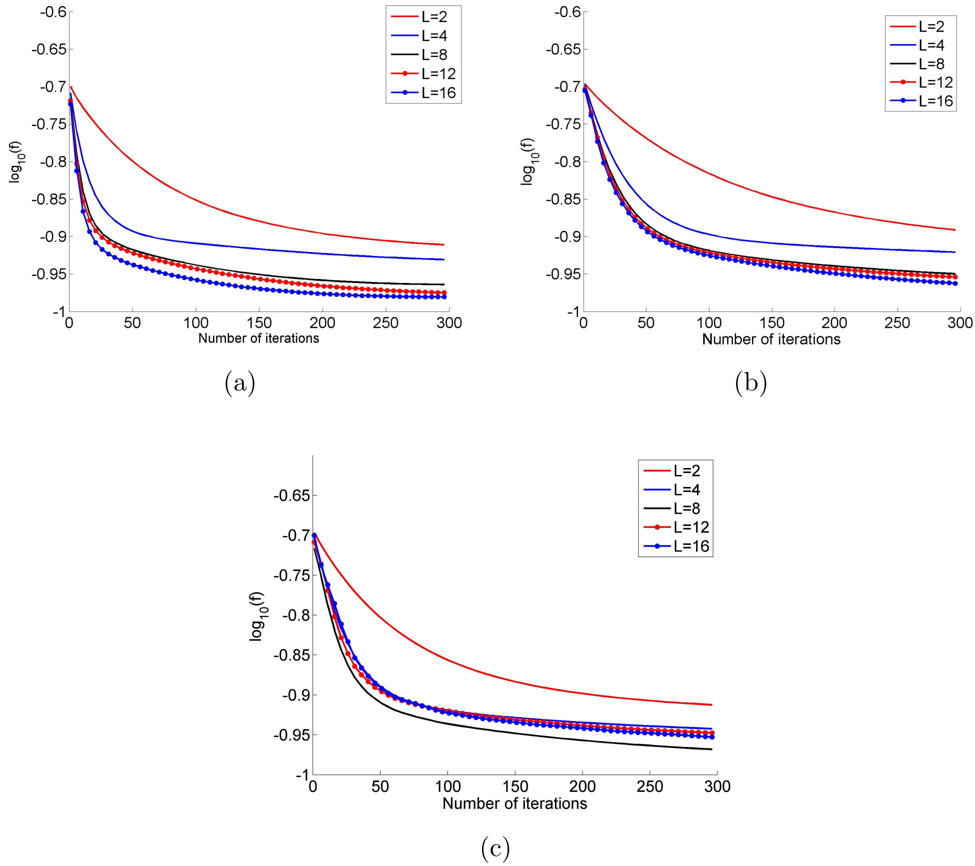

Fig. 5.8 Comparison of exact error f in the first 300 iterations for (a) traditional SOM (b) NFFT-SOM and (c) LF-SOM with 1% Gaussian noise, where the base 10 logarithm of the exact error value is plotted.

$L = 12$. The exact error of SOM, NFFT-SOM, and LF-SOM varying with number of iterations for different values of L are further plotted in Fig. 5.6(a), 5.6(b), and 5.6(c), respectively. It suggests that NFFT-SOM is robust to L variations, and a good reconstructed results can be obtained by NFFT-SOM for $4 \leq L \leq 12$. In comparison, the effects of L on LF-SOM and SOM are dramatic, which makes it difficult to choose an appropriate L in practice.

The effects of L on the three methods are also considered under low noise cases. With the presence of 1% white Gaussian noise, the reconstructed conductivity profiles at 60th iteration for SOM, NFFT-SOM, and LF-SOM with $L = 12$ are presented in Fig. 5.7(a), 5.7(b), and 5.7(c), respectively. It

suggests that, unlike the high noise cases, the reconstruction results are quite satisfying for all the methods with $L = 12$. The exact error curves of SOM, NFFT-SOM, and LF-SOM for different values of L are also plotted in Fig. 5.8(a), 5.8(b), and 5.8(c), respectively, where 1% noise is added. It is found that, compared with the high noise cases, the effects of L on all the three methods are much smaller, and a good reconstructed result can be obtained with $4 \leq L \leq 12$ for all the inversion methods.

5.5 Summary

This chapter proposes two fast Fourier transform subspace-based optimization methods (NFF-SOM and LF-SOM) to solve the EIT problem with arbitrary boundary. Through numerical simulations and analysis, it suggests that NFF-SOM and LF-SOM have two advantages over traditional SOM. Firstly, the speed of the proposed methods is much faster than that of traditional SOM since the computational complexity is largely reduced by implementing FFT in the optimization procedures. In NFFT-SOM, the computational speed is also accelerated by avoiding the full singular-value decomposition of the matrix mapping from the induced current to received voltage. In LF-SOM, the computational cost is further reduced by replacing the singular value decomposition with a lower computational cost least square method. Secondly, compared with SOM, both LF-SOM and NFFT-SOM can get a smaller exact error for high noise cases, which means that a better reconstructed result can be obtained for the proposed methods.

Most importantly, besides the above mentioned two advantages, it is found that NFFT-SOM has another advantage that it is robust to the L variations. For NFFT-SOM, there is a consecutive range of integer L, instead of a single

value, that can be chosen in practice for both high and low noise cases. This is an important and encouraging advantage, especially for EIT where it is difficult to directly find a good candidate of L from the spectrum of $\overline{\overline{G}}_\partial$.

Additionally, further numerical simulations also suggest that the drawback of the proposed methods is that, compared with traditional SOM, both of the proposed methods need more iterations in optimization since the noise spaces of them are spanned by complete Fourier bases.

Chapter 6

Conclusions and Future Work

6.1 Conclusions

This thesis addresses the modeling and inversion in near-field microwave microscopy (NFMM) and electrical impedance tomography (EIT) problems. Both the modeling and inversion are conducted in the framework of Laplace's equation since the computational domain is much smaller than the wavelength in the NFMM and the problem is purely static in the EIT. For NFMM, in order to quantitatively reconstruct material information from measured signals, a boundary integral and finite element based method is proposed to solve the tip-sample interaction problem, which is a very challenging task in NFMM. The EIT problem is well known as a difficult problem in the filed of inverse problems for its severely nonlinear and highly ill-posed properties, and the thesis has proposed two methods which are highly robust to noise and have low computational cost to solve the problem. In the following, all the specific contributions are summarized as follows:

- The thesis has conducted a complete analysis on tip-sample interaction problems in NFMM:

  - A lumped element model between Z-match network and ground in MIM is presented, and the limitations of the method are discussed. As an improvement of the lumped element method, impedance variation method is proposed to establish the relationship between measured signals in MIM and impedance variations between tip and sample. The theoretical principles behind the impedance variation method are proved in detail.
  - The Dirichlet Green's function to calculate charges on tip in equivalent-sphere model under Bishperical coordinate system is derived. This solution is verified by numerical software, and the limitations of equivalent-sphere model are also discussed.
  - A quantitative analysis approach is presented to determine an effective height of probe beyond which the probe geometry does not contribute significantly to the measurements in NFMM. The study has compared the performance of effective height among three measurement parameter manipulations, and in addition has shown that the effective height highly depends upon the manipulations. The numerical analysis and associated experimental results show that second derivative of capacitance with respect to tip-sample distance is the most robust to probe height. Most importantly, the conclusions about effective height under different measurement parameter manipulations is significant in improving imaging resolution in NSMM.

- The thesis has proposed a novel forward solver for NFMM which can be applied to arbitrary tip shapes, thick and thin films, and complex inhomogeneous perturbation. The proposed method reduces the three-

dimensional computational domain to the computational box beneath the tip, which avoids using FEM to compute the whole computational domain during the scanning process. To simulate three-dimensional tip-sample interaction for scanning points, the proposed method is much faster than brute force all-domain methods.

- The thesis has presented a nonlinear image reconstruction method with total variation constraint in NFMM, and it is verified in numerical examples that it can not only retrieve the permittivity and conductivity distributions in three dimensional samples, but also improve the imaging resolution in NFMM.

- The thesis has proposed two fast Fourier transform subspace-based optimization methods (NFF-SOM and LF-SOM) to solve the EIT problem with arbitrary boundary. It suggests that the speed of the proposed methods is much faster than that of traditional SOM since the computational complexity is largely reduced by implementing FFT in the optimization procedures. Moreover, compared with traditional SOM, both LF-SOM and NFFT-SOM can get a smaller exact error for high noise cases, which means that a better reconstructed results can be obtained for the proposed methods. Most importantly, besides the above mentioned two advantages, it is found that NFFT-SOM has another advantage that it is robust to the L variations. Additionally, the disadvantages of the proposed methods are also discussed in the thesis. It suggests that the drawback of the proposed methods is that, compared with traditional SOM, both of the proposed methods need more iterations in optimization since the noise spaces of them are spanned by complete Fourier bases.

6.2 Future work

Several challenging issues have been dealt with in this study, and future work will address the following aspects:

- The thesis has proposed a nonlinear reconstruction method in chapter 4 based on the proposed forward solver to retrieve the properties of material in NFMM. It suggests that the reconstruction method is able to not only quantitatively obtain sample information from measured signals, but also to improve imaging resolution. Although the proposed method has been verified numerically in this study, it definitely deserves the best endeavor to accomplish it in experiment. Thus, in the next step of the work, practical experiment of inversion method will be addressed, which includes calibrating the MIM systems, fabricating various samples, and dealing with drift errors and noise.

- One of important advantages of the proposed reconstruction method is that it can be easily applied to other microscopies with very few changes about the current setups. Thus, the reconstruction method in this study will also be applied to other scanning imaging techniques. For examples, in another project in which the author has helped to develop the numerical model of optical system, the image inversion approach has been used to improve the resolution of a confocal laser scanning microscope experimentally.

- Based on the working principle of NFMM, it is meaningful to apply the methods and knowledge in this study to investigate some emerging materials, such as two-dimensional (2D) materials [20, 22, 183]. For examples, the MIM introduced in this thesis is very appropriate to

investigate formation of ripples, electron-hole and chemical doping in graphene and 2D materials beyond graphene. Therefore, the possible specific future work may include studying these phenomena using the near-field microwave microscopy techniques.

- The thesis has applied LF-SOM and NFFT-SOM to solve nonlinear, highly ill-posed EIT problems under static situation. In next step, it is meaningful to extend the methods to time-harmonic electromagnetic wave issues. For EIT problems, the developed algorithms are very powerful tools to solve the practical problems in medical imaging, and the application of these algorithms to commercially available EIT instrument is also an important aspect of the future work.

Bibliography

[1] A. Adler, “Modeling electrical impedance tomography current flow in a human thorax model,” EIDORS documentation (2010).

[2] W. Kundhikanjana, “Imaging nanoscale electronic inhomogeneity with microwave impedance microscopy,” Ph.D. thesis, Stanford University (2013).

[3] K. Lai, W. Kundhikanjana, M. Kelly, and Z. X. Shen, “Modeling and characterization of a cantilever-based near-field scanning microwave impedance microscope,” Review of Scientific Instruments **79**, 6 (2008).

[4] Z. Wei, Y. T. Cui, E. Y. Ma, S. Johnston, Y. Yang, R. Chen, M. Kelly, Z. X. Shen, and X. Chen, “Quantitative theory for probe-sample interaction with inhomogeneous perturbation in near-field scanning microwave microscopy,” IEEE Transactions on Microwave Theory and Techniques **64**, 1402–1408 (2016).

[5] P. M. Morse, *Methods of theoretical physics* (McGraw-Hill, 1953).

[6] Y. L. Yang, K. J. Lai, Q. C. Tang, W. Kundhikanjana, M. A. Kelly, K. Zhang, Z. X. Shen, and X. X. Li, “Batch-fabricated cantilever probes with electrical shielding for nanoscale dielectric and conductivity imaging,” Journal of Micromechanics and Microengineering **22**, 8

(2012).

[7] K. Lai, W. Kundhikanjana, M. A. Kelly, and Z. X. Shen, “Calibration of shielded microwave probes using bulk dielectrics,” Applied Physics Letters **93**, 3 (2008).

[8] A. G. Ramm, *Inverse problems* (Springer Science, New York, 2005).

[9] C. Rui, W. Zhun, and C. Xudong, “Three dimensional through-wall imaging: Inverse scattering problems with an inhomogeneous background medium,” Antennas and Propagation (APCAP), 2015 IEEE 4th Asia-Pacific Conference on pp. 505 – 506 (2015).

[10] H. Kagiwada, R. Kalaba, S. Timko, and S. Ueno, “Associate memories for system identification: Inverse problems in remote sensing,” Mathematical and Computer Modelling **14**, 200–202 (1990).

[11] A. Quarteroni, L. Formaggia, and A. Veneziani, *Complex systems in biomedicine* (Springer, New York;Milan;, 2006).

[12] V. A. Marchenko, *Sturm-Liouville operators and applications* (Birkhauser Verlag, 1986).

[13] M. Tanaka and G. S. Dulikravich, *Inverse problems in engineering mechanics* (Elsevier, Amsterdam, 1998).

[14] S. M. Anlage, V. V. Talanov, and A. R. Schwartz, “Principles of near-field microwave microscopy,” in “Scanning Probe Microscopy: Electrical and Electromechanical Phenomena at the Nanoscale,” , vol. 2 (Springer New York, New York, NY, 2007).

[15] E. Y. Ma, M. R. Calvo, J. Wang, B. Lian, M. Muhlbauer, C. Brune, Y. T. Cui, K. J. Lai, W. Kundhikanjana, Y. L. Yang, M. Baenninger,

M. Konig, C. Ames, H. Buhmann, P. Leubner, L. W. Molenkamp, S. C. Zhang, D. Goldhaber-Gordon, M. A. Kelly, and Z. X. Shen, "Unexpected edge conduction in mercury telluride quantum wells under broken time-reversal symmetry," Nature Communications **6** (2015).

[16] Z. Wu, W.-q. Sun, T. Feng, S. W. Tang, G. Li, K.-l. Jiang, S.-y. Xu, and C. K. Ong, "Imaging of soft material with carbon nanotube tip using near-field scanning microwave microscopy," Ultramicroscopy **148**, 75–80 (2015).

[17] K. Haddadi, S. Gu, and T. Lasri, "Sensing of liquid droplets with a scanning near-field microwave microscope," Sensors and Actuators A: Physical **230**, 170–174 (2015).

[18] G. Georg, B. Enrico, L. Andrea, B. P. Samadhan, K. Manuel, R. Christian, G. Rajiv, H. Peter, M. Romolo, and K. Ferry, "Quantitative sub-surface and non-contact imaging using scanning microwave microscopy," Nanotechnology **26**, 135701 (2015).

[19] W. Kundhikanjana, Y. Yang, Q. Tanga, K. Zhang, K. Lai, Y. Ma, M. A. Kelly, X. X. Li, and Z. X. Shen, "Unexpected surface implanted layer in static random access memory devices observed by microwave impedance microscope," Semiconductor Science and Technology **28**, 5 (2013).

[20] A. Takagi, F. Yamada, T. Matsumoto, and T. Kawai, "Electrostatic force spectroscopy on insulating surfaces: the effect of capacitive interaction," Nanotechnology **20**, 7 (2009).

[21] G. Gramse, E. Brinciotti, A. Lucibello, S. B. Patil, M. Kasper, C. Rankl, R. Giridharagopal, P. Hinterdorfer, R. Marcelli, and F. Kienberger,

"Quantitative sub-surface and non-contact imaging using scanning microwave microscopy," Nanotechnology **26**, 9 (2015).

[22] K. Lai, W. Kundhikanjana, M. A. Kelly, Z. X. Shen, J. Shabani, and M. Shayegan, "Imaging of coulomb-driven quantum hall edge states," Physical Review Letters **107**, 5 (2011).

[23] E. Y. Ma, Y.-T. Cui, K. Ueda, S. Tang, K. Chen, N. Tamura, P. M. Wu, J. Fujioka, Y. Tokura, and Z.-X. Shen, "Mobile metallic domain walls in an all-in-all-out magnetic insulator," Science **350**, 538–541 (2015).

[24] A. P. Gregory, J. F. Blackburn, K. Lees, R. N. Clarke, T. E. Hodgetts, S. M. Hanham, and N. Klein, "Measurement of the permittivity and loss of high-loss materials using a near-field scanning microwave microscope," Ultramicroscopy **161**, 137–145 (2016).

[25] S. Berweger, P. T. Blanchard, M. D. Brubaker, K. J. Coakley, N. A. Sanford, T. M. Wallis, K. A. Bertness, and P. Kabos, "Near-field control and imaging of free charge carrier variations in gan nanowires," Applied Physics Letters **108**, 073101 (2016).

[26] D. A. Usanov, S. S. Gorbatov, V. Y. Kvasko, and A. V. Fadeev, "A near-field microwave microscope for determining anisotropic properties of dielectric materials," Instruments and Experimental Techniques **58**, 239–246 (2015).

[27] S. G. Lipson, H. Lipson, and D. S. Tannhauser, *Optical physics*, vol. 3rd (Cambridge University Press, Cambridge;New York;, 1995).

[28] E. H. Land, E. R. Blout, D. S. Grey, M. S. Flower, H. Husek, R. C. Jones, C. H. Matz, and D. P. Merrill, "A color translating ultraviolet microscope," Science **109**, 371–374 (1949).

[29] H. Kazuhiro, T. Yuzuru, Y. Takahiro, H. Nobuyuki, S. Noriyuki, H. Morio, S. Tsutomu, W. Takeo, and K. Hiroo, "Phase defect observation using extreme ultraviolet microscope," Japanese Journal of Applied Physics **45**, 5378 (2006).

[30] K. Yoshito, T. Kei, Y. Takahiro, S. Takashi, U. Toshiyuki, W. Takeo, and K. Hiroo, "Study of critical dimensions of printable phase defects using an extreme ultraviolet microscope," Japanese Journal of Applied Physics **48**, 06FA07 (2009).

[31] K. Hamamoto, Y. Tanaka, S. Y. Lee, N. Hosokawa, N. Sakaya, M. Hosoya, T. Shoki, T. Watanabe, and H. Kinoshita, "Mask defect inspection using an extreme ultraviolet microscope," Journal of Vacuum Science and Technology B **23**, 2852–2855 (2005).

[32] P. A. Cole and F. S. Brackett, "Technical requirements in the determination of absorption spectra by the ultraviolet microscope," Review of Scientific Instruments **11**, 419–427 (1940).

[33] G. Schmahl and D. Rudolph, "Proposal for a phase contrast x-ray microscope," in "X-ray Microscopy: Instrumentation and Biological Applications," , P.-c. Cheng and G.-j. Jan, eds. (Springer Berlin Heidelberg, Berlin, Heidelberg 978-3-642-72881-5, 1987), pp. 231–238.

[34] C. Jacobsen, S. Williams, E. Anderson, M. T. Browne, C. J. Buckley, D. Kern, J. Kirz, M. Rivers, and X. Zhang, "Diffraction-limited imaging in a scanning transmission x-ray microscope," Optics Communications **86**, 351–364 (1991).

[35] J. A. Kong, *Electromagnetic wave theory* (Wiley, New York, 1986).

[36] J. M. Vigoureux and D. Courjon, "Detection of nonradiative fields in

light of the heisenberg uncertainty principle and the rayleigh criterion," Applied Optics **31**, 3170–3177 (1992).

[37] D. Sen, "The uncertainty relations in quantum mechanics," Current Science **107**, 203–218 (2014).

[38] F. J. Giessibl, "Advances in atomic force microscopy," Reviews of Modern Physics **75**, 949–983 (2003).

[39] G. M. King, A. R. Carter, A. B. Churnside, L. S. Eberle, and T. T. Perkins, "Ultrastable atomic force microscopy: Atomic-scale stability and registration in ambient conditions," Nano Letters **9**, 1451–1456 (2009).

[40] J. Zhang, P. Chen, B. Yuan, W. Ji, Z. Cheng, and X. Qiu, "Real-space identification of intermolecular bonding with atomic force microscopy," Science **342**, 611–614 (2013).

[41] K. M. Lang, D. A. Hite, R. W. Simmonds, R. McDermott, D. P. Pappas, and J. M. Martinis, "Conducting atomic force microscopy for nanoscale tunnel barrier characterization," Review of Scientific Instruments **75**, 2726–2731 (2004).

[42] G. Binnig, C. F. Quate, and C. Gerber, "Atomic force microscope," Physical Review Letters **56**, 930–933 (1986).

[43] G. Binnig and H. Rohrer, "Scanning tunneling microscopy (reprinted from ibm journal of research and development, vol 30, 1986)," (2000).

[44] G. Binnig and H. Rohrer, "Scanning tunneling microscopy," Surface Science **126**, 236–244 (1983).

[45] H. Oka, O. O. Brovko, M. Corbetta, V. S. Stepanyuk, D. Sander, and

J. Kirschner, "Spin-polarized quantum confinement in nanostructures: Scanning tunneling microscopy," Reviews of Modern Physics **86**, 1127–1168 (2014).

[46] N. Levy, T. Zhang, J. Ha, F. Sharifi, A. A. Talin, Y. Kuk, and J. A. Stroscio, "Experimental evidence for s-wave pairing symmetry in superconducting $\mathrm{cu}_x\mathrm{bi}_2\mathrm{se}_3$ single crystals using a scanning tunneling microscope," Physical Review Letters **110**, 117001 (2013).

[47] J. C. Koepke, J. D. Wood, D. Estrada, Z.-Y. Ong, K. T. He, E. Pop, and J. W. Lyding, "Atomic-scale evidence for potential barriers and strong carrier scattering at graphene grain boundaries: A scanning tunneling microscopy study," ACS Nano **7**, 75–86 (2013).

[48] F. Klappenberger, "Two-dimensional functional molecular nanoarchitectures complementary investigations with scanning tunneling microscopy and x-ray spectroscopy," Progress in Surface Science **89**, 1–55 (2014).

[49] C. P. Vlahacos, R. C. Black, S. M. Anlage, A. Amar, and F. C. Wellstood, "Nearfield scanning microwave microscope with 100 m resolution," Applied Physics Letters **69**, 3272–3274 (1996).

[50] D. E. Steinhauer, C. P. Vlahacos, F. C. Wellstood, S. M. Anlage, C. Canedy, R. Ramesh, A. Stanishevsky, and J. Melngailis, "Quantitative imaging of dielectric permittivity and tunability with a near-field scanning microwave microscope," Review of Scientific Instruments **71**, 2751–2758 (2000).

[51] D. E. Steinhauer, C. P. Vlahacos, F. C. Wellstood, S. M. Anlage, C. Canedy, R. Ramesh, A. Stanishevsky, and J. Melngailis, "Imaging of

microwave permittivity, tunability, and damage recovery in (ba,sr)tio3 thin films," Applied Physics Letters **75**, 3180–3182 (1999).

[52] S. K. Dutta, C. P. Vlahacos, D. E. Steinhauer, A. S. Thanawalla, B. J. Feenstra, F. C. Wellstood, S. M. Anlage, and H. S. Newman, "Imaging microwave electric fields using a near-field scanning microwave microscope," Applied Physics Letters **74**, 156–158 (1999).

[53] C. P. Vlahacos, D. E. Steinhauer, S. K. Dutta, B. J. Feenstra, S. M. Anlage, and F. C. Wellstood, "Quantitative topographic imaging using a near-field scanning microwave microscope," Applied Physics Letters **72**, 1778–1780 (1998).

[54] A. Imtiaz and S. M. Anlage, "Effect of tip geometry on contrast and spatial resolution of the near-field microwave microscope," Journal of Applied Physics **100**, 044304 (2006).

[55] A. Imtiaz, M. Pollak, S. M. Anlage, J. D. Barry, and J. Melngailis, "Near-field microwave microscopy on nanometer length scales," Journal of Applied Physics **97**, 044302 (2005).

[56] A. Imtiaz, S. M. Anlage, J. D. Barry, and J. Melngailis, "Nanometer-scale material contrast imaging with a near-field microwave microscope," Applied Physics Letters **90**, 143106 (2007).

[57] D. E. Steinhauer, C. P. Vlahacos, S. K. Dutta, B. J. Feenstra, F. C. Wellstood, and S. M. Anlage, "Quantitative imaging of sheet resistance with a scanning near-field microwave microscope," Applied Physics Letters **72**, 861–863 (1998).

[58] D. E. Steinhauer, C. P. Vlahacos, S. K. Dutta, F. C. Wellstood, and S. M. Anlage, "Surface resistance imaging with a scanning near-field

microwave microscope," Applied Physics Letters **71**, 1736–1738 (1997).

[59] A. Imtiaz, T. Baldwin, H. T. Nembach, T. M. Wallis, and P. Kabos, "Near-field microwave microscope measurements to characterize bulk material properties," Applied Physics Letters **90**, 243105 (2007).

[60] A. S. Thanawalla, S. K. Dutta, C. P. Vlahacos, D. E. Steinhauer, B. J. Feenstra, S. M. Anlage, F. C. Wellstood, and R. B. Hammond, "Microwave near-field imaging of electric fields in a superconducting microstrip resonator," Applied Physics Letters **73**, 2491–2493 (1998).

[61] S.-C. Lee, C. P. Vlahacos, B. J. Feenstra, A. Schwartz, D. E. Steinhauer, F. C. Wellstood, and S. M. Anlage, "Magnetic permeability imaging of metals with a scanning near-field microwave microscope," Applied Physics Letters **77**, 4404–4406 (2000).

[62] D. E. Steinhauer and S. M. Anlage, "Microwave frequency ferroelectric domain imaging of deuterated triglycine sulfate crystals," Journal of Applied Physics **89**, 2314–2321 (2001).

[63] M. Tabib-Azar, D. P. Su, A. Pohar, S. R. LeClair, and G. Ponchak, "0.4 mu m spatial resolution with 1 ghz (lambda = 30 cm) evanescent microwave probe," Review of Scientific Instruments **70**, 1725–1729 (1999).

[64] M. Tabibazar, N. S. Shoemaker, and S. Harris, "Nondestructive characterization of materials by evanescent microwaves," Measurement Science and Technology **4**, 583–590 (1993).

[65] M. Tabib-Azar, R. Ciocan, G. Ponchak, and S. R. LeClair, "Transient thermography using evanescent microwave microscope," Review of Scientific Instruments **70**, 3387–3390 (1999).

[66] M. Tabib-Azar, P. S. Pathak, G. Ponchak, and S. LeClair, "Nondestructive superresolution imaging of defects and nonuniformities in metals, semiconductors, dielectrics, composites, and plants using evanescent microwaves," Review of Scientific Instruments **70**, 2783–2792 (1999).

[67] R. Wang, F. Li, and M. Tabib-Azar, "Calibration methods of a 2ghz evanescent microwave magnetic probe for noncontact and nondestructive metal characterization for corrosion, defects, conductivity, and thickness nonuniformities," Review of Scientific Instruments **76**, 054701 (2005).

[68] M. Tabib-Azar and D. Akinwande, "Real-time imaging of semiconductor space-charge regions using high-spatial resolution evanescent microwave microscope," Review of Scientific Instruments **71**, 1460–1465 (2000).

[69] M. Tabib-Azar, D. Akinwande, G. Ponchak, and S. R. LeClair, "Novel physical sensors using evanescent microwave probes," Review of Scientific Instruments **70**, 3381–3386 (1999).

[70] M. Tabib-Azar, R. Ciocan, G. Ponchak, and S. R. LeClair, "Transient thermography using evanescent microwave microscope," Review of Scientific Instruments **70**, 3387–3390 (1999).

[71] M. Tabib-Azar, D. Akinwande, G. E. Ponchak, and S. R. LeClair, "Evanescent microwave probes on high-resistivity silicon and its application in characterization of semiconductors," Review of Scientific Instruments **70**, 3083–3086 (1999).

[72] T.-A. Massood and W. Yaqiang, "Design and fabrication of scanning

near-field microwave probes compatible with atomic force microscopy to image embedded nanostructures," IEEE Transactions on Microwave Theory and Techniques **52**, 971–979 (2004).

[73] M. Tabib-Azar and B. Sutapun, "Novel hydrogen sensors using evanescent microwave probes," Review of scientific instruments **70**, 3707–3713 (1999).

[74] F. X. Li, M. Tabib-Azar, and J. A. Mann, "Surface electron spin resonance study on ruby crystal using evanescent microwave microscopy techniques," IEEE Sensors Journal **7**, 184–191 (2007).

[75] F. Sakran, A. Copty, M. Golosovsky, N. Bontemps, D. Davidov, and A. Frenkel, "Electron spin resonance microscopic surface imaging using a microwave scanning probe," Applied Physics Letters **82**, 1479–1481 (2003).

[76] M. Abu-Teir, F. Sakran, M. Golosovsky, D. Davidov, and A. Frenkel, "Local contactless measurement of the ordinary and extraordinary hall effect using near-field microwave microscopy," Applied Physics Letters **80**, 1776–1778 (2002).

[77] M. Abu-Teir, M. Golosovsky, D. Davidov, A. Frenkel, and H. Goldberger, "Near-field scanning microwave probe based on a dielectric resonator," Review of Scientific Instruments **72**, 2073–2079 (2001).

[78] M. Golosovsky and D. Davidov, "Novel millimeter-wave near-field resistivity microscope," Applied Physics Letters **68**, 1579–1581 (1996).

[79] M. Golosovsky, A. F. Lann, D. Davidov, and A. Frenkel, "Microwave near-field imaging of conducting objects of a simple geometric shape,"

Review of Scientific Instruments **71**, 3927–3932 (2000).

[80] M. Golosovsky, A. Lann, and D. Davidov, “A millimeter-wave near-field scanning probe with an optical distance control,” Ultramicroscopy **71**, 133–141 (1998).

[81] A. Copty, M. Golosovsky, D. Davidov, and A. Frenkel, “Localized heating of biological media using a 1-w microwave near-field probe,” IEEE Transactions on Microwave Theory and Techniques **52**, 1957–1963 (2004).

[82] T. Nozokido, R. Iibuchi, J. Bae, K. Mizuno, and H. Kudo, “Millimeter-wave scanning near-field anisotropy microscopy,” Review of Scientific Instruments **76**, 033702 (2005).

[83] T. Nozokido, J. Bae, and K. Mizuno, “Visualization of photoexcited free carriers by scanning near-field millimeter-wave microscopy,” Applied Physics Letters **77**, 148–150 (2000).

[84] Y. Cho, A. Kirihara, and T. Saeki, “Scanning nonlinear dielectric microscope,” Review of Scientific Instruments **67**, 2297–2303 (1996).

[85] Y. Cho, S. Kazuta, and K. Matsuura, “Scanning nonlinear dielectric microscopy with nanometer resolution,” Applied Physics Letters **75**, 2833–2835 (1999).

[86] Y. Cho, K. Fujimoto, Y. Hiranaga, Y. Wagatsuma, A. Onoe, K. Terabe, and K. Kitamura, “Tbit/inch2 ferroelectric data storage based on scanning nonlinear dielectric microscopy,” Applied Physics Letters **81**, 4401–4403 (2002).

[87] T. Morita and Y. Cho, “Polarization reversal anti-parallel to the applied

electric field observed using a scanning nonlinear dielectric microscopy," Applied Physics Letters **84**, 257–259 (2004).

[88] W. Park, J. Kim, and K. Lee, "Millimeter-wave scanning near-field microscope using a resonant waveguide probe," Applied Physics Letters **79**, 2642–2644 (2001).

[89] S. Hong, J. Kim, W. Park, and K. Lee, "Improved surface imaging with a near-field scanning microwave microscope using a tunable resonator," Applied Physics Letters **80**, 524–526 (2002).

[90] M. S. Kim, S. Kim, J. Kim, K. Lee, B. Friedman, J.-T. Kim, and J. Lee, "Tipsample distance control for near-field scanning microwave microscopes," Review of Scientific Instruments **74**, 3675–3678 (2003).

[91] J. Kim, K. Lee, B. Friedman, and D. Cha, "Near-field scanning microwave microscope using a dielectric resonator," Applied Physics Letters **83**, 1032–1034 (2003).

[92] S. Kim, H. Yoo, K. Lee, B. Friedman, M. A. Gaspar, and R. Levicky, "Distance control for a near-field scanning microwave microscope in liquid using a quartz tuning fork," Applied Physics Letters **86**, 153506 (2005).

[93] A. Babajanyan, K. Lee, E. Lim, T. Manaka, M. Iwamoto, and B. Friedman, "Investigation of space charge at pentacene/metal interfaces by a near-field scanning microwave microprobe," Applied Physics Letters **90**, 182104 (2007).

[94] S. Yun, S. Na, A. Babajayan, H. Kim, B. Friedman, and K. Lee, "Noncontact characterization of sheet resistance of indium-tin-oxide thin films by using a near-field microwave microprobe," Thin Solid

Films **515**, 1354–1357 (2006).

[95] J. Kim, M. S. Kim, K. Lee, J. Lee, D. J. Cha, and B. Friedman, "Development of a near-field scanning microwave microscope using a tunable resonance cavity for high resolution," Measurement Science and Technology **14**, 7–12 (2003).

[96] T. Wei, X.-D. Xiang, W. G. Wallace-Freedman, and P. G. Schultz, "Scanning tip microwave near-field microscope," Applied Physics Letters **68**, 3506–3508 (1996).

[97] Y. L. Lu, T. Wei, F. Duewer, Y. Q. Lu, N. B. Ming, P. G. Schultz, and X. D. Xiang, "Nondestructive imaging of dielectric-constant profiles and ferroelectric domains with a scanning-tip microwave near-field microscope," Science **276**, 2004–2006 (1997).

[98] C. Gao, T. Wei, F. Duewer, Y. Lu, and X.-D. Xiang, "High spatial resolution quantitative microwave impedance microscopy by a scanning tip microwave near-field microscope," Applied Physics Letters **71**, 1872–1874 (1997).

[99] C. Gao and X.-D. Xiang, "Quantitative microwave near-field microscopy of dielectric properties," Review of Scientific Instruments **69**, 3846–3851 (1998).

[100] C. Gao, F. Duewer, and X.-D. Xiang, "Quantitative microwave evanescent microscopy," Applied Physics Letters **75**, 3005–3007 (1999).

[101] C. Gao, B. Hu, P. Zhang, M. Huang, W. Liu, and I. Takeuchi, "Quantitative microwave evanescent microscopy of dielectric thin films using a recursive image charge approach," Applied Physics Letters **84**, 4647–4649 (2004).

[102] F. Duewer, C. Gao, and X.-D. Xiang, “Tipsample distance feedback control in a scanning evanescent microwave probe for nonlinear dielectric imaging,” Review of Scientific Instruments **71**, 2414–2417 (2000).

[103] I. Takeuchi, H. Chang, C. Gao, P. G. Schultz, X.-D. Xiang, R. P. Sharma, M. J. Downes, and T. Venkatesan, “Combinatorial synthesis and evaluation of epitaxial ferroelectric device libraries,” Applied Physics Letters **73**, 894–896 (1998).

[104] C. Gao, F. Duewer, Y. Lu, and X.-D. Xiang, “Quantitative nonlinear dielectric microscopy of periodically polarized ferroelectric domains,” Applied Physics Letters **73**, 1146–1148 (1998).

[105] Z. Wang, M. A. Kelly, Z.-X. Shen, G. Wang, X.-D. Xiang, and J. T. Wetzel, “Evanescent microwave probe measurement of low-k dielectric films,” Journal of Applied Physics **92**, 808–811 (2002).

[106] Y. Wang, A. D. Bettermann, and D. W. van der Weide, “Process for scanning near-field microwave microscope probes with integrated ultratall coaxial tips,” Journal of Vacuum Science and Technology B **25**, 813–816 (2007).

[107] J. D. Chisum and Z. Popovic, “Performance limitations and measurement analysis of a near-field microwave microscope for nondestructive and subsurface detection,” IEEE Transactions on Microwave Theory and Techniques **60**, 2605–2615 (2012).

[108] V. V. Talanov and A. R. Schwartz, “Near-field scanning microwave microscope for interline capacitance characterization of nanoelectronics interconnect,” IEEE Transactions on Microwave Theory and Tech-

niques **57**, 1224–1229 (2009).

[109] K. J. Lai, M. Nakamura, W. Kundhikanjana, M. Kawasaki, Y. Tokura, M. A. Kelly, and Z. X. Shen, "Mesoscopic percolating resistance network in a strained manganite thin film," Science **329**, 190–193 (2010).

[110] Y. L. Yang, E. Y. Ma, Y. T. Cui, A. Haemmerli, K. J. Lai, W. Kundhikanjana, N. Harjee, B. L. Pruitt, M. Kelly, and Z. X. Shen, "Shielded piezoresistive cantilever probes for nanoscale topography and electrical imaging," Journal of Micromechanics and Microengineering **24**, 7 (2014).

[111] L. Fumagalli, D. Esteban-Ferrer, A. Cuervo, J. L. Carrascosa, and G. Gomila, "Label-free identification of single dielectric nanoparticles and viruses with ultraweak polarization forces," Nature Materials **11**, 808–816 (2012).

[112] G. M. Sacha, "Influence of the substrate and tip shape on the characterization of thin films by electrostatic force microscopy," IEEE Transactions on Nanotechnology **12**, 152–156 (2013).

[113] L. Fumagalli, M. A. Edwards, and G. Gomila, "Quantitative electrostatic force microscopy with sharp silicon tips," Nanotechnology **25**, 9 (2014).

[114] G. Gramse, G. Gomila, and L. Fumagalli, "Quantifying the dielectric constant of thick insulators by electrostatic force microscopy: effects of the microscopic parts of the probe," Nanotechnology **23**, 7 (2012).

[115] L. Fumagalli, G. Gramse, D. Esteban-Ferrer, M. A. Edwards, and G. Gomila, "Quantifying the dielectric constant of thick insulators using electrostatic force microscopy," Applied Physics Letters **96**, 3 (2010).

[116] G. Gomila, G. Gramse, and L. Fumagalli, "Finite-size effects and analytical modeling of electrostatic force microscopy applied to dielectric films," Nanotechnology **25**, 11 (2014).

[117] G. M. Sacha, F. B. Rodriguez, and P. Varona, "An inverse problem solution for undetermined electrostatic force microscopy setups using neural networks," Nanotechnology **20**, 5 (2009).

[118] G. Gramse, M. Kasper, L. Fumagalli, G. Gomila, P. Hinterdorfer, and F. Kienberger, "Calibrated complex impedance and permittivity measurements with scanning microwave microscopy," Nanotechnology **25**, 8 (2014).

[119] G. M. Sacha and J. J. Saenz, "Cantilever effects on electrostatic force gradient microscopy," Applied Physics Letters **85**, 2610–2612 (2004).

[120] B. Harrach, J. K. Seo, and E. J. Woo, "Factorization method and its physical justification in frequency-difference electrical impedance tomography," IEEE Transactions on Medical Imaging **29**, 1918–1926 (2010).

[121] C. Bellis, A. Constantinescu, T. Coquet, T. Jaravel, and A. Lechleiter, "A non-iterative sampling approach using noise subspace projection for eit," Inverse Problems **28**, 25 (2012).

[122] Y. T. Chow, K. Ito, and J. Zou, "A direct sampling method for electrical impedance tomography," Inverse Problems **30**, 25 (2014).

[123] W. Zhun, C. Rui, H. Zhao, and C. Xudong, "Two fft subspace-based optimization methods for electrical impedance tomography," Submitted to Inverse Problems (2016).

[124] L. Borcea, "Electrical impedance tomography," Inverse Problems **18**, R99–R136 (2002).

[125] G. Alessandrini and S. Vessella, "Lipschitz stability for the inverse conductivity problem," Advances in Applied Mathematics **35**, 207–241 (2005).

[126] J. Sylvester and G. Uhlmann, "Inverse boundary value problems at the boundarycontinuous dependence," Communications on pure and applied mathematics **41**, 197–219 (1988).

[127] R. V. Kohn and M. Vogelius, "Determining conductivity by boundary measurements ii. interior results," Communications on Pure and Applied Mathematics **38**, 643–667 (1985).

[128] R. Kohn and M. Vogelius, "Determining conductivity by boundary measurements," Communications on Pure and Applied Mathematics **37**, 289–298 (1984).

[129] B. Harrach, J. K. Seo, and E. J. Woo, "Factorization method and its physical justification in frequency-difference electrical impedance tomography," Medical Imaging, IEEE Transactions on **29**, 1918–1926 (2010).

[130] S. Babaeizadeh and D. H. Brooks, "Electrical impedance tomography for piecewise constant domains using boundary element shape-based inverse solutions," Medical Imaging, IEEE Transactions on **26**, 637–647 (2007).

[131] M. Bruhl, M. Hanke, and M. S. Vogelius, "A direct impedance tomography algorithm for locating small inhomogeneities," Numerische Mathematik **93**, 635–654 (2003).

[132] N. Chaulet, S. Arridge, T. Betcke, and D. Holder, "The factorization method for three dimensional electrical impedance tomography," Inverse Problems **30**, 15 (2014).

[133] T. J. Yorkey, J. G. Webster, and W. J. Tompkins, "Comparing reconstruction algorithms for electrical impedance tomography," IEEE Trans. Biomed. Eng. **34**, 843– 852 (1987).

[134] L. Borcea, G. A. Gray, and Y. Zhang, "Variationally constrained numerical solution of electrical impedance tomography," Inverse Problems **19**, 1159–1184 (2003).

[135] X. D. Chen, "Subspace-based optimization method in electric impedance tomography," Journal of Electromagnetic Waves and Applications **23**, 1397–1406 (2009).

[136] E. Castellano-Hernandez and G. M. Sacha, "Ultrahigh dielectric constant of thin films obtained by electrostatic force microscopy and artificial neural networks," Applied Physics Letters **100**, 3 (2012).

[137] A. Guadarrama-Santana and A. Garcia-Valenzuela, "Obtaining the dielectric constant of solids from capacitance measurements with a pointer electrode," Review of Scientific Instruments **80**, 3 (2009).

[138] W. Zhun, K. Agarwal, and C. Xudong, "Analytical green's function for tip-sample interaction in microwave impedance microscopy," Advanced Materials and Processes for RF and THz Applications (IMWS-AMP), 2015 IEEE MTT-S International Microwave Workshop Series on pp. 1 – 3 (2015).

[139] P. H. Moon and D. E. Spencer, *Field theory handbook: including coordinate systems, differential equations, and their solutions* (Springer-

Verlag, 1961).

[140] J. Jackson, *Classical Electrodynamics* (Wiley, 1998).

[141] F. Wang, N. Clement, D. Ducatteau, D. Troadec, H. Tanbakuchi, B. Legrand, G. Dambrine, and D. Theron, "Quantitative impedance characterization of sub-10nm scale capacitors and tunnel junctions with an interferometric scanning microwave microscope," Nanotechnology **25**, 7 (2014).

[142] J. Hoffmann, G. Gramse, J. Niegemann, M. Zeier, and F. Kienberger, "Measuring low loss dielectric substrates with scanning probe microscopes," Applied Physics Letters **105**, 4 (2014).

[143] C. Riedel, A. Alegria, G. A. Schwartz, J. Colmenero, and J. J. Saenz, "Numerical study of the lateral resolution in electrostatic force microscopy for dielectric samples," Nanotechnology **22**, 6 (2011).

[144] D. Ziegler and A. Stemmer, "Force gradient sensitive detection in lift-mode kelvin probe force microscopy," Nanotechnology **22**, 9 (2011).

[145] H. P. Huber, M. Moertelmaier, T. M. Wallis, C. J. Chiang, M. Hochleitner, A. Imtiaz, Y. J. Oh, K. Schilcher, M. Dieudonne, J. Smoliner, P. Hinterdorfer, S. J. Rosner, H. Tanbakuchi, P. Kabos, and F. Kienberger, "Calibrated nanoscale capacitance measurements using a scanning microwave microscope," Review of Scientific Instruments **81**, 9 (2010).

[146] S. Hudlet, M. Saint Jean, C. Guthmann, and J. Berger, "Evaluation of the capacitive force between an atomic force microscopy tip and a metallic surface," European Physical Journal B **2**, 5–10 (1998).

[147] B. M. Law and F. Rieutord, “Electrostatic forces in atomic force microscopy,” Physical Review B **66**, 6 (2002).

[148] A. Karbassi, D. Ruf, A. D. Bettermann, C. A. Paulson, D. W. van der Weide, H. Tanbakuchi, and R. Stancliff, “Quantitative scanning near-field microwave microscopy for thin film dielectric constant measurement,” Review of Scientific Instruments **79**, 5 (2008).

[149] S. Gomez-Monivas, J. J. Saenz, R. Carminati, and J. J. Greffet, “Theory of electrostatic probe microscopy: A simple perturbative approach,” Applied Physics Letters **76**, 2955–2957 (2000).

[150] G. M. Sacha, E. Sahagun, and J. J. Saenz, “A method for calculating capacitances and electrostatic forces in atomic force microscopy,” Journal of Applied Physics **101** (2007).

[151] G. M. Sacha, C. Gomez-Navarro, J. J. Saenz, and J. Gomez-Herrero, “Quantitative theory for the imaging of conducting objects in electrostatic force microscopy,” Applied Physics Letters **89** (2006).

[152] G. M. Sacha, “Method to calculate electric fields at very small tip-sample distances in atomic force microscopy,” Applied Physics Letters **97** (2010).

[153] W. Zhun and C. Xudong, “Numerical study of resolution in near field microscopy for dielectric samples,” Antennas and Propagation USNC/URSI National Radio Science Meeting, 2015 IEEE International Symposium on pp. 910–911 (2015).

[154] J. Jin, *The finite element method in electromagnetics*, vol. 2nd (John Wiley Sons, New York;Great Britain;, 2002).

[155] E. Castellano-Hernandez, J. Moreno-Llorena, J. J. Saenz, and G. M. Sacha, "Enhanced dielectric constant resolution of thin insulating films by electrostatic force microscopy," Journal of Physics-Condensed Matter **24**, 5 (2012).

[156] Y. Birhane, J. Otero, F. Perez-Murano, L. Furnagalli, G. Gomila, and J. Bausells, "Batch fabrication of insulated conductive scanning probe microscopy probes with reduced capacitive coupling," Microelectronic Engineering **119**, 44–47 (2014).

[157] M. Farina, D. Mencarelli, A. Di Donato, G. Venanzoni, and A. Morini, "Calibration protocol for broadband near-field microwave microscopy," IEEE Transactions on Microwave Theory and Techniques **59**, 2769–2776 (2011).

[158] H. Z. Liu, A. R. Hawkins, S. M. Schultz, and T. E. Oliphant, "Fast nonlinear image reconstruction for scanning impedance imaging," Ieee Transactions on Biomedical Engineering **55**, 970–977 (2008).

[159] P. L. Combettes and J. Luo, "An adaptive level set method for nondifferentiable constrained image recovery," IEEE Transactions on Image Processing **11**, 1295–1304 (2002).

[160] P. L. Combettes and J.-C. Pesquet, "Image restoration subject to a total variation constraint," IEEE transactions on image processing **13**, 1213–1222 (2004).

[161] G. Van Kempen and L. Van Vliet, "The influence of the regularization parameter and the first estimate on the performance of tikhonov regularized non-linear image restoration algorithms," Journal of Microscopy **198**, 63 (2000).

[162] Y.-W. Wen and R. H. Chan, “Parameter selection for total-variation-based image restoration using discrepancy principle,” IEEE Transactions on Image Processing **21**, 1770–1781 (2012).

[163] C. R. Vogel and M. E. Oman, “Iterative methods for total variation denoising,” SIAM Journal on Scientific Computing **17**, 227–238 (1996).

[164] Y. H. Dai and Y. Yuan, “A nonlinear conjugate gradient method with a strong global convergence property,” Siam Journal on Optimization **10**, 177–182 (1999).

[165] A. Kirsch, “The music algorithm and the factorization method in inverse scattering theory for inhomogeneous media,” Inverse Problems **18**, 1025–1040 (2002).

[166] B. Gebauer, “The factorization method for real elliptic problems,” Zeitschrift Fur Analysis Und Ihre Anwendungen **25**, 81–102 (2006).

[167] I. Catapano, L. Crocco, and T. Isernia, “On simple methods for shape reconstruction of unknown scatterers,” IEEE Transactions on Antennas and Propagation **55**, 1431–1436 (2007).

[168] A. Lechleiter, N. Hyvonen, and H. Hakula, “The factorization method applied to the complete electrode model of impedance tomography,” Siam Journal on Applied Mathematics **68**, 1097–1121 (2008).

[169] B. Gebauer and N. Hyvonen, “Factorization method and irregular inclusions in electrical impedance tomography,” Inverse Problems **23**, 2159–2170 (2007).

[170] N. Hyvonen, H. Hakula, and S. Pursiainen, “Numerical implementation of the factorization method within the complete electrode model of

electrical impedance tomography," Inverse Problems and Imaging **1**, 299–317 (2007).

[171] P. M. van den Berg and R. E. Kleinman, "A contrast source inversion method," Inverse Problems **13**, 1607–1620 (1997).

[172] A. Abubakar, P. M. van den Berg, and J. J. Mallorqui, "Imaging of biomedical data using a multiplicative regularized contrast source inversion method," IEEE Transactions on Microwave Theory and Techniques **50**, 1761–1771 (2002).

[173] A. Abubakar, W. Hu, P. M. van den Berg, and T. M. Habashy, "A finite-difference contrast source inversion method," Inverse Problems **24** (2008).

[174] X. D. Chen, "Subspace-based optimization method for solving inverse-scattering problems," IEEE Transactions on Geoscience and Remote Sensing **48**, 42–49 (2010).

[175] Y. Zhong, X. D. Chen, and K. Agarwal, "An improved subspace-based optimization method and its implementation in solving three-dimensional inverse problems," IEEE Transactions on Geoscience and Remote Sensing **48**, 3763–3768 (2010).

[176] Y. Zhong and X. D. Chen, "An fft twofold subspace-based optimization method for solving electromagnetic inverse scattering problems," IEEE Transactions on Antennas and Propagation **59**, 914–927 (2011).

[177] P. C. Hansen, M. E. Kilmer, and R. H. Kjeldsen, "Exploiting residual information in the parameter choice for discrete ill-posed problems," Bit Numerical Mathematics **46**, 41–59 (2006).

[178] A. Lakhtakia and G. W. Mulholland, “On 2 numerical techniques for light-scattering by dielectric agglomerated structures,” Journal of Research of the National Institute of Standards and Technology **98**, 699–716 (1993).

[179] A. Gil, J. Segura, and N. M. Temme, *Numerical methods for special functions* (Society for Industrial and Applied Mathematics, Philadelphia, Pa, 2007).

[180] X. D. Chen, “Application of signal-subspace and optimization methods in reconstructing extended scatterers,” Journal of the Optical Society of America a-Optics Image Science and Vision **26**, 1022–1026 (2009).

[181] G. W. Stewart, *Matrix algorithms* (Society for Industrial and Applied Mathematics, Philadelphia, 1998).

[182] P. M. van den Berg, A. L. van Broekhoven, and A. Abubakar, “Extended contrast source inversion,” Inverse Problems **15**, 1325–1344 (1999).

[183] Y. Wang, Y. M. Yang, Z. Z. Zhao, C. Zhang, and Y. H. Wu, “Local electron field emission study of two-dimensional carbon,” Applied Physics Letters **103** (2013).

Appendix A: Derivation of Coefficients in Dirichlet Green's Function for Equivalent-Sphere Model

In this appendix, we have derived Eq. (2.19) from Eq. (2.18) and Eq. (2.16). According to the boundary condition $\varphi = \varphi_g + \varphi_p = 0|_{\mu=0}$, we have:

$$-\frac{1}{4\pi\varepsilon_0 a}\sqrt{(\cosh\mu_c - \cos\eta_c)}\cdot F_p(\mu=0) = \sum_{n=0}^{\infty}\sum_{m=0}^{n}\cos[m(\phi-\phi_c)]\cdot P_n^m(\cos\eta)(A+B) \tag{A.1}$$

in which

$$F_p(\mu=0) = \sum_{n=0}^{\infty}\sum_{m=0}^{n}\varepsilon_m\frac{(n-m)!}{(n+m)!}\cos[m(\phi-\phi_c)]\cdot P_n^m(\cos\eta_c)P_n^m(\cos\eta)e^{-(n+0.5)\mu_c} \tag{A.2}$$

Further considering the boundary condition $\varphi = \varphi_g + \varphi_p = 0|_{\mu=\mu_0}$, we have:

$$-\frac{1}{4\pi\varepsilon_0 a}\sqrt{(\cosh\mu_c - \cos\eta_c)}\cdot F_p(\mu=\mu_0) = \sum_{n=0}^{\infty}\sum_{m=0}^{n}\cos[m(\phi-\phi_c)]\cdot P_n^m(\cos\eta)A_e \tag{A.3}$$

with $A_e = Ae^{(n+0.5)\mu_0} + Be^{-(n+0.5)\mu_0}$, and

$$F_p(\mu=\mu_0) = \sum_{n=0}^{\infty}\sum_{m=0}^{n}\varepsilon_m\frac{(n-m)!}{(n+m)!}\cos[m(\phi-\phi_c)]\cdot P_n^m(\cos\eta_c)P_n^m(\cos\eta)e^{-(n+0.5)(\mu_0-\mu_c)} \tag{A.4}$$

Combining A.1 and A.2, we can solve A and B as:

$$A = \frac{M[e^{-(0.5+n)(\mu_0+\mu_c)} - e^{-(0.5+n)(\mu_0-\mu_c)}]}{e^{-(0.5+n)\mu_0} - e^{(0.5+n)\mu_0}} \tag{A.5}$$

and

$$B = \frac{M[e^{-(0.5+n)(\mu_0-\mu_c)} - e^{-(0.5+n)(\mu_c-\mu_0)}]}{e^{-(0.5+n)\mu_0} - e^{(0.5+n)\mu_0}} \tag{A.6}$$

with

$$M = -\frac{1}{a}\sqrt{(\cosh\mu_c - \cos\eta_c)} \cdot \varepsilon_m \frac{(n-m)!}{(n+m)!} P_n^m(\cos\eta_c) \cdot \frac{1}{4\pi\varepsilon_0} \tag{A.7}$$